STUDY OF A CLOSE-GRID GEODYNAMIC MEASUREMENT SYSTEM

Final Report

Grant NGR 09-015-002
Supplement No. 59

May 1977

Smithsonian Institution
Astrophysical Observatory
Cambridge, Massachusetts 02138

The Smithsonian Astrophysical Observatory
and the Harvard College Observatory
are members of the
Center for Astrophysics

STUDY OF A CLOSE-GRID GEODYNAMIC MEASUREMENT SYSTEM

Final Report

Grant NGR 09-015-002
Supplement No. 59

May 1977

Smithsonian Institution
Astrophysical Observatory
Cambridge, Massachusetts 02138

TABLE OF CONTENTS

TABLE OF CONTENTS (Cont.)

ABSTRACT

The Clogeos (Close-Grid Geodynamic Measurement System) concept envisions a complete range or range-rate measurement terminal installed in a satellite in a near-polar orbit with a network of relatively simple transponders or retro-reflectors on the ground at intervals of 0.1 to 10 km. To measure the distortion of the grid in three dimensions to accuracies of ±1 cm is the ultimate goal of such a system, with obviously important applications to geodynamics, glaciology, and geodesy.

This report discusses a number of aspects of the Clogeos concept, including the anticipated problem areas. User requirements are considered, and a typical grid, designed for earthquake prediction, has been laid out along the San Andreas, Hayward, and Calaveras faults in southern California.

In order to determine the sensitivity of both range and range-rate measurements to small grid motions, a simplified model was constructed and analyzed. Variables in the model are satellite altitude and elevation angle plus grid displacements in latitude, longitude, and height. To determine the potential accuracy of such systems in the absence of ionospheric and atmospheric perturbations, several types of hardware embodiments of Clogeos systems are analyzed, including radio and optical pulse ranging and radio doppler tracking.

Tropospheric-induced range errors are considered in detail at both radio and optical wavelengths, and the accuracy limitations imposed by refractivity variations are estimated for a number of conditions. Cloud-cover statistics for several locales of interest for earthquake monitoring are tabulated as part of the determination of tropospheric constraints. Also discussed at length are multiple-wavelength optical ranging systems for correcting refractivity errors and over-constrained grids for solving for path-averaged refractivity.

Preliminary conclusions and recommendations for future study and experiments on the characterization of path-averaged refractivity at both optical and radio wavelengths are given at the end of the report.

STUDY OF A CLOSE-GRID GEODYNAMIC MEASUREMENT SYSTEM

Final Report

Grant NGR 09-015-002
Supplement No. 59

1. INTRODUCTION AND BACKGROUND

1.1 Introduction

The paradigm of plate tectonics allows a number of geophysical phenomena to be considered together as parts of a complex system. The earth's surface is pictured as composed of several lithospheric plates moving with respect to each other. New plate material is formed at oceanic ridges by the upwelling of molten magma. Old plate material is driven deep beneath the surface along ocean trenches, where one plate rides up over another and simultaneously builds mountain chains. Further development of this paradigm depends on theoretical advances and observations from a variety of sources. The Earth and Ocean Dynamics Applications Program conducted by the National Aeronautics and Space Administration (NASA) addresses a number of these measurements.

Earthquake activity is largely concentrated along the boundaries between tectonic plates. Many of these boundaries lie beneath the sea, making detailed observations of crustal motions difficult if not impossible with current technology. Those that traverse landmasses are of keen interest; the San Andreas Fault is one example. Motions between lithospheric plates average several centimeters per year, but it is not clear whether the motion is episodic or continuous. It is clear, however, that a complex variety of motions may take place near a fault zone. To unravel the tangle of events, it would be desirable to measure the position (in three dimensions) of a large number of stations near a fault.

The current worldwide grid of satellite-tracking stations is sparse. With the advent of the Lageos satellite plus altimeter-equipped Geos 3 and the planned Seasat, measurement accuracies can be dramatically improved on a global basis. However, to fill in the gaps between stations — i.e., to densify the network — is unreasonably costly. An alternative might be to place the costly "tracking station" in a satellite and locate a large number of inexpensive "reflectors" on the ground — an inverted Lageos, or Clogeos, concept.

Under a supplement to NASA Grant NGR 09-015-002, the Smithsonian Astrophysical Observatory (SAO) has been investigating concepts for "tracking" such ground stations from one or more satellites. The idea of applying an orbiting system to various observing and data-gathering tasks is not new, nor is it the subject of this report. Here we deal with one specialized aspect of satellite-to-ground tracking — high-precision position determination.

Is it possible to use satellite techniques to locate a large number of "stations" on the earth's surface to an accuracy of 1 cm? Can it be done economically and with sufficient regularity and reliability to be a useful technique? Does the technology to make it possible exist today? Which techniques or combination of techniques holds the most promise? It was these and related questions that SAO set out to investigate.

The primary motive was to see if a more detailed and accurate picture of crustal motions near fault zones could be generated. This application immediately placed limits on accuracies, numbers of stations to be monitored, frequency of measurements, and similar parameters.

In the sections that follow, the system is defined and examined with particular attention paid to attainable accuracies. The many sources of errors are identified and possible methods for circumventing or correcting them are discussed.

1.2 Clogeos Mission

Satellite systems have proved to be very effective geodetic tools for conducting large-scale surveys. Indeed, the first accurate worldwide geodetic networks were obtained by satellite. Now, because they are less expensive, much faster, and more accurate, satellite methods are superseding conventional ground-based geodetic methods for establishing accurate large-scale networks within continental areas (e.g., in the United States, Canada, Brazil, Australia, and Europe). As one example, the U.S. Navy's Transit/Geoceiver system is being used as the standard method for measuring large geodetic networks in many countries, being particularly effective in difficult terrain and under unfavorable weather conditions.

NASA has launched a series of geodetic satellites that have provided unique capabilities for accurate global positioning. Programs in lunar ranging and very long-baseline interferometry (VLBI), both of which have good potential in this area, have also received NASA support. The instrumentation developed under these programs has reached the point where we can reasonably expect global-positioning accuracies of about 2 cm within a few years.

But can satellite systems be effective in the densification of geodetic grids, where both high accuracy and large numbers of survey stations are required? It seems clear that present satellite systems are not suitable for frequent measurements of dense geodetic networks, either because ground stations are much too expensive or, in the case of Transit, because the system lacks the required accuracy. NASA has very sensibly suggested considering the possibility of shifting the expensive high-precision ground-station instrumentation to the satellite, thereby simplifying and reducing ground-station cost. SAO believes that this idea is feasible and may also be cost effective.

If a geodetic-grid-densification satellite system should prove practical, it would be reasonable to adopt as its primary mission the monitoring of crustal motions in fault zones. There is an urgent, unfulfilled need for

such information; the accuracies required for this mission seem to be attainable; and if this most demanding objective can be met, the system will also have the capability to pursue other geodetic objectives.

The usefulness of geodetic measurements in studying strain buildup was considered by the U.S. Geodynamics Committee, who stated that, "Virtually everything we know about the nature of strain buildup that leads to earthquakes in the western United States comes from geodetic studies that began in the late 1800's. Until we gain a better understanding of the regional deformation that precedes — and indeed causes — major earthquakes, we shall continue to remain in an unsatisfactory position to determine adequately seismic hazards in space and time. Measurements of such deformation necessarily involve observations encompassing distances of many kilometers, and older classical surveying methods are now being supplemented by new techniques that promise major breakthroughs in both the accuracy and the economics of the observational programs" (National Academy of Sciences, 1973, p. 83). Enlarging on this last statement, the Committee noted that "An entirely new era in geodesy is opening up with the use of satellite data" (National Academy of Sciences, 1973, p. 84).

Accurate measurements of crustal motion over a period of time (e.g., 1 cm/yr over a decade) and throughout a closely spaced geodetic grid in a fault zone would constitute an excellent record of strain accumulation. In combination with other information, this record should make it possible to start assembling a reliable model of the stress field. Other applicable inputs would include the history of previous tectonic activity in the zone and, from VLBI, Lageos observations, and lunar ranging, the relative velocities of the adjoining lithospheric plates (plate motion is the prime mover for earthquakes). There is little question that accurate and detailed models of the stress fields in fault zones would be of great value to earthquake research, and almost certainly to earthquake prediction.

In addition to long-term monitoring of crustal motions, the system should also be designed to detect and measure accurately those crustal motions that

On the other hand, there are examples of what can be done with an appropriate data base. The concept of plate tectonics was developed immediately after observations were made with extensive seismic networks and the global pattern of seismicity became apparent. Landsat pictures have had startling success, revealing patterns of geological formations, vegetation, etc., with surprising clarity, patterns that had never previously been visible even from the enormous number of aerial photographs made over the years.

It would be truly surprising if the synoptic data from a Clogoes system did not lead to a similar advance in revealing patterns of crustal motion, and this information, in turn, will necessarily lead to significantly better knowledge of earthquakes.

2. USER REQUIREMENTS

An operational Clogeos system must be designed and engineered to satisfy the needs of its user community. The primary requirement for high-resolution grid measurements is in the study and prediction of earthquakes; the first section herein presents a brief summary of the accuracy, data rate, grid spacing, and cost tradeoffs for an earthquake-prediction network. Section 2.2 describes a hypothetical Clogeos grid deployed along the major fault lines of southern California. This grid was designed at SAO to illustrate the practical aspects of grid layout, with considerable attention being paid to road access, natural topographic features, and the presence of existing seismograph and geodimeter stations.

2.1 Requirements for an Earthquake-Prediction System

To meet its primary objective, Clogeos should be designed to make three-dimensional measurements of the relative positions of points in a geodetic grid to an accuracy on the order of 1 cm. A complete survey should be made every 3 months, with more frequent (at least weekly) observations conducted at any time on demand in selected areas, e.g., when there are indications of unusual crustal movement or suspicions of an imminent earthquake. (Such indications may be derived from Clogeos itself or from other sensors such as tiltmeters or seismic detectors.)

Grid spacing will vary from about 5 to 60 km, depending on the area being surveyed. As a minimum, the system should be capable of performing surveys in the active fault zones in California, Nevada, and Alaska. A reasonable estimate of the total number of grid points that should be observed is 1000 to 2000; a definitive number cannot be given until we have sufficient information from the Clogeos system itself.

The 1-cm accuracy requirement derives from the magnitudes of those crustal movements that have been observed, i.e., 0 to 15 cm/yr. It should be

emphasized that a region within a fault zone that shows little or no active faulting or crustal motion may very well be a site of great crustal stress, specifically because there is no crustal motion to relieve accumulating stress. Indeed, this is why many previous earthquakes have occurred at unexpected times and places. Such sites — those showing no crustal movements but where large stress buildup is occurring — would be quite evident from a sufficiently accurate and detailed map of regional strain accumulation.

The 3-month cycle for obtaining each complete resurvey is based on the episodic nature of crustal motions. Along some faults, fault motion is fairly steady over periods of many years. However, in many cases, fault motion is quite sporadic, sometimes showing no movement for a long interval followed by either a sudden motion or an interval of steady motion. Of course, earthquakes themselves are an example of sudden movements. Even more important are those cases where a distinct change in either horizontal or vertical crustal motions, or in both, has preceded an earthquake. These premonitory motions have been observed to take place over a period of months preceding large earthquakes (see, e.g., Savage et al., 1973; Scholz et al., 1973).

Grid spacing is derived from consideration of the scale of horizontal variations in strain fields. Near an active fault line, significant variations may occur within distances of a kilometer or less, whereas in other regions within a fault zone, there may be no significant structure over distances as large as 50 km or more. When possible, the actual selection of grid sites should be tailored to known scales of strain-field structure, and in all cases, sites should be selected in collaboration with agencies such as the U.S. Geological Survey. The information needed to make the best selection of ground sites is not now available; it can be generated only after a system like Clogeos has been producing data over a few years. We would expect that the locations of ground sites in the densification grid, the frequency of interrogation, and other operating parameters will all be modified periodically as the overall pattern of crustal motions develops from a growing Clogeos data base.

An important requirement that seems self-evident but is sometimes overlooked is the need for reliability not only in hardware operability, but also

in output information. Reliability, in this sense, must be attained through redundant observations, internal consistency checks such as multiple-grid closures, and comparison of computed baselines with ground surveys and Clogeos and VLBI terminals where available. The Clogeos software should be designed to perform such tests frequently and routinely.

The most difficult — but quite real — requirement to assess is cost. Obviously, the system cost and, in particular, the ground station cost should be "low." But it is not clear just how many dollars constitute low. Right now, with no truly catastrophic U.S. earthquake fresh in mind, and with an undefined Clogoes system without established credibility, a satellite cost of $15 million and ground-station costs of $5,000 each may be an upper limit. On the other hand, consider the comment by Arthur Grantz (1971) of the U.S. Geological Survey: "Had the Lower Van Norman Lake Dam, which was close to collapse when the earthquake ended, actually failed, the San Fernando earthquake might have become infamous as the deadliest in United States history." In this event, the acceptable Clogeos dollar value could more than double. To go a step farther, we can imagine a time in the future when NASA has a well-defined and detailed design for a Clogeos system that has undergone sufficient study to establish genuine confidence in its ability to predict earthquakes reliably. Under these circumstances, the acceptable Clogeos cost could increase several times over.

Rather than set an a priori dollar value for Clogeos, we would recommend first defining the system with the lowest cost that is reasonably close to meeting the performance requirements and then estimating the satellite and ground-station costs.

An item that should not be overlooked in estimating costs is the selection and preparation of each ground-station site. Contrary to some suggestions, we do not believe that the station equipment can simply be lowered from a helicopter. If observations of crustal movements are to be made to 1-cm accuracy over a number of years, each installation must be carefully selected and prepared to ensure that the station is solidly anchored to the crust and will not

be perturbed by unrelated surface movements. We consider this to be a fundamental and nontrivial problem, one that should be delegated to an organization, such as the U.S. Geological Survey, that has had long experience in coping with such problems. It seems clear that site preparation will be a significant part of the cost of each installation.

2.2 A Clogeos Network for Southern California

As an example of a Clogeos grid designed for earthquake prediction, we have laid out a typical grid along the San Andreas, Hayward, and Calaveras faults, running about 75 km northwest and southeast of the junction east of Monterey. This location was selected because it provides maximum fault coverage over a limited sample area. The philosophy behind the criteria for the grid specifications was an attempt to maintain linear dimensions consistent with homogeneity in the gross atmospheric structure, while ensuring that opposing stations are far enough removed to be decidedly on opposite sides of a particular fault but close enough to the fault to register the desired relative crustal motion.

Grid points were chosen at existing geological stations where possible. When it was necessary to add new stations, we tried to locate them conveniently for ease of access and construction and at points that were readily definable in terms of latitude, longitude, and elevation. An attempt was made to maintain a maximum station separation of 10 to 30 km, with roughly half the stations on each side of the faults. A somewhat more dense network of stations was placed around the fault intersection east of Monterey so that this geologically interesting area can be examined in more detail by a Clogeos system.

The layout of our sample network is shown on the maps reproduced in Figure 2-1. Table 2-1 lists the latitude, longitude, and elevation of the grid points. The station numbers are arbitrary, serving to identify each station on the accompanying maps. Three-letter station codes are existing National Center for Earthquake Research (NCER) seismograph stations; those labeled "Geod." are surveyed NCER geodimeter stations. Grid points with no additional identification

are stations that do not currently exist and would require surveying before being established in an operational system. Data for the seismograph stations were obtained from NCER Open File Report 75-125 "Catalog of Earthquakes Along the San Andreas Fault System in Central California" dated April-June 1973. The geodimeter station data were obtained from geological maps included in Special Publication 37 of the California Division of Mines and Geology dated 1972. The "nonexistent" stations were simply located on topographic maps and their elevations estimated from the contours.

The locations of the major fault lines were also obtained from the maps in Special Publication 37. The gross locations are correct to within a minute or so of latitude and longitude. However, since the intricate structure shown on geological maps is not required for our purpose, a point-by-point transformation to the topographic maps was not carried out; thus it is expected that some small segments of the faults may not be located precisely.

Table 2-1. Geographical locations of grid points for a typical network in southern California.

Station number	Station identification	Latitude	Longitude	Elevation (m)
1	LOR	36°14'.79 N	121°02'.55 W	308
2	Geod.	36 18.75	120 49.50	1367
3		36 23.75	121 04.50	305
4		36 25.00	120 58.80	832
5	Geod.	36 26.90	121 11.70	1007
6	BEN	36 30.60	121 04.53	448
7	BGM	36 35.48	121 01.52	1217
8	BVL	36 34.51	121 11.34	510
9	EMM	36 39.68	121 05.76	488
10	LWR	36 39.96	121 16.36	232
11	Geod.	36 44.70	121 13.25	697
12	FRP	36 45.22	121 29.43	705
13		36 48.25	121 27.00	305
14	LTR	36 53.07	121 18.49	183
15	DIL	36 50.12	121 38.64	204
16	CHR	36 57.46	121 35.01	241
17	FEL	36 59.00	121 24.09	323
18	PLV	36 58.62	121 49.93	158
19	CBO	37 06.71	121 41.33	192
20		37 02.60	121 57.75	973
21	GHS	37 05.75	121 26.83	778
22		37 13.40	121 35.20	610
23		37 26.30	121 42.00	1204
24	ALM	37 09.50	121 50.82	244
25	COE	37 15.46	121 40.35	366
26	SVC	37 17.11	121 46.35	128
27	Geod.	37 20.80	121 38.00	1219

Table 2-1. (Cont.)

Station number	Station identification	Latitude	Longitude	Elevation (m)
28	MSJ	37°31:25 N	121°52:23 W	498
29	MNR	37 35.68	121 38.22	500
30	PAL	37 37.88	121 57.37	463
31	MOR	37 48.68	121 48.15	792
32	MDC	37 52.90	121 54.85	1173
33	BCR	37 09.62	122 01.57	660
34	CRC	37 14.50	122 07.82	607
35	STJ	37 20.03	122 05.48	122
36	BGH	37 20.52	122 20.34	158
37	SFT	37 24.31	122 10.55	143
38		37 25.30	122 21.30	641
39		37 27.80	122 16.90	61
40	CYH	37 33.54	122 05.62	38
41	CSH	37 38.88	122 02.57	170
42	LCH	37 44.28	122 03.83	312
43	SAC	37 34.95	122 25.03	207
44		37 31.70	122 28.90	132
45	SFR	37 47.28	122 23.37	8
46	MIL	37 46.88	122 10.55	90
47	BOL	37 48.97	122 03.72	610
48	BWR	37 55.45	122 06.40	221
49		37 57.00	122 00.60	313
50	JHC	36 32.82	121 23.53	207
51	SRS	36 40.11	121 31.13	399
52	SJG	36 47.88	121 34.43	171
53	QSR	36 50.02	121 12.76	536
54	CNR	36 42.55	121 20.60	305
55	STC	36 38.10	121 14.00	259
56	EKH	36 39.88	121 10.45	342

Table 2-1. (Cont.)

Station number	Station identification	Latitude	Longitude	Elevation (m)
57		36°36'90 N	121°07'50 W	607
58		36 30.50	121 14.10	757
59		36 35.10	121 16.75	914
60		36 36.75	121 25.90	607
61		36 41.75	121 24.20	1003
62		36 44.80	121 19.50	257
63		36 54.40	121 31.50	361

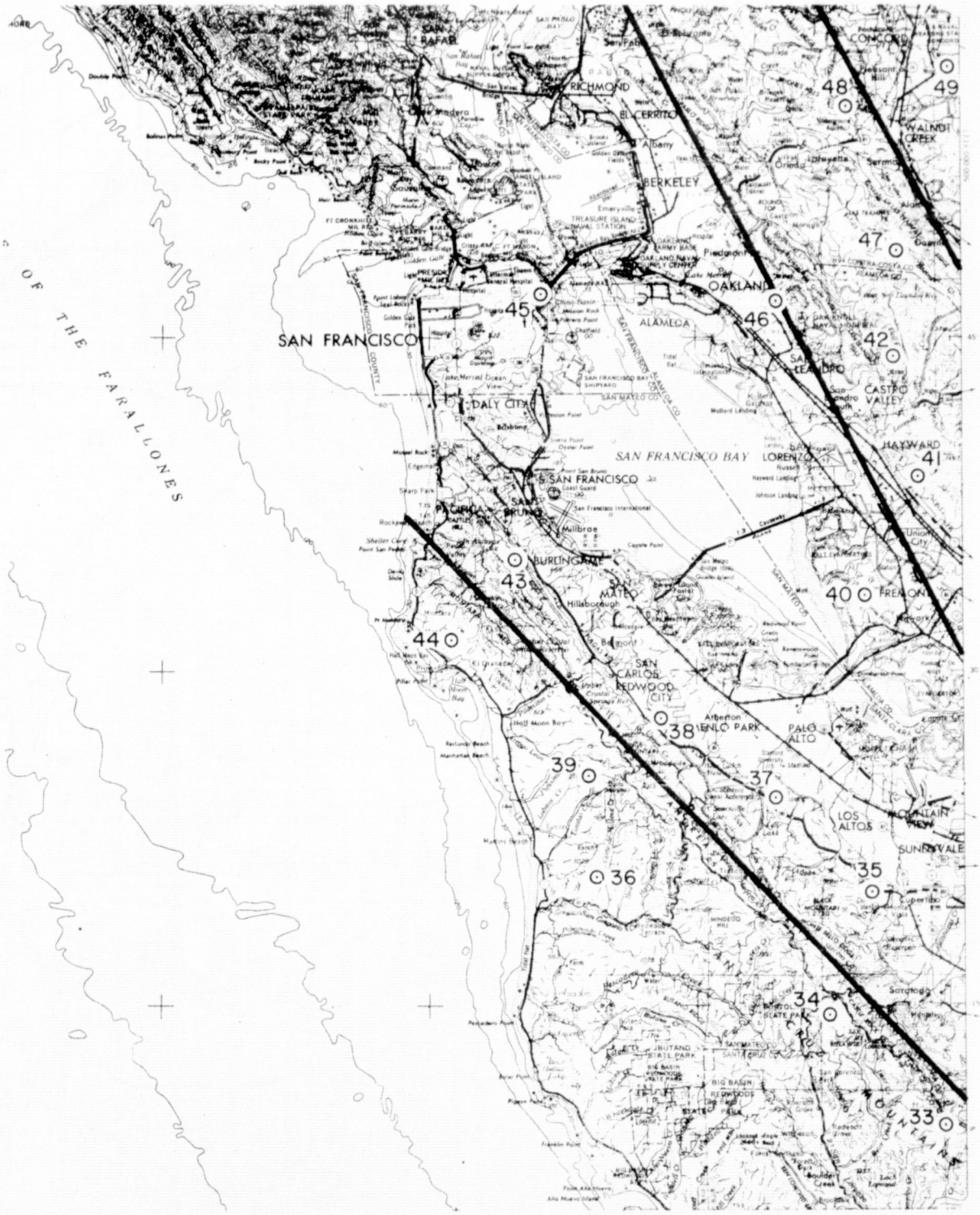

Figure 2-1. Maps showing locations of grid points for a typical network in southern California.

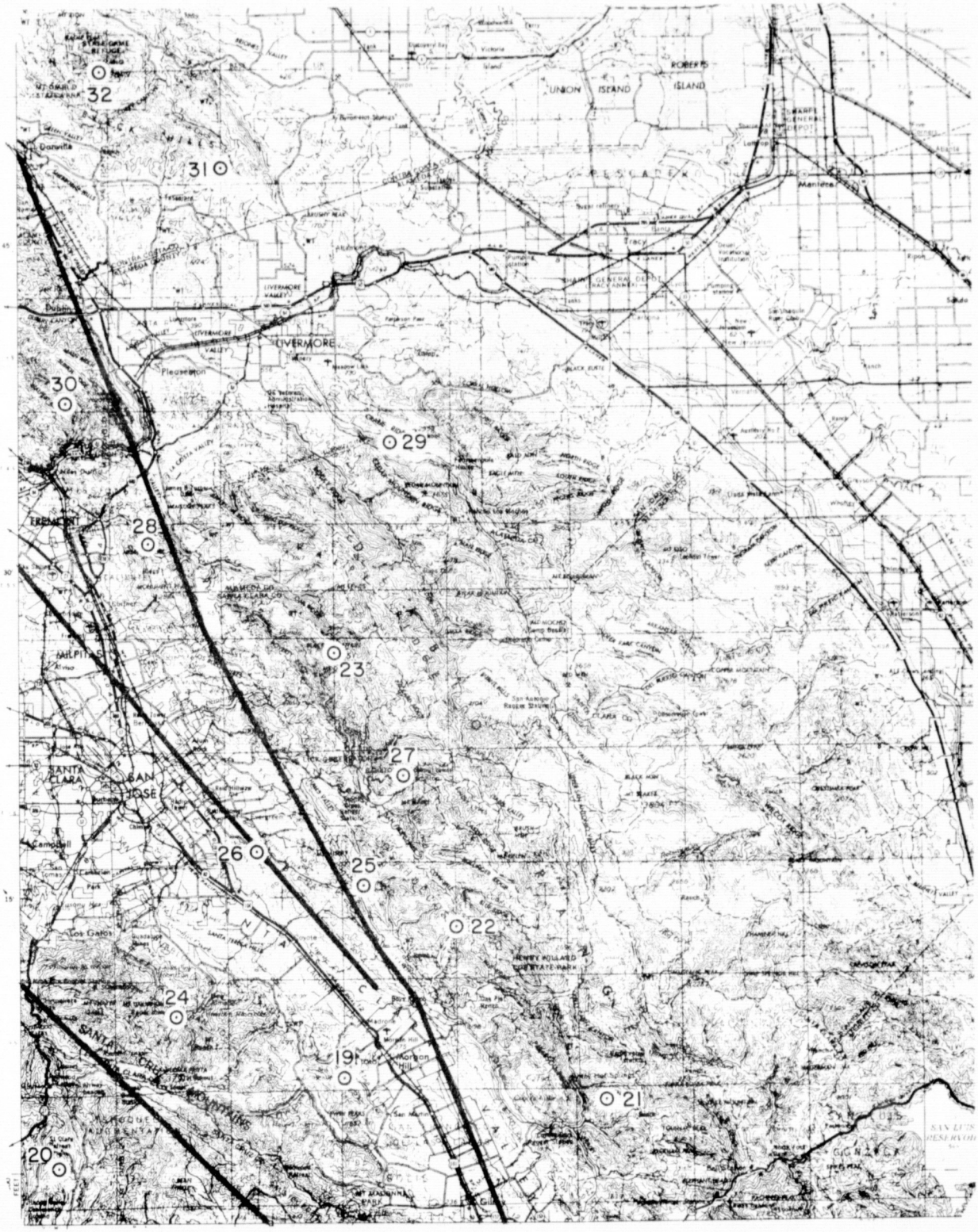

Figure 2-1. (Cont.)

Figure 2-1. (Cont.)

ORIGINAL PAGE IS
OF POOR QUALITY

3. SYSTEM CONCEPTS AND CONSTRAINTS

3.1 Introduction and Background

The basic idea behind the Clogeos concept is that under certain circumstances, it may be desirable and practical to violate a fundamental axiom of space system design: that the spacecraft systems be as simple as possible and that the complex and sophisticated instrumentation be installed on the ground. The logic that led to this "inverted" concept is outlined in the following paragraphs.

The problem that Clogeos is designed to handle is very simple: to maintain a continuous record of the distortion, in three-dimensional space, of a grid consisting of a large number of selected points spaced at intervals of 5 to 50 km over an area with linear dimensions on the order of 1000 km.

An obvious approach to this problem would be to extend the Lageos system and install many closely spaced tracking stations. Each of these stations would be equipped with a tracking telescope mount, a high-power pulsed laser, a high-speed optical detector, and the necessary timing, computing, communications, and other auxiliary facilities. However, since up to 1000 such stations might be required in a single earthquake zone, this approach is clearly impractical.

An alternative scheme, still using the passive Lageos-type satellite, would be to move a smaller number of ground stations from place to place, taking data successively at several sites with the same ground equipment. Although this technique has the advantage of requiring fewer ground instruments, each site must be carefully prepared in advance to receive the instrumentation, which must then be painstakingly emplaced in order for measurements to be made to an accuracy of 1 cm. Also, many people would be needed to move,

set up, and operate the tracking stations. From a scientific point of view, the volume of data would be reduced directly as the number of ground instruments decreased. Furthermore, by requiring that data be taken serially, rather than simultaneously from all sites, error-correction techniques such as those described in Section 4.3 cannot be effectively employed.

The Clogeos concept is based on the premise that the grid system described above can be most effectively and economically monitored by placing all the tracking equipment in the satellite and employing relatively simple ground stations at the grid points. The ground stations can be as simple as a single passive retroreflector mounted on a fixed pedestal. Although the spacecraft may require complex tracking and data-handling provisions, one such device can service hundreds or thousands of ground stations.

In very general terms, three classes of constraints occur that limit or define the nature of a satellite-based grid-location system. We discuss these in detail in the following subsections and outline them briefly below:

A. A very fundamental constraint is strictly geometric in nature and applies to all grid-location systems regardless of the hardware. These orbital constraints are based on the fact that, in certain orbits, the range or range rate from a satellite to a ground location is insensitive to some types of ground-station movements. For example, it is obviously difficult to determine the distance between two closely spaced points on the equator by making only range measurements from each point to a synchronous satellite hovering directly over the pair of sites.

It is exceedingly difficult to make very general statements concerning the sensitivity of satellite measurements under different conditions to distortions of a closely spaced grid. Therefore, we performed a set of computer simulations, using a number of satellite trajectories, to see how sensitive measurements might be to small changes in the position of a ground station (Section 3.2). The grid network is grossly oversimplified, but the results can, in general, be applied to more complex networks.

It should be noted that the choice of trajectory also affects the performance of a location system in a second way: The higher the altitude of the satellite is, the greater the slant range to the ground station will be. A greater slant range requires a higher power level from the transmitter, or a more sensitive receiver, for a given signal-to-noise ratio. For this reason, range as a function of time is illustrated in Section 3.2 for each simulated trajectory.

B. The refractive index of the troposphere establishes lower limits for the accuracy of satellite-to-ground range or range-rate systems. In many cases, as will be documented in Section 5, these errors are the dominant sources of uncertainty in navigation or location systems. Section 3.3 describes the nature of the refractive-index problem for both radio and optical frequencies and illustrates the magnitude of the errors as a function of frequency, water-vapor content, and elevation angle.

The range and range-rate errors attributable to the refractivity of the ionosphere can always be reduced to negligible proportions in the radio spectrum by transmitting two or three coherently related frequencies from the spacecraft to the ground station. This technique has been used successfully for many years in the Transit navigation systems (Guier and Weiffenbach, 1960) and will not be discussed further here. Ionospheric refractivity at all optical and millimeter-wave frequencies is negligible.

C. All satellite-to-ground location systems are limited to a certain extent by cloud cover over the ground area of interest. This constraint is far more serious for optical systems than for systems operating at radio frequencies, but we discuss cloud cover herein as a general system problem. Section 3.4 summarizes cloud-cover statistics for two areas of particular concern in this study, southern California/western Nevada and southern Alaska/Aleutian Islands. The implications of these statistics for specific system design are considered in Section 6.

3.2 Computer Simulation of the Effects of 10-mm Station Displacements

For any station location, station motions will cause variations to appear in the apparent motion of a satellite. By making and analyzing range and range-rate measurements to a satellite from a ground station, we can measure

the motion and distinguish whether the station has moved in altitude, longitude, or latitude. To demonstrate the behavior of the observed satellite motion both in range and in range rate, we ran a series of computer simulations in which the ground station was displaced 10 mm in altitude, latitude, and longitude, one coordinate at a time.

Our very simplified model includes a ground station arbitrarily located at latitude 37°N and longitude 270°E and a satellite in a slightly retrograde orbit with an inclination of 110° and an eccentricity of 0.01. The only variable is in satellite orbital altitude, for which we chose a representative sampling of 500, 1000, and 2000 km, corresponding to 15, 14, and 11 revolutions per day. Elevation angles were selected from satellite passes to cover a wide range, from low on the horizon, 25°9, to near zenith, 86°3.

The simulations involved plotting the range and range-rate error signatures that would result if the station were displaced by 10 mm in latitude, longitude, or height. All the simulations represent typical examples only, not averages of runs.

To give a sense of scale regarding the types of numbers we are dealing with, we first show range as a function of time in Figure 3-1; no station movement has yet been included. The actual distance of the satellite as seen from the ground station is plotted versus time for three passes at different elevation angles; orbital altitude is held fixed at 1000 km. Clearly, the range to the point of closest approach depends on the elevation angle — the lower the satellite is on the horizon, the farther the range from the ground station at all times. For a 25°9 elevation angle, a satellite orbiting at 1000 km never passes over a station closer than ∿1700 km; a near-zenith angle, on the other hand, would provide range measurements as close as 1000 km for this same satellite altitude.

The point is, we are measuring distances as large as 3 to 4 Mm, from which we hope to be able to pinpoint and plot deviations caused by station motion as small as 10 mm. As an example, Figure 3-2 shows the range error signature that

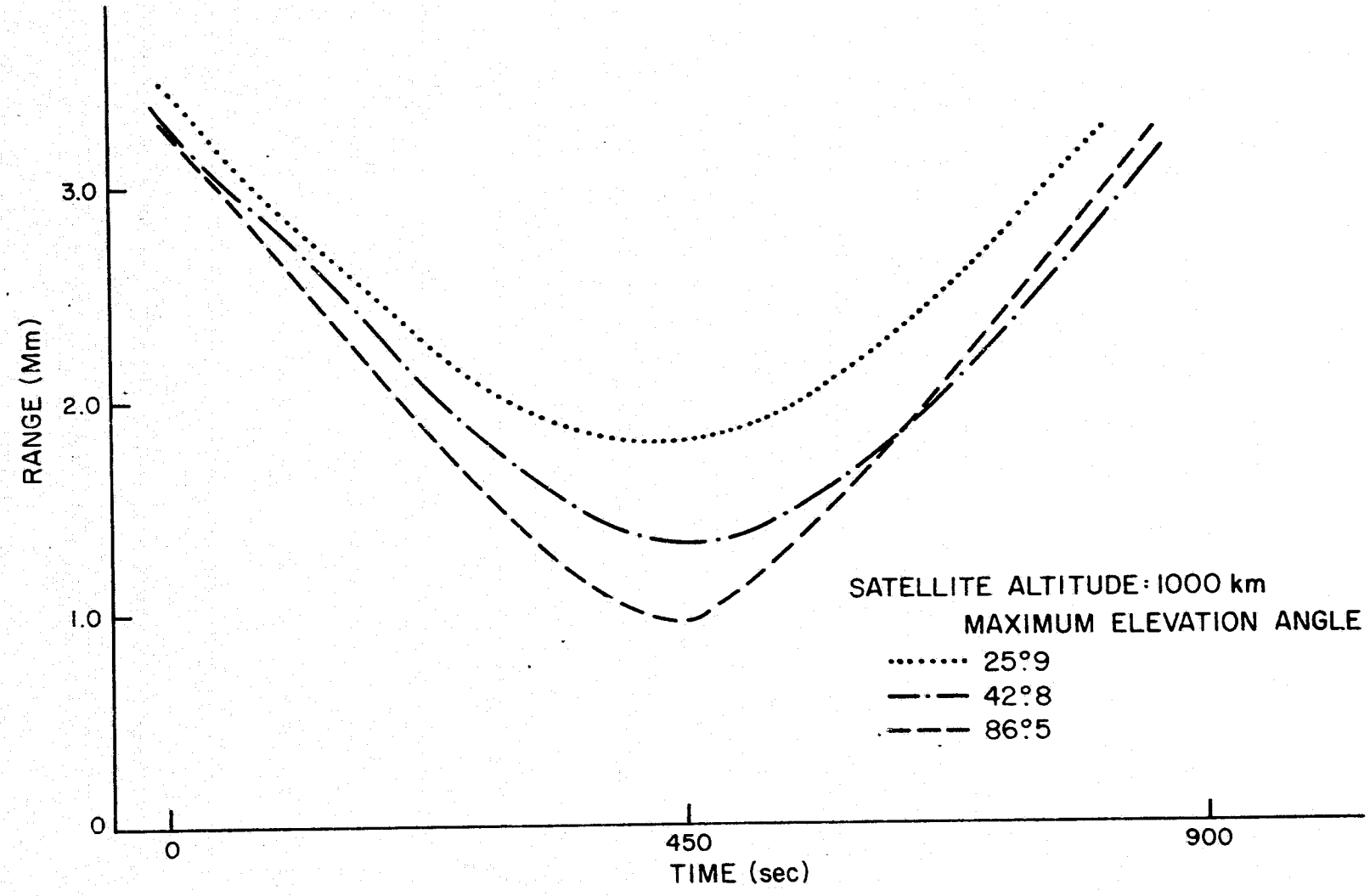

Figure 3-1. Range as a function of time before station movement.

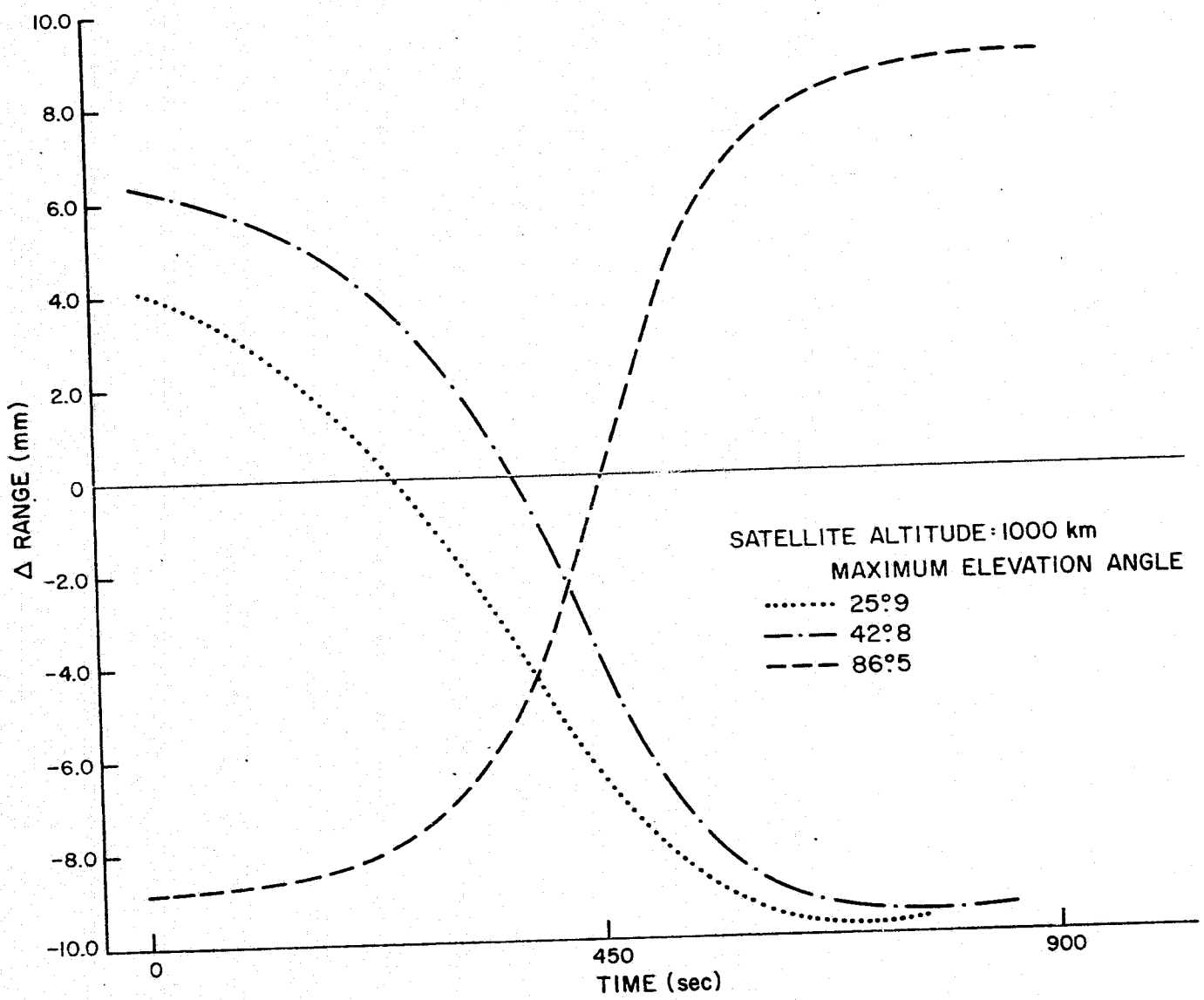

Figure 3-2. Range error signature resulting from a 10-mm latitudinal displacement.

would result if the station were displaced 10 mm in latitude. An error signature is derived by plotting range as a function of time before and after station displacement, superimposing the two curves, subtracting one from the other, and plotting the difference. The orbital characteristics are the same in both Figures 3-1 and 3-2; but whereas total range (Figure 3-1) is given in megameters, the range error signature (Figure 3-2) is measured in millimeters. Note that higher elevation angles provide more sensitive range error signatures for latitudinal displacement. A medium-angle orbit would sense a large percentage of the displacement, while low elevation angles would detect much less. Thus, for a system dependent on range measurements alone, motions in latitude will be significantly more visible from near-zenith elevation angles. A secondary advantage of high elevation angles is that less transmission power would be required for the tracking instrument.

Figure 3-3 is also shown, for comparison purposes, before station motion has been imposed. Here, range rate is plotted against time for the same three elevation angles and a 1000-km orbital altitude. As in the case of range, range-rate measurements are in general more sensitive to high elevation angles, but for points of closest approach, the difference among the three is fairly small.

Next, we took the data recorded in Figure 3-3, moved the station 10 mm north, and plotted the range-rate error signature, the difference between the range-rate measurements before and after station motion. Figure 3-4 shows the effects of a 10-mm latitudinal displacement over megameter distances. The largest observed effect, for a near-zenith 1000-km orbit, is only 0.70 mm/sec. It is also clear from Figure 3-4 that range-rate error signatures for latitudinal displacements are consistently more distinct for overhead passes, by a factor of more than 2.

Figure 3-5 plots the range error signatures resulting from displacements in station altitude and longitude for three elevation angles; the satellite is in a 1000-km orbit. Not unexpectedly, as a satellite passes almost overhead, nearly the full 10-mm displacement in station altitude is recorded. If the elevation angle is low on the horizon, the maximum sensitivity decreases to less than 5 mm.

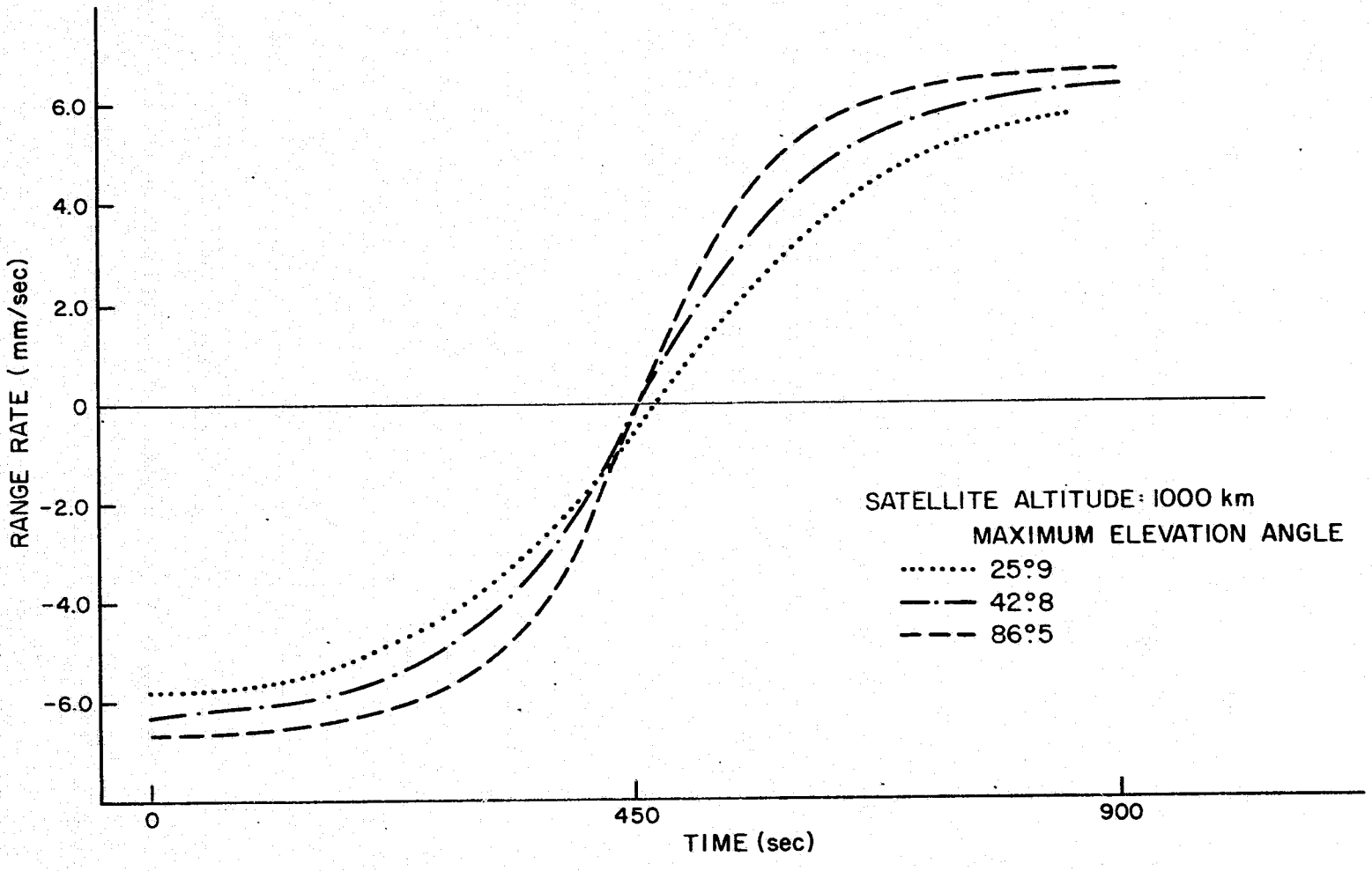

Figure 3-3. Range rate as a function of time before station movement.

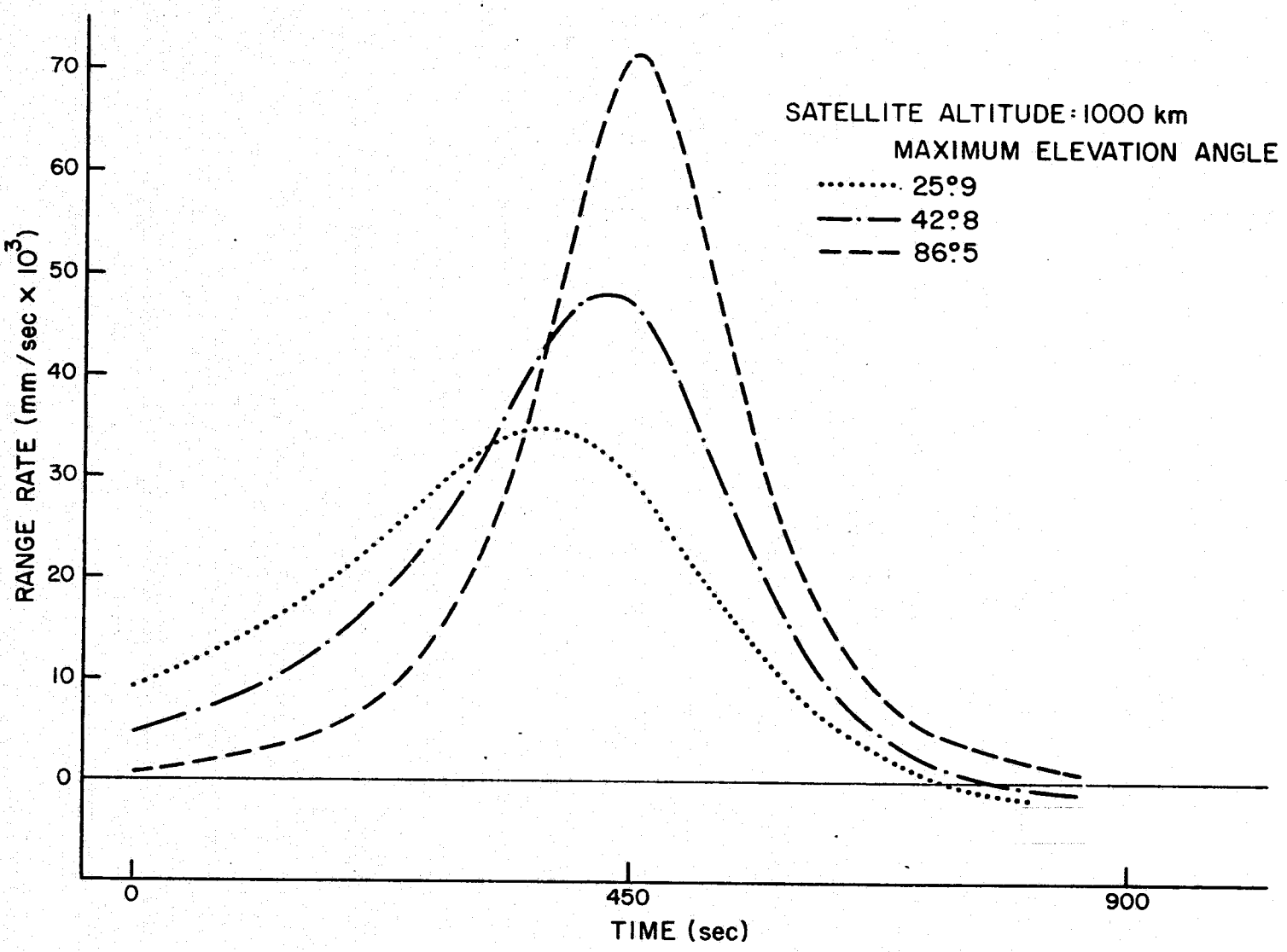

Figure 3-4. Range-rate error signature resulting from a 10-mm latitudinal displacement.

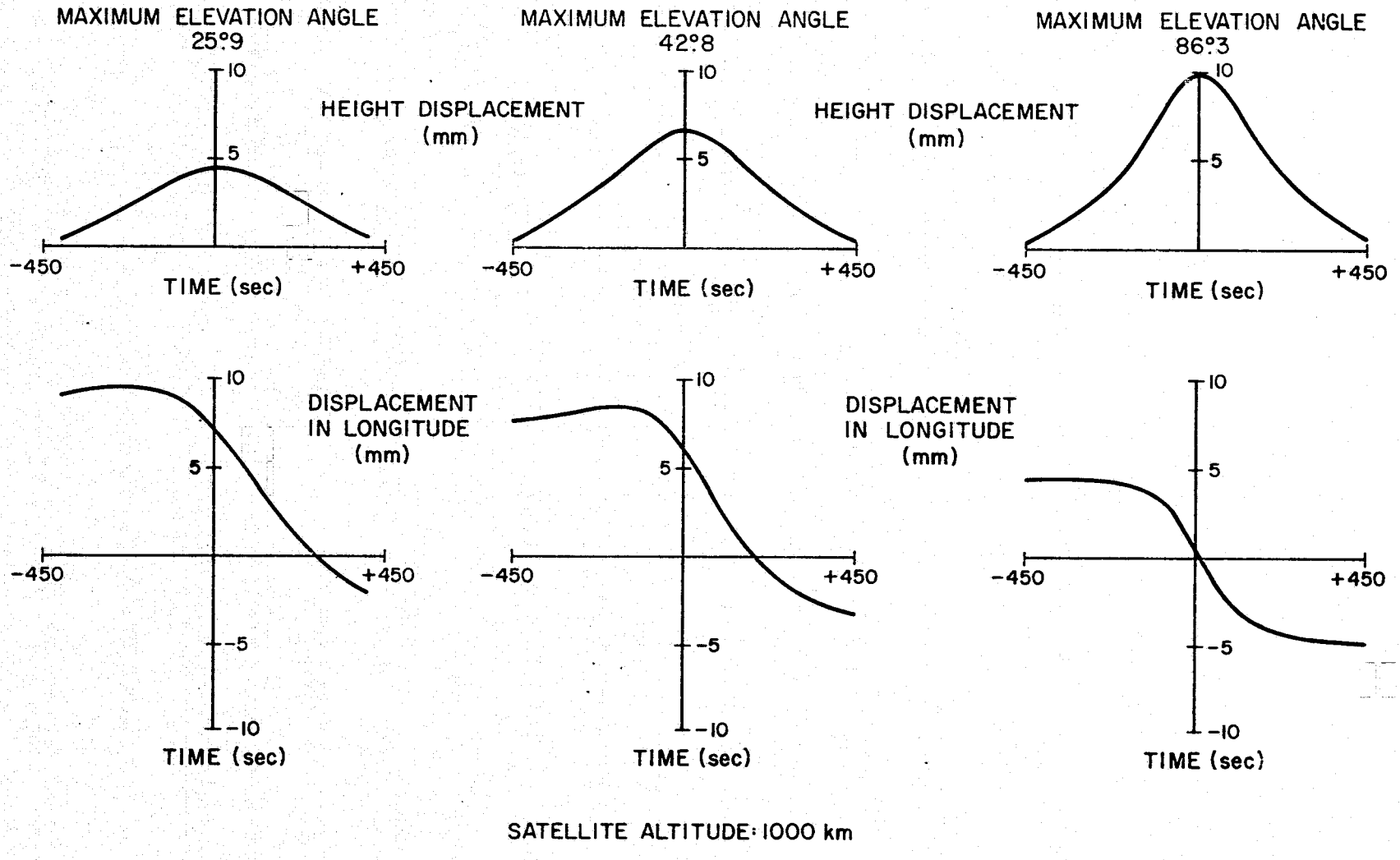

Figure 3-5. Range error signatures resulting from 10-mm displacements in station altitude (top) and longitude (bottom) for three elevation angles; satellite altitude is held constant.

For longitudinal displacements, however, low elevation angles provide better sensitivity on the whole, with medium elevation angles running a close second; high elevation angles never reveal more than ∿5 mm in displacement. Figure 3-5 is a good demonstration of the distinct differences in signatures resulting from displacements in altitude and longitude. The signature caused by an altitude change is an even function, compared to the odd function that results from a change in longitude. Of course, the error signature of general station motion will be a superposition of the signatures along the orthogonal axes.

In plotting Figure 3-6, we varied the satellite altitude and selected passes that maintained a nearly constant elevation angle. Range error signatures are shown for a hypothetical 10-mm displacement in altitude and longitude. The middle latitude curve is the same as the dotted-and-dashed curve in Figure 3-2. Whereas Figure 3-2 varied the elevation angles while maintaining a constant orbital altitude of 1000 km, Figure 3-6 shows this effect for different orbital altitudes. In general, a large percentage of the 10-mm latitudinal displacement is picked up from all three orbital altitudes, while longitudinal displacements are never fully discernible in any of the cases. Again, the signatures for displacements along the orthogonal axes are different, and a movement in latitude can be distinguished from one in longitude.

The same manipulations were performed to simulate range-rate error signatures, plotted in Figures 3-7 and 3-8, to test the sensitivity of changes in the range rate resulting from 10-mm station displacements. In Figure 3-7, we simulated an orbital altitude of 1000 km and varied the elevation angle. Plotted are range-rate error signatures for 10-mm displacements in station height and longitude. Clearly, elevation angle plays an important part in monitoring height displacements, with a low elevation angle being nearly insensitive to them. In contrast, longitudinal displacements are seen with roughly the same degree of sensitivity at any elevation angle; an overhead pass would, however, reveal a little more detail. In Figure 3-7, a displacement in height is manifested as an odd-function error signature, while a longitudinal displacement is seen as an even-function error signature. Displacements along these perpendicular axes can be readily distinguished by the shape of the signature.

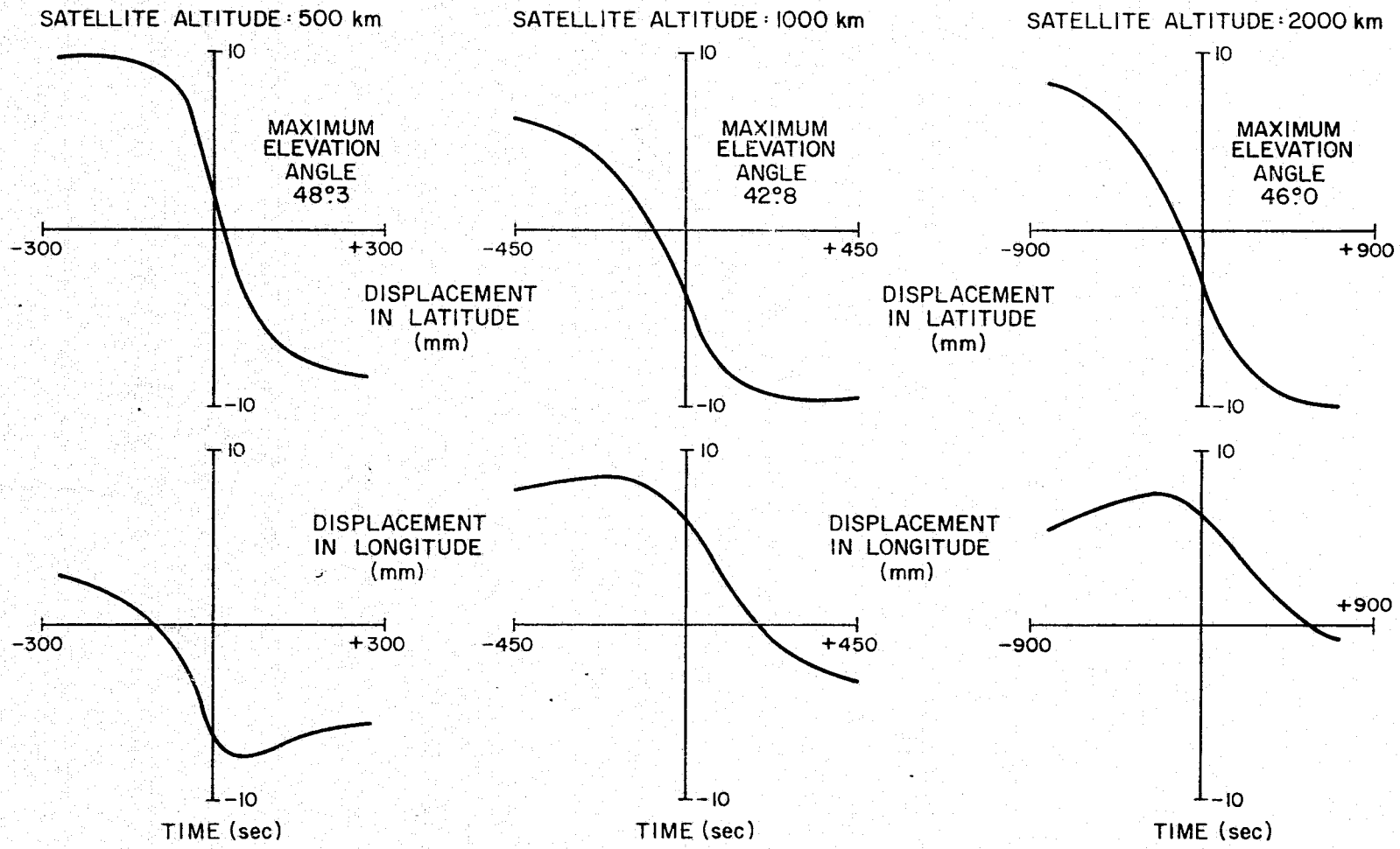

Figure 3-6. Range error signatures resulting from 10-mm displacements in station latitude (top) and longitude (bottom) for three satellite altitudes.

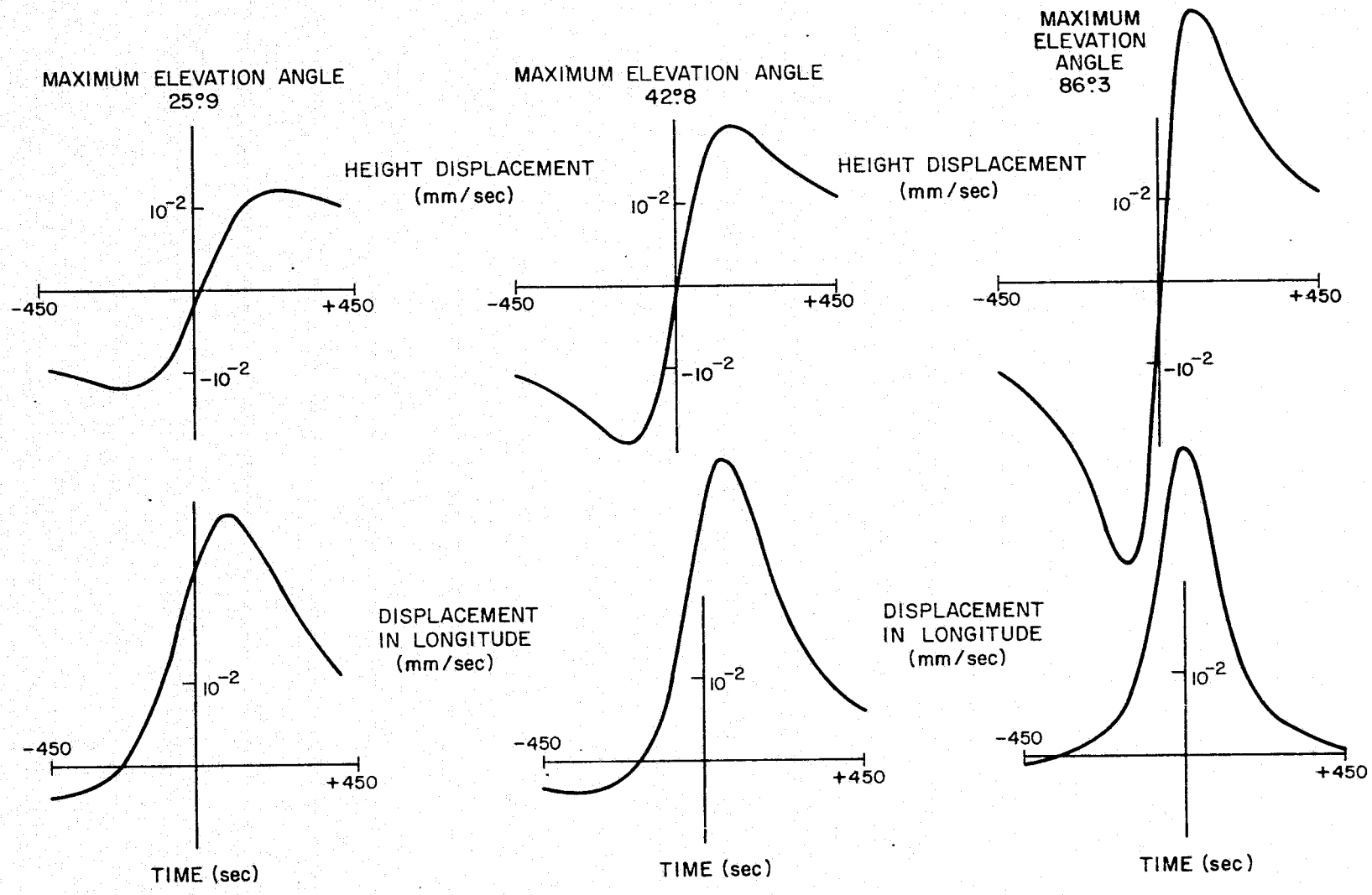

Figure 3-7. Range-rate error signature resulting from 10-mm displacements in station altitude (top) and longitude (bottom) for three elevation angles; satellite altitude is held constant.

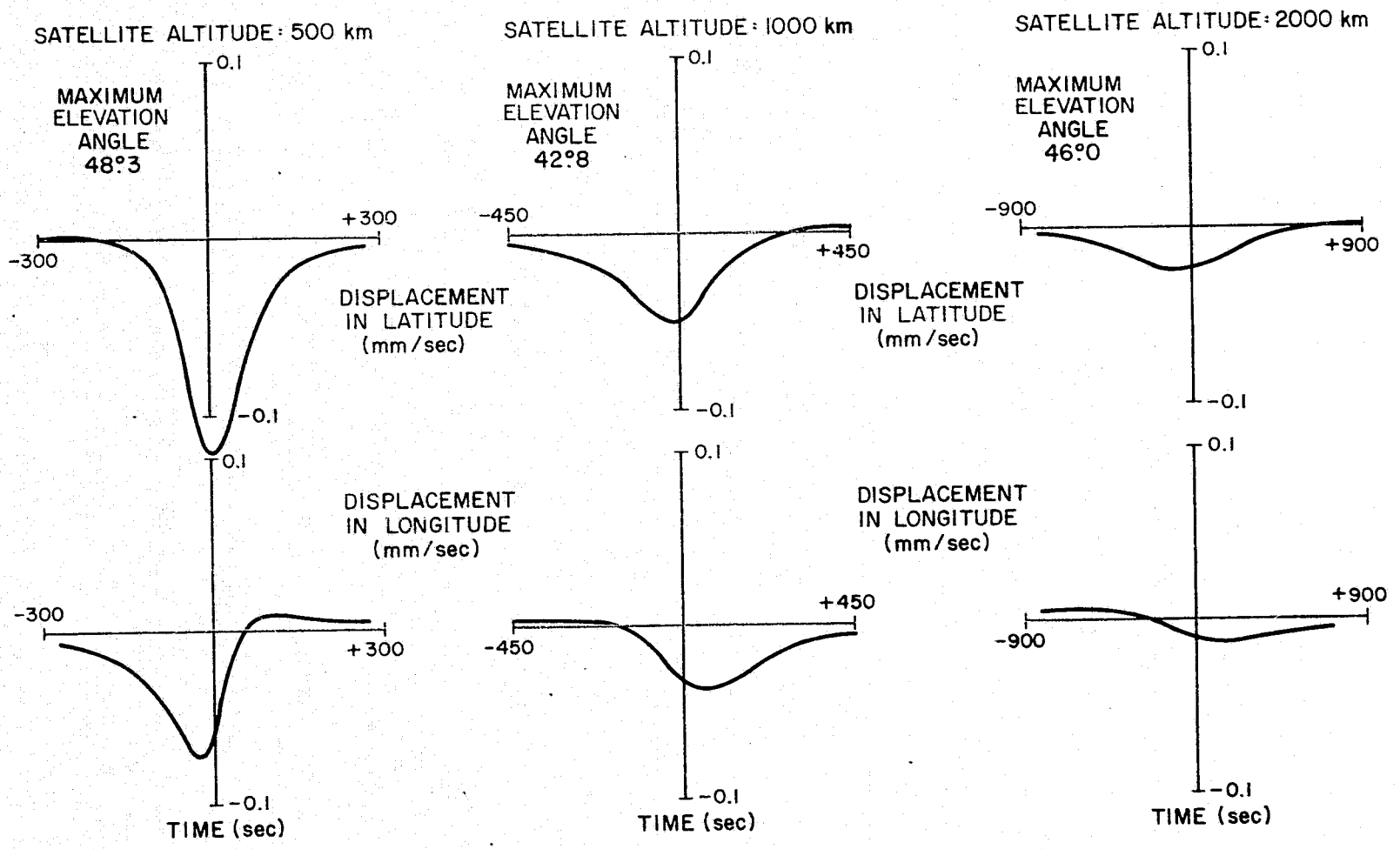

Figure 3-8. Range-rate error signature resulting from 10-mm displacements in station latitude (top) and longitude (bottom) for three satellite altitudes.

The elevation angles were held nearly constant while satellite altitude was varied in Figure 3-8, where range-rate error signatures are plotted for 10-mm displacements in station latitude and longitude. The middle curve for latitude corresponds to the dotted-and-dashed curve in Figure 3-4, in which latitude curves were shown for varying elevation angles. For both latitude and longitude, the lowest orbital altitude shows the most sensitivity, with high altitudes revealing very little about the displacements. Thus, a system dependent on range-rate measurements for measuring latitudinal and longitudinal displacements would work best for low orbital altitudes, whereas, as seen above (Figure 3-6), range systems would function somewhat better at high altitudes. Figure 3-8 is a particularly good demonstration of range-rate sensitivity and also of the difficulty of distinguishing between latitudinal and longitudinal motions by range-rate measurements, at least for selected ground stations and satellite orbits. Note that the signatures are virtually identical at low altitudes and only slightly different for the 2000-km altitude.

The computer simulations are revealing in another way: The magnitudes of the range and range-rate signatures are essential inputs to any feasibility study of a space-to-ground location system. Figures 3-2, 3-5, and 3-6 tend to confirm our intuition that a system designed to use range measurements only to detect ground-station motions on the order of 10 mm must be capable of resolving range differences of $\sim$1 mm. To distinguish between motions along the three orthogonal axes, the signature shape must be extracted down to a small fraction of the peak value of the range difference; furthermore, a 1.0-mm range resolution corresponds to a time resolution of 6.6 psec for a go-return path.

Intuition is not so helpful with respect to the range-rate error signatures. However, Figures 3-4, 3-7, and 3-8 show that a range-rate resolution of approximately 0.01 mm/sec is necessary in order to determine the characteristic signature of a displacement along a particular axis. Figure 3-8 demonstrates that for a satellite at 2000-km altitude, even the 0.01-mm/sec resolution will not be sufficient to characterize ground-station motion. If we consider that the range-rate residual errors for existing high-precision doppler-tracking systems are on the order of 0.5 to 1.0 mm/sec, it is apparent that the detection of 10-mm displacements by range-rate techniques is a formidable task.

To summarize, the decision to use a particular system to detect small station motions involves a series of tradeoffs between the sensitivity of the measurements and the type of motion experienced. For range-rate measurements, the case is relatively clear cut, in that a low-altitude, high-elevation-angle orbit would measure all three station motions — latitudinal, longitudinal, and height — with a fair degree of sensitivity. The picture is less clear for range measurements, where a high elevation angle reveals more details about height and latitudinal motions, while a low one tells more about longitudinal displacements; low altitudes are more sensitive than high ones to latitudinal and longitudinal motions, but only slightly.

3.3 Tropospheric-Induced Range Errors at Radio and Optical Frequencies

3.3.1 Introduction

Range-measurement accuracies over ground-to-spacecraft paths have a very fundamental limitation caused by the temporal and spatial variability of the refractive index of the troposphere. In a very general sense, the effect of tropospheric refractivity can be summarized as follows:

A. At radio frequencies, tropospheric refractivity consists of both a "dry" and a "wet" component. The wet component, due to water vapor in the air, is highly variable, both spatially and temporally. Typically, this component will integrate out, for a vertical path through the atmosphere, to a mean of 10 to 15 cm with a variability of ±15 cm. The contribution of the dry component to the total integrated path length is much larger than that of the wet component, with a mean value of approximately 230 cm. However, the variability of the dry-component integral is much smaller, on the order of ±2 cm.

B. The dispersion of the troposphere over the radio spectrum is extremely small. Below 10 GHz, the change in refractive index with frequency is virtually unmeasurable. Above 10 GHz, water-vapor absorption lines contribute to a very small dispersion constant.

C. At optical frequencies, the dry component dominates, with vertical integrals and variabilities similar to those encountered in the radio regimes. The variability of the wet-component integral is approximately ±2.0 mm for optical frequencies.

D. The optical spectrum exhibits a strong dispersion term, particularly at the short-wavelength end of the visible spectrum. At sea level, the refractive index at 6328 Å differs from that at 3700 Å by about 30 parts per million. The dispersion constants are known to a high degree of accuracy, and the dispersivity of the atmosphere can be usefully employed to correct for refractivity-induced range errors (Owens and Earnshaw, 1968).

Despite the fact that massive efforts have been undertaken in the past to understand and characterize the role of tropospheric refractivity on the accuracy of operational radio and optical ranging systems, the present state of knowledge is very inadequate. Many of the experiments were quite limited in time or geographical extent and so cannot be generalized with any degree of confidence. In other cases, particularly in the radio regime, the experiments were not completely documented and the results were never published in the open literature. The very extensive Mistram experiments, described in Section 3.3.3, fall into the latter category. In light of these problems, SAO sponsored a 2-day conference in June 1975 to bring together meteorologists and propagation specialists to discuss the state of the art in refractivity measurements and corrections. A summary of the conference proceedings and recommendations is included in this report as Appendix A.

Although most of the references in this and the following sections are to "range" or "ranging," the same basic considerations and theory apply to range-rate measurements (Hopfield, 1963).

3.3.2 Refractivity models at radio frequencies

The computation of average refractivity requires an estimation of N gradients with respect to the vertical height. The refractivity of air, N, can be computed by the Smith-Weintraub equation (in N units) (Bean and Dutton, 1966),

$$N = (n - 1) \times 10^6 = K_1 \frac{P}{T} + K_2 \frac{e}{T} + K_3 \frac{e}{T^2} \quad , \tag{3-1}$$

where n is the refractive index of air, P is the pressure of dry air (in mb), T is the air temperature (in °K), e is the partial pressure of water vapor (in mb),

and the constants K_1, K_2, and K_3 are related to the molecular weights of the respective constituents. Thus, errors in meteorological measurements directly correspond to those in the determination of N (assuming no errors in the equation itself). Table 3-1 lists some errors that arise in determining N from meteorological measurements. For example, by assuming errors of ±2 mb in P, ±1°C in T, and ±5% in relative humidity, RH, typical of radiosonde-measurement errors with sea-level values of P = 1014 mb, T = 15°C, and RH = 60% RH, a standard error of 4.1 N units can be obtained. Table 3-2 gives the percentage errors occurring as a result of errors in the various surface meteorological observations plus those in the constants from the Smith-Weintraub equation.

The refractivity of air at a given location is not a constant quantity, varying with time as a result of variations in atmospheric conditions. In addition, the refractive index varies for different geographic locations. Thus, the refractive profile taken at one time may not be applicable at another. Table 3-3 illustrates the relative contributions of P, T, and e to the variation of N (Bean and Horn, 1961), wherein the average summer-to-winter differences of N for arctic, temperate, and tropical conditions are tabulated. The primary contributions to ΔN at the earth's surface arise from ΔT and Δe; the effect of ΔP is negligible. Furthermore, the effects of ΔT and Δe are opposite in sign, but the total changes are all positive since $|b\ \Delta e| > |a\ \Delta T|$. This very sensitive response of N to the principal climatic elements, especially to water vapor, is an important factor to be considered. The order of magnitude of the average values of dry d_0, wet w_0, and total refractivity N_0 at the earth's surface can be seen in Table 3-4, where representative values are listed for arctic, temperate, and tropical locations (Bean, 1961). It is seen that the contribution of the wet part to the total value of N is nearly negligible in the arctic but becomes greater as the climate changes from temperate to tropical.

Thus, variations in the meteorological parameters in the troposphere cause changes in the refractive index. The tropospheric index n always has values slightly greater than unity near the earth's surface (e.g., 1.0003) and approaches unity with increasing height. A radio or optical ray propagated through the earth's troposphere therefore encounters variations in n along its trajectory, causing the

Table 3-1. Comparison of errors in determining N from meteorological measurements assuming no errors in the Smith-Weintraub equation (P = 1014 mb, RH = 60%)(errors are in N rms units).

Source of error	-50°C	0°C	15°C	40°C
Surface weather observations (P = ±1 mb, T = ±0.1°C, RH = ±1%)	±0.38	±0.43	±0.82	±2.83
Radiosonde observations (P = ±2 mb, T = ±1°C, RH = ±5%)	±1.73	±2.02	±4.07	±14.19

Table 3-2. Percentage contribution of errors in surface meteorological measurements and constants in the Smith-Weintraub equation.

Temperature (°C)	Percentage of total variance due to						Total rms error (N units)
	ΔT	Δe	ΔP	ΔK_1	ΔK_2	ΔK_3	
-50	16.7 ± 0.158	0.0 ± 0.005	81.0 ± 0.348	2.3 ± 0.059	0.0 ± 0.001	0.0 ± 0.002	0.387
0	6.2 ± 0.119	41.3 ± 0.306	35.6 ± 0.284	1.0 ± 0.048	5.7 ± 0.114	10.2 ± 0.152	0.476
15	1.8 ± 0.127	64.1 ± 0.765	7.9 ± 0.269	0.2 ± 0.045	10.0 ± 0.302	16.0 ± 0.382	0.955
40	0.3 ± 0.188	69.3 ± 2.811	0.5 ± 0.248	0.0 ± 0.040	12.7 ± 1.202	17.2 ± 0.399	3.378

Table 3-3. Relative contributions of P, T, and e to the variation of N (from Bean and Horn, 1961).

Station	Climate	Measurement altitude (km)	ΔT	a ΔT	Δe	b Δe	ΔP	c ΔP	ΔN^*
Fairbanks, Alaska	Arctic	0.0	26.8	-34.0	9.9	44.6	2	0.5	11.1
		1.0	17.2	-18.7	5.8	27.4	7	2.0	10.7
		3.0	13.1	-11.3	2.8	14.5	16	4.6	7.8
Washington, D.C.	Temperate	0.0	23.3	-29.6	17.4	78.3	0	0	48.7
		1.0	21.6	-23.5	11.9	56.2	6	1.7	34.4
		3.0	18.8	-16.2	4.3	22.2	20	5.8	11.8
Swan Island, Caribbean	Tropic	0.0	0.5	-0.6	3.0	13.5	-2	-0.5	12.4
		1.0	2.3	-2.5	2.3	10.8	-1	-0.3	8.0
		3.0	-0.7	0.6	0.6	3.1	1	0.3	4.0

*Excess of August value of N over February value of N as derived from the approximation $N = a\,\Delta T + b\,\Delta e + c\,\Delta P$, where a, b, and c are known constants.

Table 3-4. Average values of dry, wet, and total refractivity of the troposphere at the earth's surface (Bean, 1961).

Station	Climate	d_0	w_0	N_0
Isachsen (78°50'N)	Arctic	332.0	0.8	332.8
Washington, D.C. (38°50'N)	Temperate	266.1	58.5	324.6
Canton Island (2°46'S)	Tropic	259.4	111.9	371.3

ray path to become curved. When a ray is propagated in free space, where there is no atmosphere, the path followed by the ray is a straight line. To determine the "true" path length between the transmitter and the receiver, two types of corrections are required: One is the retardation correction, ΔR_n, also called the n-related correction, and the second is the correction due to ray bending, ΔR_g, also called the geometrical range correction. The total correction ΔR_e will be the sum of ΔR_n and ΔR_g. Representative values of both types of corrections at radio frequencies are shown in Table 3-5 for rays at various angles θ_0 and three different heights h of the elevation point (i.e., the point determining the upper limit to the range integral $\int n\, dh$. In general, the n-related range correction is much more important than the geometrical range correction, and in fact, the latter can be neglected at elevation angles of more than about 10° (zenith angles less than 80°). Note that at vertical incidence ($\theta_0 = \pi/2$), the range correction is finite even though the ray is theoretically straight. Table 3-5 also shows that when the terminal of a link is at vertical incidence and beyond the earth's atmosphere, a correction of 2.4 m should be applied to the measured range for average conditions. Where the ray grazes the horizon, the range error is obviously much larger.

There are several ways of estimating the refraction error to determine the true path length (or range) between the transmitter and the receiver. The range error is given by the area under the refractivity profile, i.e., $\int N\, dh$, where N at any given height is the sum of the dry and wet parts of the refractivity. If annual statistics of the N variation at a given place are taken as a criterion (see Table 3-6) to correct the range error, then the root-mean-square (rms) error of using the annual mean to represent the height error at a specific time varies for different stations from a few millimeters to 2 cm for the dry part and from 3 to 6 cm for the wet component (Hopfield, 1969). These range-error variations depend on both seasonal and weather conditions. Although the wet component is a much smaller part of the total integral (about 10%), it accounts for most of the short-period variability. The dry component is both larger (90% or more) and more stable, showing only minor seasonal and weather effects (Hopfield, 1970). The seasonal variability of the wet component is seen clearly in Figures 3-9 and 3-10; the vertical integrals therein were computed from annual statistics.

Table 3-5. Typical values of tropospheric range corrections at radio frequencies.*

θ_0 (rad)	R_0 (km)	ΔR_g (m)	ΔR_n (m)	ΔR_e (m)
		h = 1 km		
0	135	0.2	41.0	41.2
0.05	20	-	5.83	5.83
0.1	10	-	2.96	2.96
0.2	5	-	1.50	1.50
0.5	2	-	0.62	0.62
1.0	1.2	-	0.35	0.35
$\pi/2$	1	(0)	0.30	0.30
		h = 10 km		
0	410	2.6	91.5	94.1
0.05	165	0.1	30.9	31.0
0.1	95	0.02	17.23	17.25
0.2	50	-	8.97	8.97
0.5	21	-	3.76	3.76
1.0	12	-	2.14	2.14
$\pi/2$	10	(0)	1.80	1.80
		h = 110 km		
0	1265	7.6	100.7	108.7
0.05	935	0.5	38.2	38.7
0.1	720	0.12	22.27	22.39
0.2	475	0.02	11.86	11.88
0.5	225	-	5.01	5.01
1.0	130	-	2.86	2.86
$\pi/2$	110	(0)	2.41	2.41

*Values are for a standard sea-level atmosphere with $n - 1 = 320 \times 10^{-6}$.

Table 3-6. Annual statistics on $\int N\,dh$ and its components (from Hopfield, 1969).

Station	Year	$\int N_d\,dh$ (meters)		$\int N_w\,dh$ (meters)		Total $\int N\,dh$ (meters)	
		Mean	σ	Mean	σ	Mean	σ
Weather Ship E	1963	2.32546	0.01521	0.21370	0.04996	2.53916	0.05538
Weather Ship E	1965	2.32202	0.01694	0.18578	0.05174	2.50779	0.05888
Weather Ship E	1967	2.32843	0.01493	0.16647	0.05038	2.49490	0.05151
Ascension Island	1967	2.30176	0.00563	0.17516	0.03105	2.47692	0.02889
Caribou, Maine	1967	2.26051	0.01914	0.08675	0.05839	2.34727	0.05918
Washington, D.C.	1967	2.29975	0.01545	0.11671	0.06485	2.41646	0.06368
St. Cloud, Minn.	1967	2.22660	0.01800	0.08252	0.05224	2.30912	0.05140
Columbia, Mo.	1967	2.25361	0.01440	0.10922	0.06167	2.36283	0.05978
Albuquerque, New Mexico	1967	1.91237	0.01132	0.06752	0.04321	1.97989	0.04797
El Paso, Texas	1967	2.01287	0.00986	0.08923	0.05047	2.10211	0.05252
Vandenberg AFB, Cal.	1967	2.29101	0.00882	0.09298	0.03329	2.38399	0.03202
Pago Pago, Samoa	1967	2.31367	0.00492	0.25088	0.05089	2.56455	0.05101
Wake Island	1963	2.31700	0.00454	0.23929	0.05230	2.55628	0.05107
Wake Island	1965	2.31980	0.00431	0.19655	0.04698	2.51635	0.04651
Wake Island	1967	2.31756	0.00534	0.21938	0.05774	2.53694	0.05631
Majuro Island	1967	2.31261	0.00354	0.27775	0.05354	2.59036	0.05417
Point Barrow, Alaska	1967	2.30310	0.02024	0.04712	0.02862	2.35022	0.03037
Byrd Station, Antarctica	1967	1.85214	0.02115	0.01520	0.00696	1.86734	0.02461

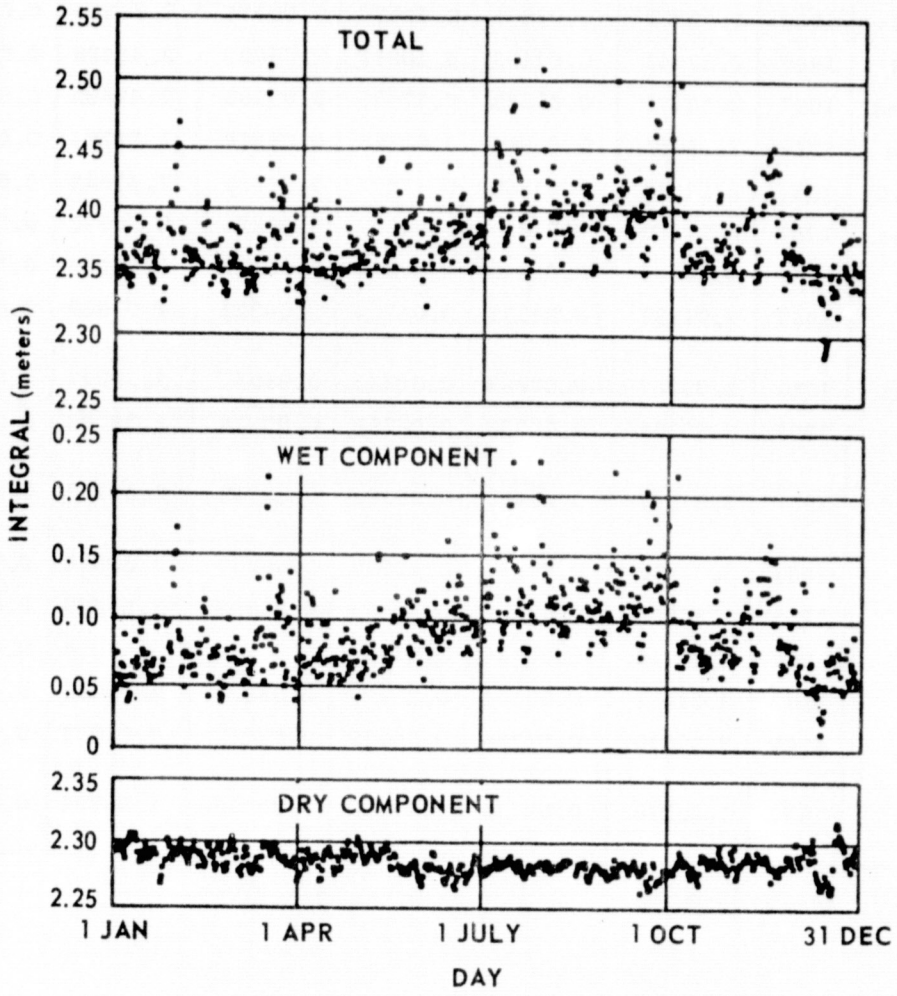

Figure 3-9. Vertical integral of refractivity at Vandenberg Air Force Base, California (lat. 34°44'N; long. 120°34'W), during 1967; balloon data (from Hopfield, 1970).

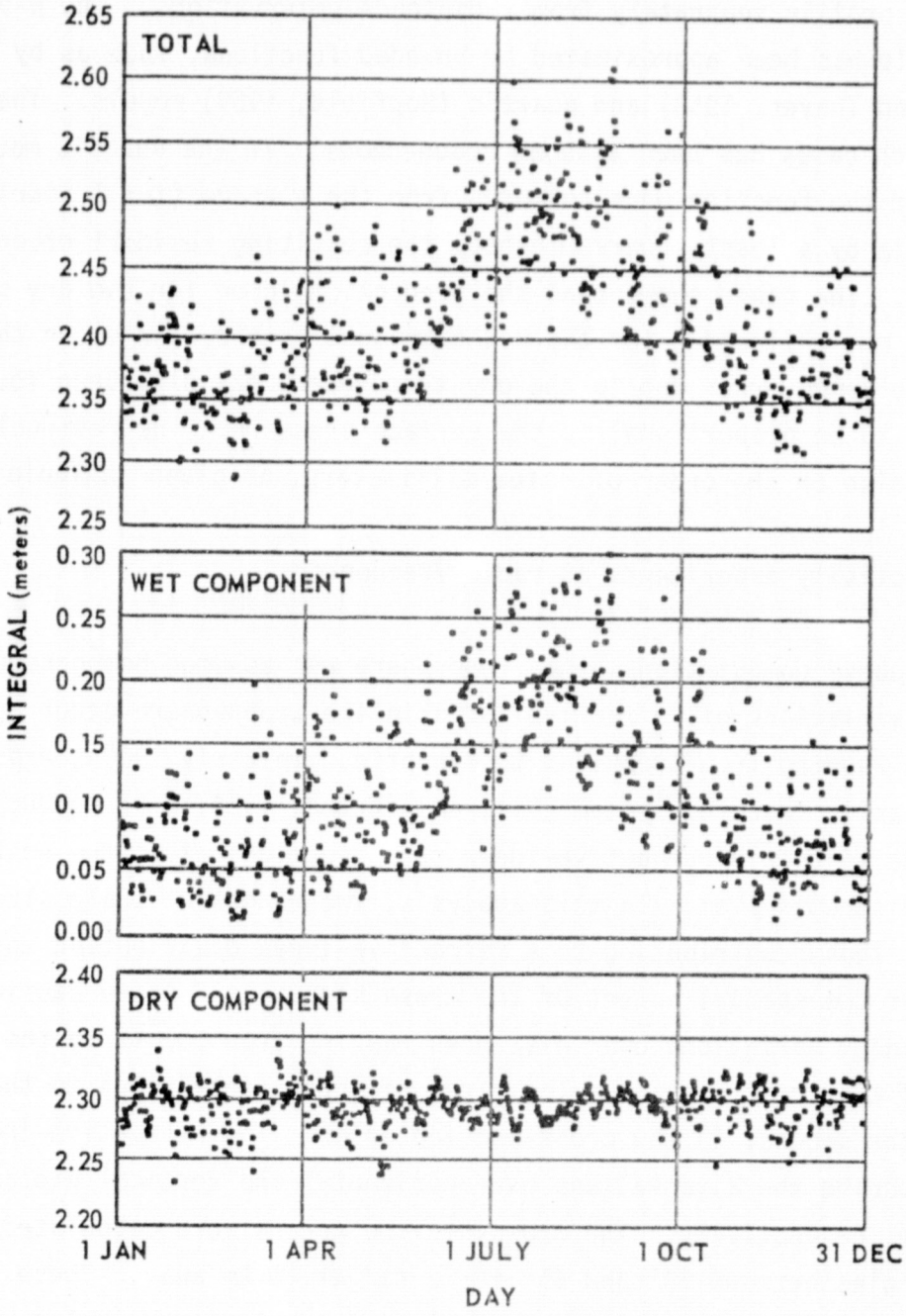

Figure 3-10. Vertical integral of refractivity at Washington, D.C. (Dulles Airport) (lat. 38°59'N, long. 77°28'W), during 1967; balloon data (from Hopfield, 1970).

Other efforts have concentrated on modeling the dry and wet parts of the refractivity profile separately from radiosonde observations. The N-versus-height profile has been approximated by bounded functions, such as by exponential (Bean and Thayer, 1958) and quartic (Hopfield, 1969) models. The troposphere in such cases has been assumed homogeneous. In the quartic model, the parameters of the function were computed from the average (for 1 year) refractivity profile by a least-squares method; the resulting residual error is given in Table 3-7. The table shows that the prediction error for the dry part is about 1 to 2 mm, while that for the wet component is very large, on the order of 5 cm. The range error due to the dry troposphere has also been found, on the average, to be proportional to the surface pressure. The residual error obtained is also on the order of a few millimeters, as given in Table 3-8.

3.3.3 Refractivity experiments at radio frequencies

In the above computations, the troposphere was assumed homogeneous, but in reality, variations of refractive index in the troposphere occur over many scale sizes, ranging from turbulent to synoptic. In early 1960s, experiments using the Missile Tracking System (Mistram) (Crane, 1964) were conducted to obtain the mesoscale refractive-index cross sections along the east-west leg of the Mistram system. In this analysis, two ranges of scale size were considered: those contributing to a refractive-index distribution that does not vary over the spatial extent of the cross section and those causing refractive-index variations over distances ranging from 500 ft to the largest dimension of the cross section. The first of these contributes to the bias error, and the second, to the cross-section error. The refractive-index cross sections describe the N variations over horizontal and vertical distances of 45 and 10 km, respectively. The cross-section errors were calculated for elevation angles between 10° and 35° for a target 10 km away. These errors apply to all heights above 10 km for the indicated elevation angles because the cross section is assumed to have a value of zero above this height.

Table 3-7. Prediction errors in the two-quartic N-profile model (from Hopfield, 1969).

Station	Year	Prediction error for $\int N_d \, dh$, σ (m)	Prediction error for $\int N_w \, dh$, σ (m)
Weather Ship E	1963	0.001372	0.028123
Weather Ship E	1965	0.001423	0.027883
Weather Ship E	1967	0.001509	0.032824
Ascension Island	1967	0.001127	0.021204
Caribou, Me.	1967	0.001548	0.027642
Washington, D.C.	1967	0.001008	0.030072
St. Cloud, Minn.	1967	0.001308	0.023500
Columbia, Mo.	1967	0.001569	0.028744
Albuquerque, N.M.	1967	0.001393	0.016624
El Paso, Tex.	1967	0.001635	0.025084
Vandenberg AFB, Cal.	1967	0.001475	0.024808
Pago Pago, Samoa	1967	0.001684	0.045408
Wake Island	1963	0.001418	0.033192
Wake Island	1965	0.001531	0.032717
Wake Island	1967	0.001669	0.044369
Majuro Island	1967	0.001489	0.049702
Point Barrow, Ala.	1967	0.001261	0.017658
Byrd Station, Antarctica	1967	0.001091	0.005542

Table 3-8. Prediction of $\int N_d\, dh$ from surface pressure: $\int N_d\, dh = kP_s$ (from Hopfield, 1969).

Station	Year	Latitude	Longitude	Height (m)	k (m/mb)	Prediction error in $\int N_d\, dh$, σ (m)
Weather Ship E	1963	35°N	48°W	10	0.002281504	0.0017736
Weather Ship E	1965	35 N	48 W	10	0.002281285	0.0016183
Weather Ship E	1967	35 N	48 W	10	0.002281130	0.0016839
Ascension Island	1967	7°55'S	14°24'W	79	0.002290524	0.0011532
Caribou, Me.	1967	46 52 N	68 01 W	191	0.002277725	0.0019329
Washington, D.C. (Dulles Airport)	1967	38 59 N	77 28 W	85	0.002280275	0.0020481
St. Cloud, Minn.	1967	45 35 N	94 11 W	318	0.002278233	0.0015620
Columbia, Mo.	1967	38 58 N	92 22 W	239	0.002280504	0.0019135
Albuquerque, N.M.	1967	35 03 N	106 37 W	1620	0.002280765	0.0014815
El Paso, Tex.	1967	31 48 N	106 24 W	1193	0.002282555	0.0016598
Vandenberg AFB, Cal.	1967	34 44 N	120 34 W	100	0.002280797	0.0015237
Pago Pago, Samoa	1967	14 20 S	170 43 W	5	0.002287643	0.0017371
Wake Island	1963	19 17 N	166 39 E	5	0.002286083	0.0015023
Wake Island	1965	19 17 N	166 39 E	5	0.002286238	0.0015791
Wake Island	1967	19 17 N	166 39 E	5	0.002286287	0.0017215
Majuro Island	1967	7 05 N	171 23 E	3	0.002289389	0.0015692
Point Barrow, Ala.	1967	71 18 N	156 47 W	8	0.002273335	0.0014273
Byrd Station, Antarctica	1967	80 01 S	119 32 W	1543	0.002272051	0.0011065

The Mistram experiments included three sites, at Mistram Central (MC) in Valkaria, Florida, 10 km west of MC (10 km), and 100 km west of MC (100 km). The cross-section errors for each of these sites are given in Figures 3-11, 3-12, and 3-13 for three consecutive days. One percent of the bias range error for a target at 10 km is plotted for reference.

We see in Figure 3-11 that the rays from the MC and 10-km sites lie in the clear (cloud-free) region over the range of elevation angles shown. For θ_0 = 10° to 20°, the 10-km ray sweeps through the region of space with a variation in refractivity of +10. This region contributes to the peak in the range error curve at $\theta_0 \sim 10°$. As the 100-km ray sweeps up, it traverses the cloud (which has high ΔN values), and the cross-section range error drops.

In Figure 3-12, MC rays for $\theta_0 < 18°$ and 10-km rays for $\theta_0 < 13°$ pass under sea-breeze-induced clouds. The cross-section range errors increase for higher elevation angles as the rays go through the clouds. The 100-km rays pass through clouds at $\theta_0 \sim 25°$, resulting in a rapid change in cross-section range error with increasing elevation angle.

The 10-km rays in Figure 3-13 traverse the sea-breeze clouds at $\theta_0 > 10°$; above 20°, the rays pass through a region of low ΔN in the center of the clouds.

3.3.4 Refractivity models at optical frequencies

As mentioned earlier, radio waves are very sensitive to tropospheric water vapor, which causes fluctuations in the refractivity profile. This can largely be overcome by using optical frequencies. Table 3-9 illustrates the dependence of refractivity and group refractivity on pressure, temperature, and humidity at 6329.9 Å (Owens and Earnshaw, 1968). It is clear therein that the effect of humidity on the refractive index for optical frequencies is much smaller than that for radio waves. The small dependence of humidity on the group refractivity is also seen for those applications in which modulated light is used. For pressure variations, Erickson (1962) found experimentally that the relative refractivity of dry air varies by less than 3×10^{-6} for a change in pressure of 0.5 atm.

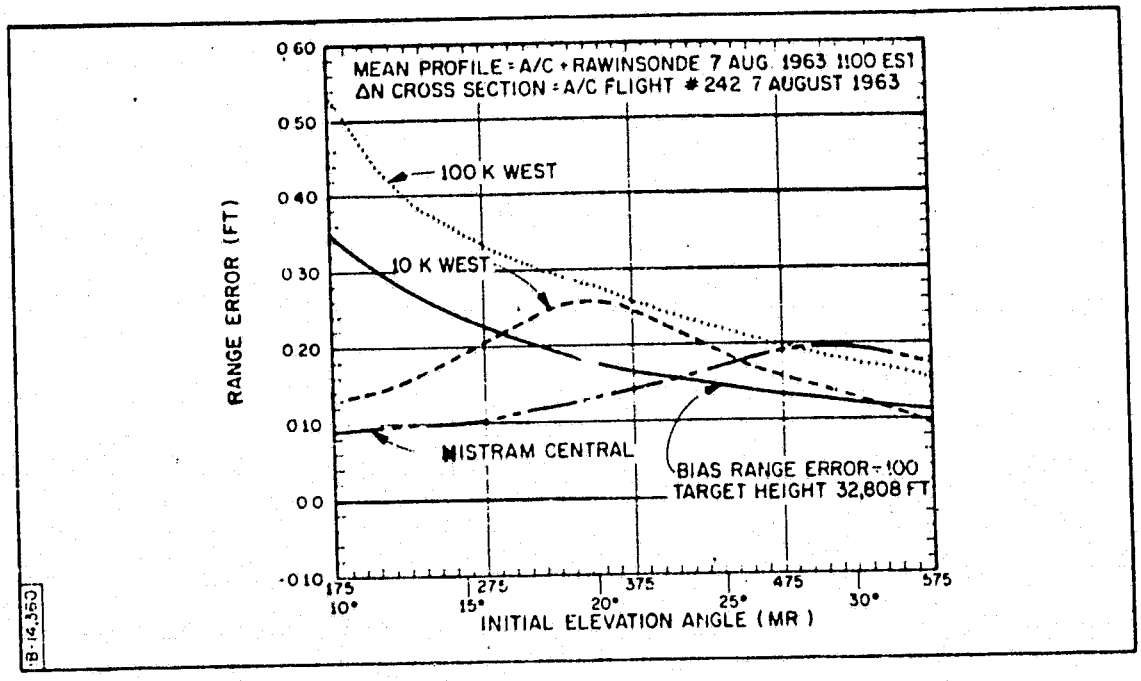

Figure 3-11. Cross-section range error from Mistram sites on 7 August 1963 (from Crane, 1964).

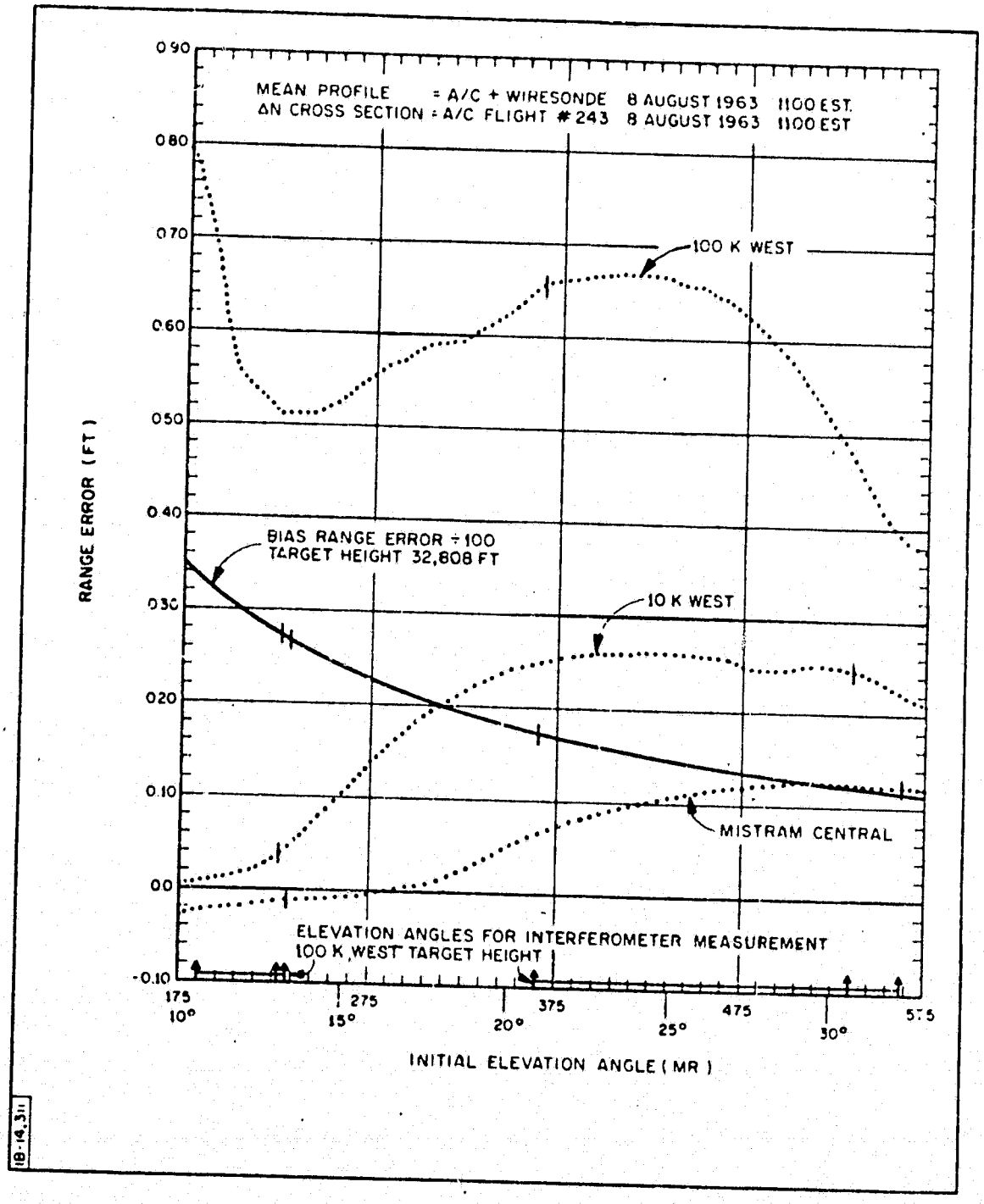

Figure 3-12. Cross-section range error from Mistram sites on 8 August 1963 (from Crane, 1964).

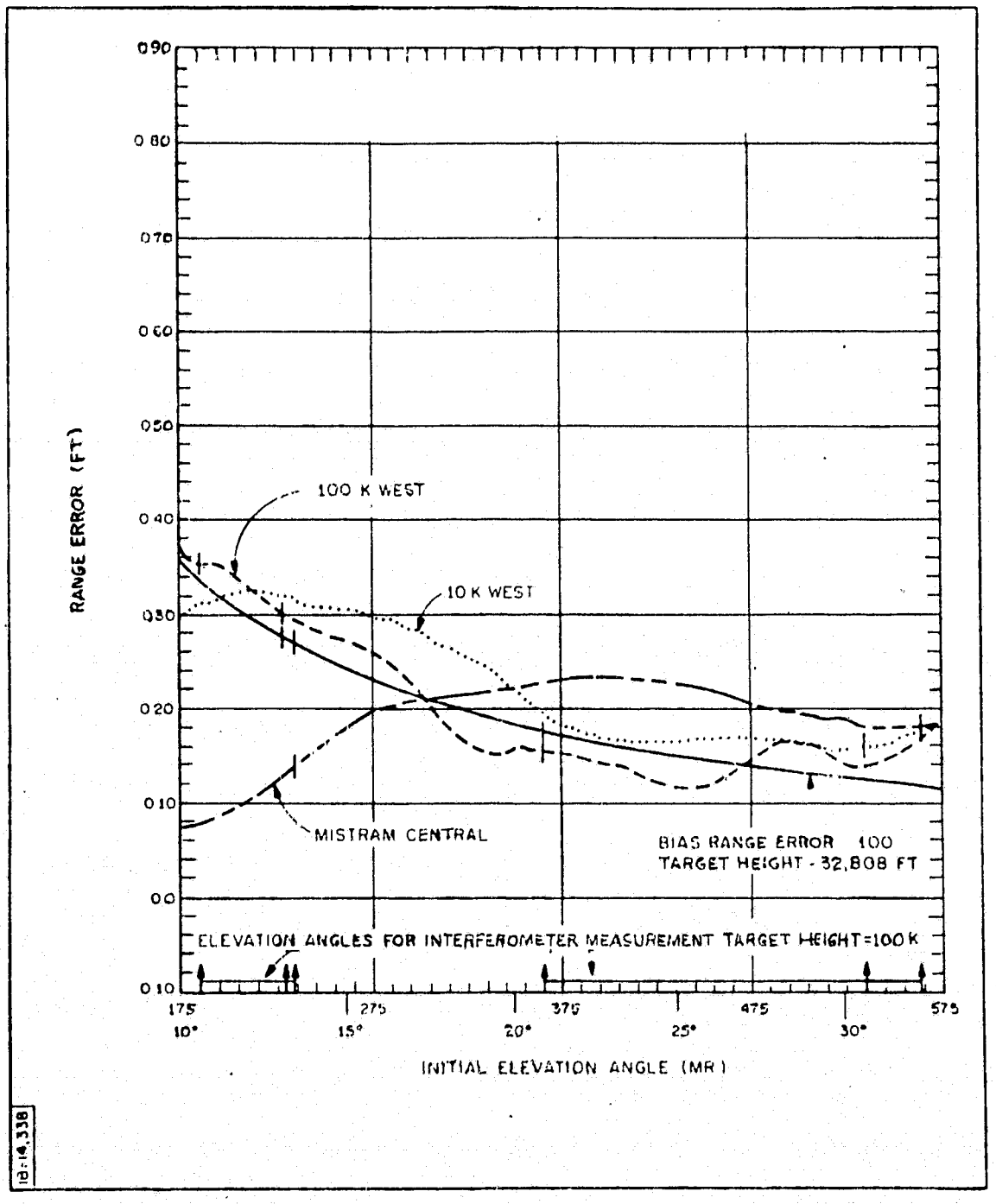

Figure 3-13. Cross-section range error from Mistram sites on 9 August 1963 (from Crane, 1964).

Table 3-9. Examples of the dependence of tropospheric refractivity and group refractivity on pressure, temperature, and relative humidity.

Pressure (mb)	Temperature (°C)	Relative humidity (%)	Refractivity at 6329.9 Å ($\times 10^6$)	Group refractivity at 6358 Å ($\times 10^6$)
		Pressure dependence		
250	15	0	68.201	
500	15	0	136.418	
1000	15	0	272.900	
1500	15	0	409.445	
		Temperature dependence		
1000	-30	0	323.551	364.271
1000	-15	0	304.705	343.013
1000	15	0	272.900	307.182
1000	45	0	247.093	278.147
1000	60	0	235.932	265.599
		Humidity dependence		
1000	15	0	272.900	307.182
1000	15	50	272.542	
1000	15	100	272.183	306.589
1000	45	0	247.093	278.147
1000	45	50	245.077	
1000	45	100	243.061	275.190

For atmospheric air, the refractive index is given by (Owens and Earnshaw, 1968)

$$\frac{n^2 - 1}{n^2 + 2} = R_1\rho_1 + R_2\rho_2 + R_3\rho_3 \quad , \tag{3-2}$$

where R_1, R_2, and R_3 are the specific refractions of dry CO_2-free air, water vapor, and CO_2, respectively, and ρ_1, ρ_2, and ρ_3 are the corresponding partial densities.

Standard (dry CO_2-free) air is defined as being dry and having a temperature of 15°C, a total pressure of 1013.25 mb, and the following composition by molar percentage: 78.09% N_2, 20.95% O_2, 0.93% Ar, and 0.03% CO_2. The refractivity of dry CO_2-free air of otherwise standard composition is obtained by dividing Edlén's (1966) dispersion formula for standard air by 1.000162 to remove the effects of CO_2:

$$R_1 \times 10^8 = (n - 1) \times 10^8 = 8340.78 + \frac{2405640}{130 - \sigma^2} + \frac{15994}{38.9 - \sigma^2} \quad , \tag{3-3}$$

where $\sigma = 1/\lambda_{vac}$ is the vacuum wavenumber (in inverse microns). The partial density ρ_1 is given by

$$\rho_1 = 348.328 \frac{P_1}{T}\left[1 + P_1\left(57.90 \times 10^{-8} - \frac{0.94581 \times 10^{-3}}{T} + \frac{0.25844}{T^2}\right)\right] \quad , \tag{3-4}$$

where P_1 is the partial pressure. Formulas (3-3) and (3-4) are valid for the following conditions:

$$2302 < \lambda < 20586 \text{ Å} \quad ,$$

$$240 < T < 330 \text{ K} \quad ,$$

$$0 < P_1 < 4 \text{ atm} \quad .$$

The refractivity of water vapor, the most important of the variable constituents of atmospheric air, is given by

$$R_2 \times 10^8 = 295.235 + 2.6422\sigma^2 - 0.032380\sigma^4 + 0.004028\sigma^6 \quad , \qquad (3\text{-}5)$$

and the density ρ_2 is given by

$$\rho_2 = 221.297 \frac{P_2}{T} \left\{ 1 + P_2 \left[1 + P_2(3.7 \times 10^{-4}) \right] \times \left(-2.37321 \times 10^{-3} + \frac{2.2336}{T} - \frac{710.792}{T^2} + \frac{7.75141 \times 10^4}{T^3} \right) \right\} \quad , \qquad (3\text{-}6)$$

where P_2 is the partial pressure. Equations (3-5) and (3-6) are valid for the following conditions:

$$3611 < \lambda < 6440 \text{ Å} \quad ,$$

$$250 < T < 320 \text{ K} \quad ,$$

$$0 < P_2 < 100 \text{ mb} \quad .$$

Although the effects of CO_2 are usually small, situations occur in which an abnormally high CO_2 content could cause a noticeable error. For the conditions P = 1013.25 mb and T = 15°C, the dispersion formula can be obtained from Edlén's formula for 15°C and 1013.25 mb,

$$R_3 \times 10^8 = 22822.1 + 117.8\sigma^2 + \frac{2406030}{130 - \sigma^2} + \frac{15997}{38.9 - \sigma^2} \quad . \qquad (3\text{-}7)$$

The density is represented as follows:

$$\rho_3 = 529.37 \frac{P_3}{T} \quad . \qquad (3\text{-}8)$$

Equations (3-7) and (3-8) are valid for

$$2379 < \lambda < 6910 \text{ Å} \quad ,$$

$$240 < T < 330 \text{ K} \quad ,$$

$$0 < P_3 < 14 \text{ mb} \quad .$$

In theory, equations (3-3) to (3-8) can be substituted into equation (3-2) to obtain a general formula for the refractive index of air. However, we can derive a simpler equation from the approximation

$$\frac{n^2 - 1}{n^2 + 2} = \frac{2(n - 1)}{3}\left(1 - \frac{n - 1}{6}\right) \quad . \tag{3-9}$$

Thus, by combining equations (3-3) through (3-9), the refractivity of air is given by

$$N = (n - 1) \times 10^8 = D_d\left(2371.34 + \frac{683939.7}{130 - \sigma^2} + \frac{4547.3}{38.9 - \sigma^2}\right)$$

$$+ D_w(6487.31 + 58.058\sigma^2 - 0.71150\sigma^4 + 0.08851\sigma^6) \quad , \tag{3-10}$$

where the density factors D_d and D_w for dry air and water vapor are given by

$$D_d = \frac{P_d}{T}\left[1 + P_d\left(57.90 \times 10^{-8} - \frac{9.3250 \times 10^{-4}}{T} + \frac{0.25844}{T^2}\right)\right] \tag{3-11}$$

and

$$D_w = \frac{P_w}{T}\left(1 + P_w\left\{\left[1 + P_w(3.7 \times 10^{-4})\right]\right.\right.$$

$$\left.\left. \times \left(-2.37321 \times 10^{-3} + \frac{2.2366}{T} - \frac{710.792}{T^2} + \frac{7.75141 \times 10^4}{T^3}\right)\right\}\right) \quad . \tag{3-12}$$

For applications in which modulated light is used, the group velocity v rather than phase velocity is required. The group refractive index n_g is related to the refractive index of air by

$$n_g = n + \sigma \frac{dn}{d\sigma} \quad . \tag{3-13}$$

Differentiating equation (3-10) and substituting it into equation (3-13), we get a simplified formula (Owens and Earnshaw, 1968) for the group refractive index,

$$(n_g - 1) \times 10^8 = D_d \left[2371.34 + 683939.7 \frac{130 + \sigma^2}{(130 - \sigma^2)^2} + 4547.3 \frac{38.9 + \sigma^2}{(38.9 - \sigma^2)^2} \right] + D_w (6487.31 + 174.174\sigma^2 - 3.55750\sigma^4 + 0.61957\sigma^6) \quad , \tag{3-14}$$

with D_d and D_w as given above.

Thayer (1967) used a slightly different formula for tropospheric refractivity. After ignoring trace gases and absorbing the effects of CO_2 in the dry term, the refractivity is given by

$$n - 1 = D(\sigma)\ f(P,T) + W(\sigma)\ g(e,T) \quad , \tag{3-15}$$

where $D(\sigma)$ is the dispersive constant, $f(P,T)$ is a function of pressure and temperature for dry air, $W(\sigma)$ is the dispersive constant for the water-vapor term at wavenumber σ, and $g(e,T)$ is the atmospheric dependence of the water-vapor term as a function of water-vapor pressure and temperature, as follows:

$$D(\sigma) = \left(66.8668 + \frac{28752.04}{144 - \sigma^2} + \frac{248.16}{40.9 - \sigma^2}\right) \times 10^{-6} \tag{3-16}$$

and

$$f(P,e,T) = 0.2840583 \left(\frac{P - e}{T}\right) [1 + (7.8681 - 0.1178t) \times 10^{-7}(P - e)] \quad , \tag{3-17}$$

where t is the temperature of the air. Similarly, for water-vapor terms,

$$W(\sigma) = 0.961646 + 0.0086062\sigma^2 - 0.00010546\sigma^4 + 0.00001312\sigma^6 \tag{3-18}$$

and

$$g(e,T) = 67.54 \left(\frac{e}{T}\right) [1 + (24 - 0.2t) \times 10^{-6} e] \times 10^{-6} \quad . \qquad (3\text{-}19)$$

It should be mentioned that for optical wavelengths between 3000 and 16000 Å, the refractive index has been determined to a very high degree of accuracy (a few parts in 10^8) for both dry air of standard composition and the moist term (the accuracy of the water-vapor term is better than $\pm 2 \times 10^{-8}$ for $t < 40°C$).

From equations (3-13) and (3-16) to (3-19), we can write the group-refractivity formula as follows:

$$(n_g - 1) \times 10^6 = \left[66.8668 + \frac{28752.04}{144 - \sigma^2}\left(1 + \frac{2\sigma^2}{144 - \sigma^2}\right)\right.$$

$$+ \frac{248.16}{40.9 - \sigma^2}\left(1 + \frac{2\sigma^2}{40.9 - \sigma^2}\right) f(P,T) + (0.961646$$

$$\left. + 0.0258186\sigma^2 - 0.00052730\sigma^4 + 0.00009184\sigma^6)\ g(e,T)\right] \quad . \qquad (3\text{-}20)$$

3.3.5 Refractivity-error estimation at optical frequencies

The previous section was concerned with the physical mechanisms of refractive-index variations in the troposphere at optical frequencies. Herein, we discuss several techniques for measuring the average refractive index over ground-to-spacecraft paths.

Multiple-frequency systems exploit the dispersive nature of the refractive index of air in the optical regime. By measuring the apparent path length R at two optical frequencies, the total tropospheric content between the spacecraft and the ground station can be accurately estimated. The true path length L can then be calculated by using the refractivity data described in Section 3.3.4. This technique leaves a small error due to the unknown water-vapor content of the air in the path of the measurement. Since the refractivity of air at radio frequencies is very sensitive to the presence of water vapor, the triple-frequency systems add a radio-frequency link to the two optical links, providing a means of estimating the contribution of water vapor to the range error.

The theory of the dual-frequency approach can be summarized briefly by first assuming that the refractive index of air is a function only of the density of dry air. Then it follows that the group refractive index is approximately

$$n_g - 1 = D(\sigma)\, f(P,T) \quad . \tag{3-21}$$

The true path length is then approximately

$$L = R - D(\sigma) \cdot \overline{f(P,T)} \cdot L \quad , \tag{3-22}$$

where the bar indicates an average over the path. If two range measurements at two different optical wavelengths, σ_1 and σ_2, are made over the same path, the range difference $\delta R_{2,1}$ will be

$$\delta R_{2,1} = \overline{f(P,T)} \cdot L[D(\sigma_2) - D(\sigma_1)] \quad . \tag{3-23}$$

Substituting equation (3-23) into equation (3-22) yields

$$L = R_1 - \left[\frac{D(\sigma_1)}{D(\sigma_2) - D(\sigma_1)} \cdot \delta R_{2,1}\right] \quad , \tag{3-24}$$

where R_1 is the range measured with light at wavelength σ_1. Equation (3-24) does not contain terms contingent on the specific atmospheric conditions between the terminals, depending rather on laboratory determinations of dispersion constants and direct measurements of apparent range and range differences.

The dual-frequency technique can be extended to account for the wet component of the troposphere by means of a third, radio-frequency, link. The approach is completely straightforward and is discussed at length by Thayer (1967).

The effectiveness of multiple-wavelength systems in reducing tropospheric range errors will be discussed in detail in Section 4.1.

3.4 Cloud-Cover Constraints

The amount of cloud cover over a proposed ground grid network could place an important restriction on the feasibility of a space-to-ground surveying system. Although, as is intuitively obvious, cloud cover is much more important in the visible spectrum than in the radio, the accuracy and reliability of all types of space-to-ground measurement systems are degraded by cloud cover.

The effect of clouds on the propagation of optical and microwave signals is reasonably well documented (Wilson, 1970). Briefly, for optical transmission, the effect is disastrous; attenuation through even thin clouds or haze is very high, and the loss of resolution due to pulse spreading can reach 100 m for ruby lasers operating at 6943 Å (Bucher et al., 1970).

At microwave frequencies, above approximately 9.0 GHz, the amount of attenuation through rain or rain-bearing clouds is comparable to that encountered in the visible spectrum. At lower radio frequencies, through the VHF and UHF bands, tropospheric attenuation, including the effect of clouds, is negligible. However, cumulus clouds display large gradients of refractive index, which could have a serious influence on the accuracy of radio range or range-rate systems. Unfortunately, the most thorough study of the refractive index of clouds is not well documented (Cunningham, 1964; Crane, 1964), and it is difficult to draw quantitative conclusions regarding the extent of system degradation.

Cloud-cover statistics tend to be very subjective and difficult to interpret. In the following, cloud statistics are tabulated in detail for two geographic areas that are potential candidates for the installation of Clogeos-type systems. Although it is difficult to draw generalities on so subjective a matter, we feel that those areas exhibiting a persistent pattern of heavy cloud cover should not be considered suitable for Clogeos systems operating in the visible spectrum. Moreover, further study would be necessary to determine whether radio systems could operate with satisfactory accuracy under this type of cloud cover. Conversely, areas with very little cloud obscuration might make good candidates for both optical and radio space-to-ground surveying systems.

Statistics from various sources are available for analysis, but most of them are too detailed for an overview. For the most part, those we use herein were obtained from the U.S. Air Force Air Weather Service and from a study of worldwide cloud-cover distributions made in 1967 for NASA by Allied Research Associates (Sherr et al., 1968). In this latter work, the globe was sectioned into 29 regions of climatological similarity determined from existing data. Table 3-10 gives a description of the climates and some general cloud-cover statistics for each.

Most of California and western Nevada (region 18) have a Mediterranean-type climate, with extreme seasonal changes in mean monthly cloud amounts that vary from about 30% cloud cover in summer to 60% during the winter months. The diurnal variations are small, with no particular time of maximum occurrence. Southern Alaska and the Aleutian chain (region 14) fall within the influence of the well-known Aleutian low, a semipermanent low-pressure regime. Here, cloudy skies predominate, varying from a monthly low of about 70% in winter to greater than 80% in summer. As in the case of California and Nevada, there is little diurnal variation.

Figures 3-14 and 3-15 show the seasonal cloud-cover distributions for regions 18 and 14 in graphical form. By looking at the San Francisco and Los Angeles curves, a better understanding of the California cloud-cover climatology can be obtained. During the summer months, a diurnal cycle appears in the San Francisco statistics owing to coastal strati, which form at night and typically burn off as daytime insolation takes effect. For all practical purposes, it appears that Los Angeles and San Francisco have mostly clear to 30% cloud cover 60 to 80% of the time in the summer, except for the early morning San Francisco strati. In winter, this is reduced to 30 to 40% with an equal chance of overcast conditions. The situation for southern Alaska and the Aleutians is quite different. Figure 3-15 indicates that the probability of overcast skies ranges from 60% in the winter to 85% in the summer.

A detailed breakdown of California cloud-cover statistics is reproduced in Tables 3-11 through 3-15. These statistics, from the Air Weather Service,

Table 3-10. General description of climatological regions (from Sherr et al., 1968).

1	2	3	4	5	6	7	8	9
Region Number	General Description	Location	Seasonal Change in Cloud Amount	Mean Monthly Cloud Amount Jun-Aug (in Percent)	Mean Monthly Cloud Amount Dec-Mar (in Percent)	Predominant Cloud Type	Diurnal Variation in Cloud Amount	Hour of Maximum Cloud Amount (Local Time)
01	Essentially Clear	Major Desert Area	Small	< 20	< 20	--	Small	----
02	Little Cloudiness	Sub-Desert Areas	Small	<40	< 40	--	Small	----
03	Tropical Cloudy	Near Equator	Small	>60	> 60	Convective	Large	1600
04	Tropical Moderate Cloudiness	North or South of Region 03	Small	~50	~ 50	Convective	Large	1600
05	Desert Marine	Over Ocean - off West Coasts	Small	~50	~ 50	Stratiform	Large	0800
06	Desert Marine Cloudy Winter	Over Ocean - West of Peru	Extreme	>70	< 30	Stratiform	Large	0800
07	Desert Marine Cloudy Summer	Over Ocean - West of Baja California	Extreme	>70	< 30	Stratiform	Large	0800
08	Mid Latitude - Clear Summer	North America	Extreme	<40	~70	Synoptic Scale	Small	----
09	High Latitude - Cloudy Summer	North America, Asia	Moderate	~70	~ 50	Synoptic Scale	Small	----
10	High Latitude - Clear Winter	Asia, North America	Extreme	~70	<30	Synoptic Scale	Small	----
11	Mid Latitude - Land	Northern Hemisphere	Moderate	~50	~70	Synoptic Scale	Small	----
12	Tropical - Cloudy Summer	North of Region 03	Moderate	>60	~50	Convective	Large	1600
13	Mid Latitude - Ocean	Northern Hemisphere	Moderate	~60	>70	Synoptic Scale	Small	----

Table 3-10. (Cont.)

1	2	3	4	5	6	7	8	9
14	High Latitude - Ocean	Northern Hemisphere	Moderate	>80	~70	Synoptic Scale	Small	----
15	Polar	Northern Hemisphere	Small	~60	~60	Synoptic Scale	Small	----
16	Tropical - Seasonal Change	North of Region 03	Extreme	>70	<40	Convective	Large	1600
17	Tropical - Clear Winter	Northern Hemisphere Near Region 16	Moderate	~50	<30	Convective	Large	1600
18	Mediter-ranean	Northern Hemisphere Europe, Western North America	Extreme	~30 --	-- ~60	Convective Synoptic Scale	Small Small	---- ----
19	Sub Tropical	Northern Hemisphere ~30N	Moderate	<50 --	-- ~60	Convective Synoptic Scale	Large Small	1600 ----
20	Sub Tropical - Ocean	Northern Hemisphere ~30N	Moderate	~50 --	-- >60	Convective Synoptic Scale	Small Small	---- ----
21	Tropical - Cloudy Summer	South of Region 03	Moderate	~50	>60	Convective	Large	1600
22	Mid Latitude Ocean	Southern Hemisphere	Moderate	>70	~60	Synoptic Scale	Small	----
23	High Latitude - Ocean	Southern Hemisphere	Moderate	~70	>80	Synoptic Scale	Small	----
24	Polar	Southern Hemisphere	Small	~60	~60	Synoptic Scale	Small	----
25	Tropical - Seasonal Change	South of Region 03	Extreme	<40	>70	Convective	Large	1600
26	Tropical - Clear Winter	South of Region 25; Africa, Australia	Moderate	<30	~50	Convective	Large	1600
27	Mediter-ranean	Southern Hemisphere Australia, Chile	Extreme	-- ~60	~30 --	Convective Synoptic Scale	Small Small	---- ----
28	Sub Tropical Land	Southern Hemisphere ~30S	Moderate	-- ~60	<50 --	Convective Synoptic Scale	Large Small	1600 ----
29	Sub Tropical - Ocean	Southern ~30S	Moderate	-- >60	~50 --	Convective Synoptic Scale	Small Small	---- ----

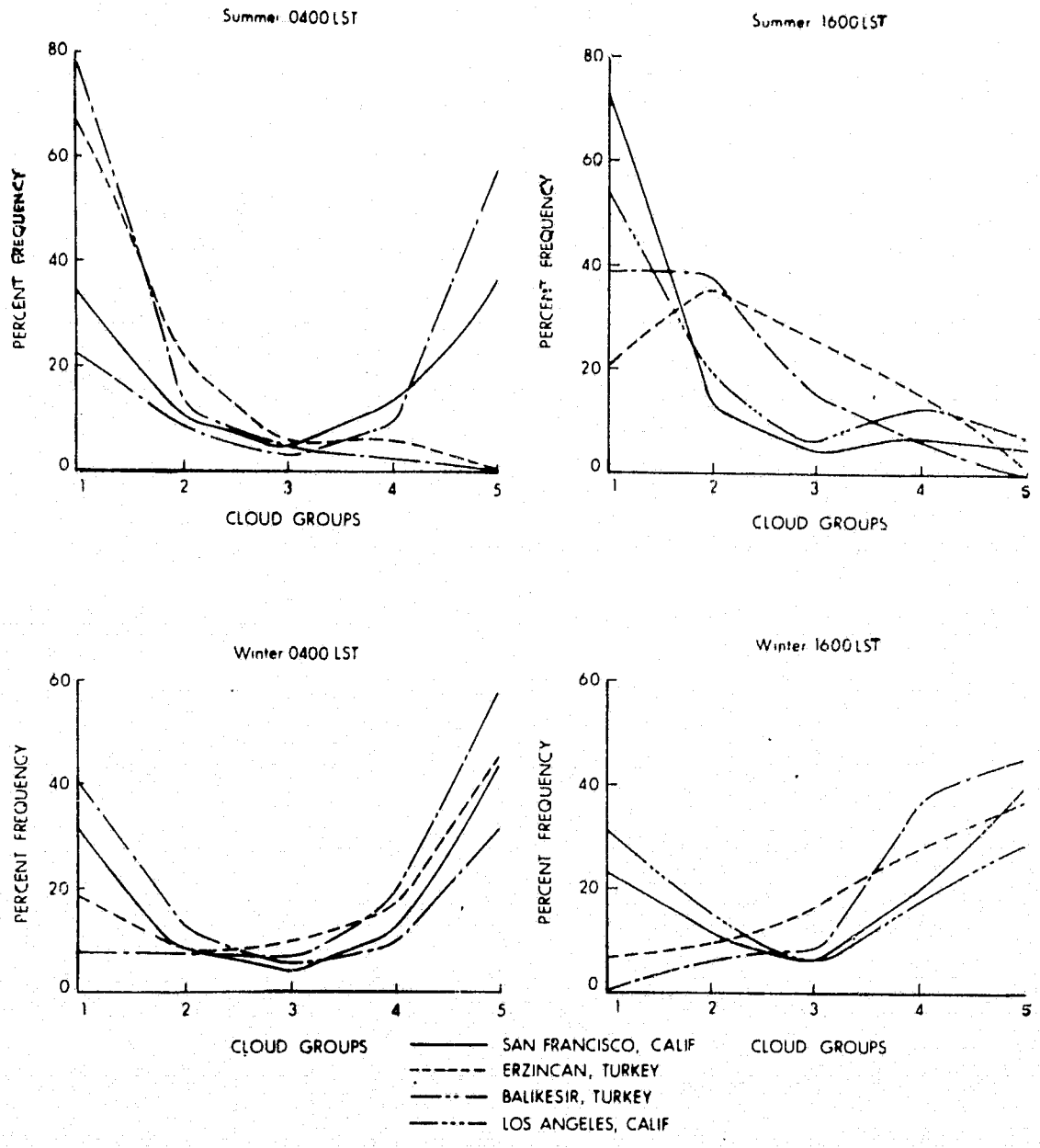

Figure 3-14. Cloud-cover distributions for Region 18 (from Sherr et al., 1968).

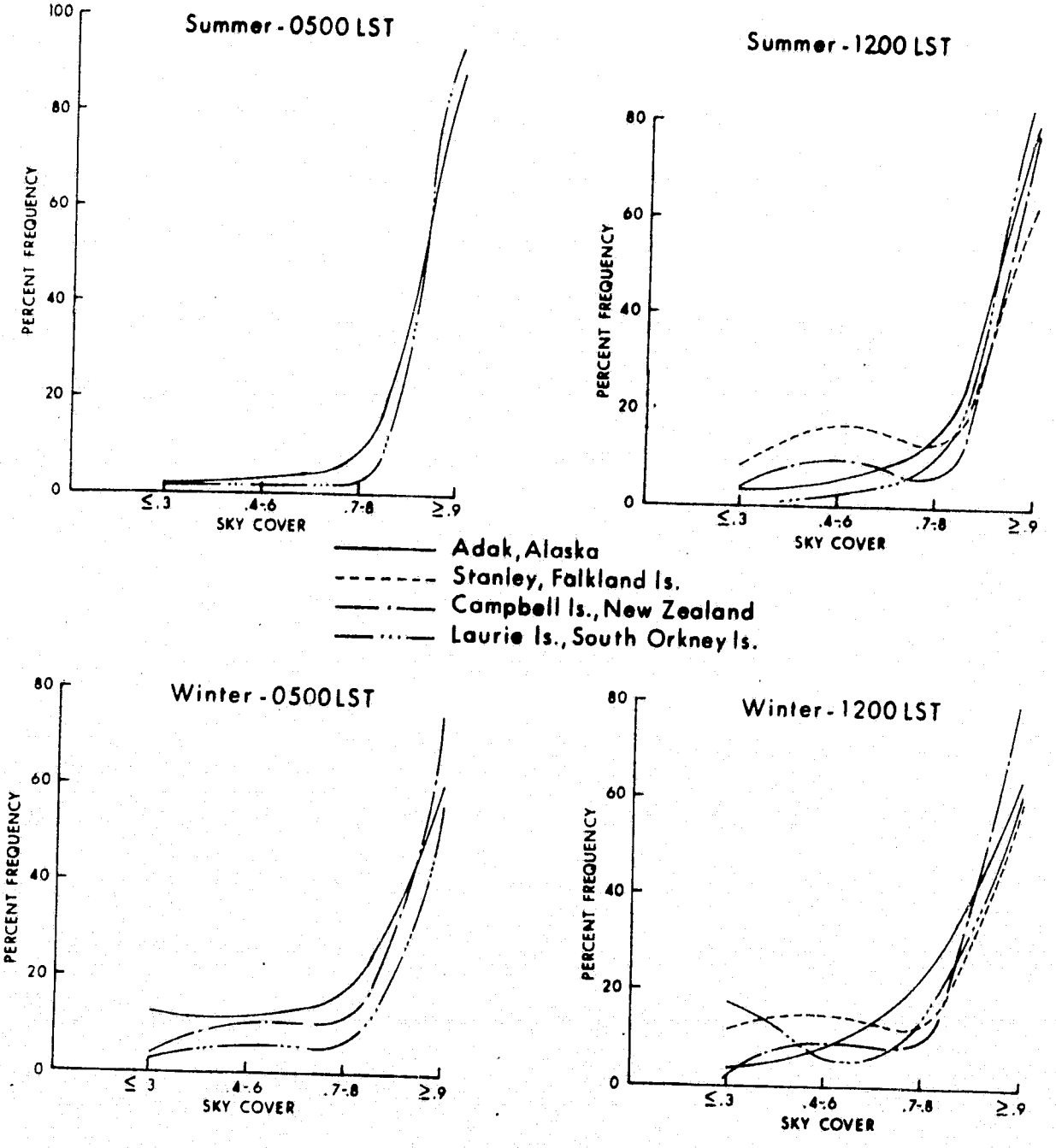

Figure 3-15. Cloud-cover distributions for regions 14 (and 23) (from Sherr at al., 1968).

include fairly large data samples. The data for each station are organized by month according to the average daily proportion of sky covered (in tenths). Following each monthly breakdown is an hourly breakdown for each of the months of January and July. The stations from which the observations were made are Vandenberg Air Force Base (AFB) (on the coast near Santa Barbara), Edwards AFB (in the desert east of Los Angeles), Norton AFB (San Bernardino, east of Los Angeles, west of the Sierra Nevadas), Long Beach Municipal Airport (near Los Angeles), and Hamilton AFB (north of San Francisco on the bay); data are also supplied for Elmendorf AFB in Anchorage, Alaska.

The data for the Santa Barbara area (Table 3-11) are within the limits of the data for region 18 shown in Figure 3-14. From both the figure and the table, the winter statistics agree well, revealing an average of about 30% overcast and 30% clear; those for summer predict a fairly high occurrence of overcast conditions (50 to 55%), with only a 15 to 20% chance of completely clear skies. More specifically, the winter quarter from January to March shows about a 45% probability for the sky to be 70 to 100% obscured and a 24 to 29% chance of being clear. From July to September, there is about a 60% probability of 70 to 100% cloud cover (44 to 56% chance of overcast) and a 30% probability of clear to 30% cloud cover (16 to 28% chance of clear skies). The spring and fall months show the transitions from summer to winter and vice versa. The hourly breakdown for January indicates no diurnal variation; however, for July, most of the cloud cover tends to occur between 1800 and 1100 local solar time (LST), giving 5 daylight hours wherein the sky has a 30 to 46% chance of being 70% obscured to overcast (12 to 23% probability of overcast) and a 40 to 55% chance of being clear to 30% obscured (20 to 26% probability of clear skies).

For the desert area east of the Sierra Nevada mountains, clear skies predominate. Table 3-12 indicates an average of about 14% probability of 70% obscured to overcast conditions during the months of May to October and a 55 to 75% chance of absolutely clear skies (80% or better chance of 30% obscured to clear). These conditions are about the best for the entire state. Little diurnal variation is seen in the accompanying monthly breakdowns for this area, with the highest probability of clear skies being at night (perhaps because of the difficulty of detecting high thin cirrus layers at night).

Table 3-11a. Percentage frequency of occurrence of cloud cover for Vandenberg AFB (from hourly observations), by month.

93214 (STATION) VANDENBERG AFB CALIFORNIA (STATION NAME) 51-53,56-70 (PERIOD) ALL (MONTH)

PERCENTAGE FREQUENCY OF OCCURRENCE
(FROM HOURLY OBSERVATIONS)

MONTH	HOURS (L.S.T.)	PERCENTAGE FREQUENCY OF TENTHS OF TOTAL SKY COVER											MEAN TENTHS OF SKY COVER	TOTAL NO. OF OBS.
		0	1	2	3	4	5	6	7	8	9	10		
JAN	ALL	29.3	6.3	5.5	4.1	3.6	2.6	3.2	4.4	6.2	5.7	29.1	5.0	9225
FEB		27.4	6.6	4.9	4.6	3.6	2.8	4.1	4.2	5.5	5.0	31.1	5.1	8389
MAR		24.3	7.2	6.4	5.1	4.2	3.2	3.2	4.1	5.4	4.8	32.3	5.3	9192
APR		27.7	6.8	5.5	4.4	4.3	3.0	3.3	3.7	5.1	4.3	32.0	5.1	8907
MAY		21.8	6.2	5.2	4.2	2.9	2.6	3.2	3.4	4.5	4.7	41.3	5.9	9203
JUN		20.6	4.9	3.7	3.4	2.7	2.4	2.7	2.8	3.9	3.9	49.1	6.4	9582
JUL		15.7	3.7	3.7	3.5	2.9	2.1	2.4	2.6	3.3	4.1	56.0	7.0	10227
AUG		17.4	4.1	4.2	3.3	2.8	2.4	2.2	3.0	3.8	3.6	53.3	6.7	10245
SEP		28.2	4.6	3.8	3.0	2.5	1.7	2.5	2.4	3.7	3.6	44.2	5.8	9922
OCT		34.9	5.5	4.3	4.0	3.0	1.9	2.6	3.4	3.9	4.2	32.5	4.8	10219
NOV		30.8	6.6	5.9	4.3	3.2	2.6	3.5	5.3	6.1	5.1	26.8	4.8	9892
DEC		24.2	6.9	5.9	5.0	3.8	2.7	3.8	4.8	5.4	4.8	22.9	4.3	10236
TOTALS		26.0	5.8	4.9	4.1	3.3	2.5	3.1	3.7	4.7	4.5	37.6	5.5	115239

Table 3-11b. Percentage frequency of occurrence of cloud cover for Vandenberg AFB (from hourly observations) for January.

93214 (STATION) VANDENBERG AFB CALIFORNIA (STATION NAME) 52-53,59-70 (PERIOD) JAN (MONTH)

PERCENTAGE FREQUENCY OF OCCURRENCE
(FROM HOURLY OBSERVATIONS)

MONTH	HOURS (L.S.T.)	PERCENTAGE FREQUENCY OF TENTHS OF TOTAL SKY COVER											MEAN TENTHS OF SKY COVER	TOTAL NO. OF OBS.
		0	1	2	3	4	5	6	7	8	9	10		
JAN	00-02	37.2	5.3	4.9	4.0	3.7	2.3	3.7	3.3	4.8	3.4	27.2	4.4	1112
	03-05	40.6	4.3	3.2	4.8	3.0	2.6	2.7	3.0	4.6	3.8	27.4	4.3	1116
	06-08	29.9	5.6	5.6	3.6	3.6	2.3	3.0	4.7	7.1	6.7	28.0	5.0	1152
	09-11	24.3	6.8	5.5	3.8	3.3	2.9	3.2	6.5	6.7	7.8	29.2	5.4	1210
	12-14	20.7	8.0	6.9	4.7	3.9	3.5	3.4	5.3	7.3	7.5	28.8	5.4	1217
	15-17	20.1	6.1	6.4	4.6	4.2	2.5	2.6	4.2	7.5	8.4	31.4	5.6	1100
	18-20	26.2	7.5	5.8	4.1	3.8	2.6	3.7	5.1	6.3	3.8	31.2	5.1	1116
	21-23	35.1	4.5	5.8	3.2	3.5	2.3	2.9	3.3	5.6	3.9	29.8	4.7	1114
TOTALS		29.3	6.3	5.5	4.1	3.6	2.6	3.2	4.4	6.2	5.7	29.1	5.0	9225

Table 3-11c. Percentage frequency of occurrence of cloud cover for Vandenberg AFB (from hourly observations) for July.

93214 (STATION) VANDENBERG AFB CALIFORNIA (STATION NAME) 51-52,58-70 (PERIOD) JUL (MONTH)

PERCENTAGE FREQUENCY OF OCCURRENCE
(FROM HOURLY OBSERVATIONS)

MONTH	HOURS (L.S.T.)	PERCENTAGE FREQUENCY OF TENTHS OF TOTAL SKY COVER											MEAN TENTHS OF SKY COVER	TOTAL NO. OF OBS.
		0	1	2	3	4	5	6	7	8	9	10		
JUL	00-02	12.4	1.2	1.6	1.7	1.2	.6	.6	.9	.9	1.6	77.3	8.2	1209
	03-05	7.9	.9	.9	1.0	1.1	.5	.5	1.2	.5	1.8	83.7	8.8	1209
	06-08	6.6	1.0	1.4	1.8	1.5	.7	.8	.7	1.8	2.9	80.8	8.8	1356
	09-11	20.6	5.5	4.3	4.5	4.2	2.9	3.0	4.2	5.1	4.8	40.9	6.0	1385
	12-14	26.1	8.7	10.1	8.5	6.6	5.6	5.4	4.6	6.2	6.5	11.6	4.0	1382
	15-17	19.9	7.3	6.5	6.3	4.8	3.7	5.8	6.7	8.0	8.3	22.6	5.2	1268
	18-20	15.6	3.3	2.2	2.3	2.2	2.1	2.2	1.4	3.1	6.0	59.7	7.3	1209
	21-23	16.3	1.7	2.2	1.6	1.3	1.0	1.1	1.4	1.1	1.2	71.1	7.7	1209
TOTALS		15.7	3.7	3.7	3.5	2.9	2.1	2.4	2.6	3.3	4.1	56.0	7.0	10227

Table 3-12a. Percentage frequency of occurrence of cloud cover for Edwards AFB (from hourly observations), by month.

23114	EDWARDS AFB CALIFORNIA	62-72	ALL
STATION	STATION NAME	PERIOD	MONTH

PERCENTAGE FREQUENCY OF OCCURRENCE
(FROM HOURLY OBSERVATIONS)

MONTH	HOURS (L.S.T.)	PERCENTAGE FREQUENCY OF TENTHS OF TOTAL SKY COVER											MEAN TENTHS OF SKY COVER	TOTAL NO. OF OBS.
		0	1	2	3	4	5	6	7	8	9	10		
JAN	ALL	40.3	3.9	4.0	8.1	3.2	2.7	2.9	3.6	4.1	4.8	22.5	4.1	7265
FEB		40.2	4.3	4.4	8.7	3.0	2.2	2.9	3.0	3.6	6.0	21.7	4.0	6649
MAR		43.4	5.1	5.0	8.0	3.4	2.8	2.7	3.8	3.2	5.4	17.2	3.6	7353
APR		49.4	5.2	5.1	7.5	3.2	2.5	2.6	3.0	3.7	4.8	13.2	3.0	7056
MAY		55.9	4.9	4.8	8.6	2.9	2.1	2.5	2.7	3.1	4.3	8.3	2.4	7324
JUN		71.1	4.3	3.6	4.6	2.5	1.5	1.5	1.8	2.4	2.5	4.5	1.5	6822
JUL		62.4	4.4	4.8	7.5	2.8	2.1	1.9	2.5	2.9	3.1	5.6	2.0	7291
AUG		67.7	4.5	4.5	6.5	2.6	2.0	2.4	2.1	2.4	2.5	2.9	1.6	7419
SEP		75.9	3.3	3.0	4.0	1.8	1.4	1.4	1.8	1.7	1.2	4.6	1.3	7175
OCT		63.7	4.4	4.1	5.0	2.3	2.0	2.6	2.7	3.8	3.0	6.5	2.0	7386
NOV		40.1	4.5	5.0	7.1	4.0	2.9	3.1	3.6	4.9	4.9	20.1	3.9	7158
DEC		42.2	6.1	5.5	6.7	3.3	2.8	2.7	3.5	4.2	4.6	18.4	3.6	7340
TOTALS		54.4	4.6	4.5	6.9	2.9	2.3	2.4	2.8	3.3	3.9	12.1	2.8	86234

Table 3-12b. Percentage frequency of occurrence of cloud cover for Edwards AFB (from hourly observations), for January.

23114	EDWARDS AFB CALIFORNIA	63-72	JAN
STATION	STATION NAME	PERIOD	MONTH

PERCENTAGE FREQUENCY OF OCCURRENCE
(FROM HOURLY OBSERVATIONS)

MONTH	HOURS (L.S.T.)	PERCENTAGE FREQUENCY OF TENTHS OF TOTAL SKY COVER											MEAN TENTHS OF SKY COVER	TOTAL NO. OF OBS.
		0	1	2	3	4	5	6	7	8	9	10		
JAN	00-02	52.5	2.9	4.3	7.8	3.5	2.9	1.8	3.7	1.4	1.3	17.8	3.0	908
	03-05	53.8	3.5	3.1	6.8	3.2	2.0	2.4	2.9	2.8	2.2	17.4	3.0	916
	06-08	40.5	3.4	4.2	6.7	3.5	3.1	3.4	3.4	4.8	5.5	21.6	4.1	915
	09-11	30.9	4.7	4.1	8.7	3.0	2.6	1.8	3.4	5.3	6.9	28.6	4.9	907
	12-14	28.5	5.1	3.8	7.8	3.5	3.2	3.6	4.4	5.5	6.5	28.0	5.0	905
	15-17	29.2	4.5	4.4	9.3	2.5	2.7	2.5	4.3	4.3	7.2	28.9	5.0	902
	18-20	39.5	4.0	3.4	8.8	2.9	2.9	4.5	3.0	4.6	5.4	21.0	4.1	906
	21-23	47.1	2.8	4.5	9.1	3.4	2.4	3.5	3.3	4.1	3.1	16.7	3.4	906
TOTALS		40.3	3.9	4.0	8.1	3.2	2.7	2.9	3.6	4.1	4.8	22.5	4.1	7265

Table 3-12c. Percentage frequency of occurrence of cloud cover for Edwards AFB (from hourly observations), for July.

23114	EDWARDS AFB CALIFORNIA	63-72	JUL
STATION	STATION NAME	PERIOD	MONTH

PERCENTAGE FREQUENCY OF OCCURRENCE
(FROM HOURLY OBSERVATIONS)

MONTH	HOURS (L.S.T.)	PERCENTAGE FREQUENCY OF TENTHS OF TOTAL SKY COVER											MEAN TENTHS OF SKY COVER	TOTAL NO. OF OBS.
		0	1	2	3	4	5	6	7	8	9	10		
JUL	00-02	77.4	2.8	4.5	4.4	1.4	.9	1.1	.8	1.1	1.3	4.4	1.1	915
	03-05	68.5	4.8	4.3	5.6	2.9	1.3	1.4	1.9	1.2	3.2	4.9	1.6	910
	06-08	58.3	5.6	4.1	6.4	2.9	2.5	2.1	3.0	3.4	3.8	7.9	2.3	904
	09-11	59.3	4.3	4.5	7.8	3.1	2.0	2.5	2.0	4.5	3.0	6.9	2.2	907
	12-14	53.2	4.4	4.0	9.9	4.3	4.5	2.0	3.9	4.6	3.8	5.5	2.5	917
	15-17	52.4	4.2	5.4	9.8	3.5	2.5	3.2	4.3	3.7	4.3	6.7	2.6	910
	18-20	57.0	6.0	6.7	9.0	3.0	1.8	1.4	2.6	2.2	4.7	5.6	2.1	912
	21-23	72.7	2.9	4.5	7.2	1.6	1.6	1.4	1.6	2.2	1.0	3.2	1.3	916
TOTALS		62.4	4.4	4.8	7.5	2.8	2.1	1.9	2.5	2.9	3.1	5.6	2.0	7291

The Air Force data for the Los Angeles area, Tables 3-13 and 3-14, indicate a wide variability in cloud cover over a relatively small geographical area. For all months of the year, Long Beach appears to be completely clear 30 to 40% of the time (clear to 30% obscured 50 to 60% of the time) and overcast 25 to 35% of the time. Norton AFB shows a slightly higher occurrence of clear skies (30 to 50%) and an almost total lack of overcast conditions from July to September. Table 3-13 indicates that the skies are clear to 30% obscured about 45% of the time in the winter and 75% in summer. The diurnal variations are low for San Bernardino in the winter but are considerable for Long Beach, which experiences clearest skies between 1900 and 0700 LST and heaviest overcast between midnight and 1100 LST. Summertime diurnal variations are similar for both locations; overcast occurs mainly in the early morning hours, and clear skies are most frequent from noon to midnight.

The statistics for the San Francisco area show strong seasonal and diurnal variations (Table 3-15). On the average, the data correspond well with those in Figure 3-14, showing a high probability of clear skies in the summer and more frequent overcast conditions in the winter. In the summer, the skies have roughly a 70% chance of being 30% obscure to clear and a 20% chance of being 70% obscure to overcast; in the winter, these numbers are 40 and 50%. The winter months are typified by clear skies occurring most often from 1800 to 0500 LST, and the summer months, by clear skies from 0900 to midnight. Overcast skies follow marked diurnal cycles during the winter.

Table 3-16 contains data for Elmendorf AFB in Anchorage, Alaska. For the entire year, the data reveal 70% obscure to overcast skies 60 to 75% of the time. Clear days occur 10 to 20% of the time over a large part of the year, excluding the warm months. Little in the way of diurnal variations in cloud cover can be gleaned from the hourly data in Table 3-16, substantiating that southern Alaska and the Aleutian Islands comprise a very cloudy region indeed.

The gross features of the cloud-cover statistics for California and southern Alaska are summarized in Table 3-17. For this summary, we averaged data from Tables 3-11 through 3-16 on a seasonal basis for several general categories varying from clear skies to conditions of complete overcast. The months

Table 3-13a. Percentage frequency of occurrence of cloud cover for Norton AFB (from hourly observations), by month.

MONTH	HOURS (L.S.T.)	PERCENTAGE FREQUENCY OF TENTHS OF TOTAL SKY COVER											MEAN TENTHS OF SKY COVER	TOTAL NO. OF OBS.
		0	1	2	3	4	5	6	7	8	9	10		
JAN	ALL	33.7	4.7	4.7	5.3	3.9	2.8	4.0	4.7	6.2	4.4	25.7	4.6	19755
FEB		33.1	4.0	4.6	5.1	3.8	3.0	3.6	4.0	5.7	4.3	28.8	4.8	18012
MAR		27.9	4.5	5.0	5.4	4.1	3.2	3.6	4.5	6.6	4.6	30.6	5.2	19734
APR		28.8	4.6	5.2	5.1	4.6	3.3	3.3	4.1	5.9	4.3	30.9	5.1	18597
MAY		29.9	6.8	5.8	5.8	4.2	3.0	3.1	3.3	4.7	3.5	29.9	4.8	19894
JUN		41.5	9.4	8.2	5.6	3.3	2.4	1.4	2.2	2.5	1.6	21.9	3.4	18960
JUL		49.7	9.9	8.0	7.6	4.4	3.0	2.4	3.2	3.2	2.0	6.7	2.3	19618
AUG		47.5	10.8	9.6	8.2	4.6	3.1	2.3	2.6	2.7	1.9	6.8	2.3	19991
SEP		46.9	9.0	8.7	6.9	4.3	2.5	2.4	2.1	2.5	1.5	11.4	2.5	18670
OCT		41.5	7.5	7.0	6.9	4.4	3.0	2.7	3.3	3.9	3.2	16.7	3.4	19944
NOV		41.1	5.7	5.6	5.8	3.7	2.9	3.1	3.8	4.4	4.6	19.3	3.8	19255
DEC		37.4	5.5	5.8	5.9	3.6	2.6	3.3	3.9	5.6	4.4	22.0	4.1	19966
TOTALS		38.4	6.9	6.5	6.1	4.1	2.9	2.9	3.5	4.5	3.4	20.9	3.9	232396

Table 3-13b. Percentage frequency of occurrence of cloud cover for Norton AFB (from hourly observations), for January.

23122 (STATION) NORTON AFB CALIF/SAN BERNARDINO (STATION NAME) 46-72 (PERIOD) JA (MONTH)

PERCENTAGE FREQUENCY OF OCCURRENCE
(FROM HOURLY OBSERVATIONS)

MONTH	HOURS (L.S.T.)	PERCENTAGE FREQUENCY OF TENTHS OF TOTAL SKY COVER											MEAN TENTHS OF SKY COVER	TOTAL NO. OF OBS.
		0	1	2	3	4	5	6	7	8	9	10		
JAN	00-02	41.0	4.0	4.4	4.5	3.4	2.0	3.7	3.6	4.5	2.9	26.1	4.2	2462
	03-05	42.5	3.7	3.9	4.1	3.8	2.2	3.4	4.6	3.5	2.2	26.2	4.1	2464
	06-08	29.2	6.4	4.6	5.6	3.4	3.7	3.8	4.9	7.1	4.8	26.5	4.9	2479
	09-11	26.7	5.4	4.7	5.6	4.0	3.3	4.4	5.0	7.3	6.3	25.4	4.8	2481
	12-14	27.5	5.6	4.9	5.1	4.2	2.9	5.1	4.8	8.3	5.9	25.7	5.0	2475
	15-17	27.1	5.2	5.0	6.3	3.8	2.9	4.0	5.7	7.4	6.1	26.4	5.1	2475
	18-20	34.6	3.8	5.4	5.8	4.6	3.0	3.9	4.5	6.7	3.7	24.0	4.5	2463
	21-23	29.1	3.6	4.7	5.2	4.2	2.6	3.7	4.2	4.5	2.9	25.2	4.2	2456
TOTALS		33.7	4.7	4.7	5.3	3.9	2.8	4.0	4.7	6.2	4.4	25.7	4.6	19755

Table 3-13c. Percentage frequency of occurrence of cloud cover for Norton AFB (from hourly observations), for July.

23122	NORTON AFB CALIF/SAN BERNARDINO	46-72	JUL
STATION	STATION NAME	PERIOD	MONTH

PERCENTAGE FREQUENCY OF OCCURRENCE
(FROM HOURLY OBSERVATIONS)

MONTH	HOURS (L.S.T.)	PERCENTAGE FREQUENCY OF TENTHS OF TOTAL SKY COVER											MEAN TENTHS OF SKY COVER	TOTAL NO. OF OBS.
		0	1	2	3	4	5	6	7	8	9	10		
JUL	00-02	64.2	6.5	5.9	5.4	3.5	1.8	1.9	2.0	2.1	.8	5.9	1.7	2463
	03-05	49.4	9.0	7.0	7.1	3.7	3.3	1.9	2.7	2.5	1.4	12.0	2.6	2445
	06-08	24.2	11.5	9.9	9.0	4.8	3.3	2.5	3.2	3.4	3.2	14.9	3.4	2435
	09-11	36.4	14.1	11.4	10.4	5.7	3.8	2.3	3.8	3.9	2.5	5.5	2.6	2434
	12-14	44.7	12.3	8.4	8.2	5.0	2.7	2.6	4.2	4.6	3.1	4.2	2.4	2457
	15-17	48.7	10.1	8.3	7.0	4.5	3.2	2.8	4.3	3.9	2.3	4.4	2.3	2457
	18-20	53.5	9.7	7.2	6.0	4.3	3.2	2.8	2.9	3.7	1.4	3.5	1.9	2462
	21-23	66.8	6.2	5.6	5.3	3.3	2.4	2.3	2.4	1.8	.7	3.3	1.4	2465
TOTALS		49.7	9.9	8.0	7.6	4.4	3.0	2.4	3.2	3.2	2.0	6.7	2.3	19618

Table 3-14a. Percentage frequency of occurrence of cloud cover for Long Beach (from hourly observations), by month.

PERCENTAGE FREQUENCY OF OCCURRENCE

23129 LONG BEACH CALIFORNIA MUN AIRPORT ALL

STATION STATION NAME MONTH

YEARS

MONTH	HOUR (L.S.T.)	FREQUENCY OF TENTHS OF TOTAL SKY COVER BY GROUPS							MEAN TENTHS OF SKY COVER	SUM OF TENTHS OF SKY COVER	TOTAL NO. OF OBSERVATIONS
		0	1-2	3	4-5	6-7	8-9	10			
01		32.2	8.7	4.5	6.6	8.0	10.6	29.5	4.9	36560	7432
02		38.4	7.8	4.4	6.2	7.4	8.4	27.4	4.5	30257	6792
03		32.9	10.8	5.0	7.1	8.4	10.6	25.1	4.6	34101	7438
04		23.6	8.5	4.8	6.8	7.4	11.6	37.3	5.8	41484	7198
05		32.9	8.4	4.4	6.9	6.4	8.2	32.8	5.0	36903	7439
06		35.1	10.0	4.7	5.2	4.4	5.4	35.2	4.8	34441	7196
07		39.3	11.7	5.0	7.0	4.7	5.9	26.4	4.1	30389	7438
08		40.0	12.6	4.3	5.3	4.4	6.1	27.2	4.1	30309	7440
09		44.6	9.6	3.8	5.2	4.5	4.9	27.4	3.9	28324	7198
10		37.6	8.6	4.3	6.0	6.8	7.1	29.6	4.5	33620	7437
11		44.8	8.8	4.8	5.8	6.0	7.1	22.7	3.8	27307	7199
12		37.7	9.5	5.0	6.4	6.6	9.9	25.0	4.3	32296	7439
TOTALS		36.6	9.6	4.6	6.2	6.2	8.0	28.8	4.5	395091	87646

Table 3-14b. Percentage frequency of occurrence of cloud cover for Long Beach (from hourly observations), for January.

FREQUENCY OF OCCURRENCE

23129 LONG BEACH CALIFORNIA MUN AIRPORT JAN
STATION STATION NAME MONTH

48 49 50 51 52 53 54 55 56 57
YEARS

MONTH	HOUR (L.S.T.)	FREQUENCY OF TENTHS OF TOTAL SKY COVER BY GROUPS							MEAN TENTHS OF SKY COVER	SUM OF TENTHS OF SKY COVER	TOTAL NO OF OBSERVATIONS
		0	1-2	3	4-5	6-7	8-9	10			
	01	122	22	11	16	14	20	104	4.7	1440	309
	02	124	18	13	10	23	12	110	4.7	1464	310
	03	127	13	9	11	15	23	112	4.9	1505	310
	04	121	23	11	6	14	21	114	4.8	1496	310
	05	119	27	7	8	17	19	113	4.8	1499	310
	06	122	16	10	17	15	26	104	4.8	1483	310
	07	91	22	17	23	25	21	111	5.3	1638	310
	08	77	27	7	27	27	42	103	5.7	1753	310
	09	73	31	14	15	24	51	102	5.7	1766	310
	10	80	30	11	22	25	46	95	5.4	1676	309
	11	80	32	14	22	30	31	101	5.3	1655	310
	12	77	39	15	18	26	38	97	5.3	1648	310
	13	81	28	22	16	32	47	84	5.3	1631	310
	14	79	32	12	20	35	56	76	5.3	1639	310
	15	77	37	15	21	38	49	72	5.1	1584	309
	16	76	44	11	26	32	54	67	5.0	1546	310
	17	77	35	18	32	35	45	68	5.0	1546	310
	18	74	33	18	27	42	47	69	5.1	1582	310
	19	105	29	17	26	37	25	71	4.4	1374	310
	20	117	20	19	26	21	24	78	4.3	1317	305
	21	125	17	21	24	21	22	80	4.2	1317	310
	22	123	24	15	27	16	25	80	4.2	1310	310
	23	126	23	15	22	17	22	85	4.2	1317	310
	24	123	21	13	26	15	19	93	4.4	1374	310
TOTALS		2396	643	335	488	596	785	2189	4.9	36560	7432

Table 3-14c. Percentage frequency of occurrence of cloud cover for Long Beach (from hourly observations), for July.

FREQUENCY OF OCCURRENCE

23129 (STATION) LONG BEACH CALIFORNIA MUN AIRPORT (STATION NAME) JUL (MONTH)

48 49 50 51 52 53 54 55 56 57 (YEARS)

MONTH	HOUR (L.S.T.)	FREQUENCY OF TENTHS OF TOTAL SKY COVER BY GROUPS							MEAN TENTHS OF SKY COVER	SUM OF TENTHS OF SKY COVER	TOTAL NO. OF OBSERVATIONS
		0	1-2	3	4-5	6-7	8-9	10			
	01	116	10	15	20	11	16	122	5.1	1572	310
	02	101	15	8	13	7	25	141	5.7	1775	310
	03	84	11	5	14	11	20	165	6.4	1985	310
	04	70	8	5	13	15	17	182	6.9	2153	310
	05	55	13	5	16	15	15	191	7.2	2241	310
	06	30	20	9	18	15	24	194	7.7	2384	310
	07	29	17	8	17	18	24	197	7.8	2426	310
	08	29	24	11	18	17	35	176	7.5	2316	310
	09	44	30	16	28	22	32	137	6.5	2004	309
	10	73	39	21	38	18	27	94	5.1	1579	310
	11	103	52	24	33	19	20	59	3.8	1184	310
	12	136	59	21	31	20	9	34	2.7	837	310
	13	166	56	21	26	14	13	14	1.9	600	310
	14	181	54	21	26	10	11	7	1.6	486	310
	15	189	55	21	19	10	13	3	1.4	434	310
	16	192	58	19	16	13	11	1	1.3	405	310
	17	192	51	17	25	9	14	2	1.4	435	310
	18	188	51	25	22	10	11	3	1.4	427	310
	19	174	64	14	24	14	16	4	1.6	508	310
	20	156	54	28	24	13	16	18	2.2	670	309
	21	167	38	17	28	18	16	26	2.4	747	310
	22	160	40	15	18	18	17	42	2.8	869	310
	23	150	32	12	19	18	18	61	3.4	1054	310
	24	138	22	13	13	14	18	92	4.2	1298	310
TOTALS		2923	873	371	519	349	438	1965	4.1	30389	7438

Table 3-15a. Percentage frequency of occurrence of cloud cover for Hamilton AFB, from hourly observations), by month.

23211 HAMILTON AFB CALIF/SAN RAFAEL 46-70 ALL

STATION STATION NAME PERIOD MONTH

PERCENTAGE FREQUENCY OF OCCURRENCE
(FROM HOURLY OBSERVATIONS)

MONTH	HOURS (L.S.T.)	PERCENTAGE FREQUENCY OF TENTHS OF TOTAL SKY COVER											MEAN TENTHS OF SKY COVER	TOTAL NO. OF OBS.
		0	1	2	3	4	5	6	7	8	9	10		
JAN	ALL	24.7	3.8	3.8	3.1	2.9	2.1	2.8	3.6	4.8	4.1	44.5	6.0	18588
FEB		27.0	4.6	4.0	3.7	3.2	2.2	3.2	3.9	5.5	3.7	39.2	5.7	16941
MAR		30.3	5.0	4.9	4.1	3.5	3.1	3.9	4.7	6.5	4.9	29.2	5.0	18586
APR		34.7	5.9	5.4	4.6	3.8	2.8	3.7	4.5	5.7	4.6	25.1	4.5	17993
MAY		39.0	6.5	5.6	4.6	4.0	3.1	3.4	4.0	5.4	3.9	20.5	3.9	18592
JUN		51.1	6.5	5.4	4.1	2.9	2.3	2.5	3.1	3.6	2.8	15.8	3.0	17990
JUL		65.4	5.5	3.9	3.2	2.1	1.5	1.9	2.0	2.2	1.5	10.7	2.0	18594
AUG		59.9	6.2	4.2	3.0	2.3	1.7	2.2	2.2	2.7	2.1	13.4	2.5	18590
SEP		59.7	5.3	4.6	3.3	2.9	1.9	2.4	2.6	3.0	2.1	12.2	2.4	17992
OCT		48.1	5.5	4.4	4.1	2.9	2.1	2.9	3.2	4.1	3.3	19.5	3.5	18595
NOV		32.2	4.9	4.5	3.6	3.1	2.4	3.3	3.6	5.1	4.6	22.7	5.0	17993
DEC		21.7	3.8	4.3	3.4	3.1	2.2	2.7	3.8	4.6	4.0	46.4	6.3	18591
TOTALS		41.2	5.3	4.6	3.7	3.1	2.3	2.9	3.4	4.4	3.4	25.8	4.2	219043

Table 3-15b. Percentage frequency of occurrence of cloud cover for Hamilton AFB (from hourly observations), for January.

23211 HAMILTON AFB CALIF/SAN RAFAEL 46-70 JAN

STATION STATION NAME PERIOD MONTH

PERCENTAGE FREQUENCY OF OCCURRENCE
(FROM HOURLY OBSERVATIONS)

MONTH	HOURS (L.S.T.)	PERCENTAGE FREQUENCY OF TENTHS OF TOTAL SKY COVER											MEAN TENTHS OF SKY COVER	TOTAL NO. OF OBS.
		0	1	2	3	4	5	6	7	8	9	10		
JAN	00-02	32.9	3.1	3.7	3.4	2.7	1.9	2.6	2.3	3.7	2.1	41.6	5.4	2322
	03-05	27.9	2.4	3.6	3.8	2.6	1.4	2.8	2.9	3.4	2.2	47.1	5.9	2325
	06-08	18.5	3.7	2.6	2.8	2.3	2.0	2.7	4.0	4.6	4.6	51.4	6.7	2225
	09-11	17.0	3.7	2.7	2.1	2.7	2.1	2.1	3.3	5.4	5.4	53.6	7.0	2324
	12-14	17.5	4.4	3.4	3.4	2.4	2.3	2.7	5.5	6.2	6.1	46.3	6.6	2323
	15-17	19.0	4.9	4.3	3.0	3.1	3.1	3.5	3.6	6.5	6.5	42.5	6.3	2324
	18-20	29.5	4.6	4.4	3.5	4.0	2.4	2.8	3.8	4.7	3.2	37.1	5.3	2324
	21-23	24.9	3.2	4.3	2.9	3.2	1.8	3.3	3.2	3.9	2.8	36.6	5.1	2321
TOTALS		24.7	3.8	3.8	3.1	2.9	2.1	2.8	3.6	4.8	4.1	44.5	6.0	18586

Table 3-15c. Percentage frequency of occurrence of cloud cover for Hamilton AFB (from hourly observations), for July.

23211 (STATION) HAMILTON AFB CALIF/SAN RAFAEL (STATION NAME) 46-70 (PERIOD) JUL (MONTH)

PERCENTAGE FREQUENCY OF OCCURRENCE
(FROM HOURLY OBSERVATIONS)

MONTH	HOURS (L.S.T.)	PERCENTAGE FREQUENCY OF TENTHS OF TOTAL SKY COVER											MEAN TENTHS OF SKY COVER	TOTAL NO. OF OBS.
		0	1	2	3	4	5	6	7	8	9	10		
JUL	00-02	66.6	3.9	3.6	3.5	2.3	1.6	2.0	1.7	2.5	1.0	11.2	2.0	2325
	03-05	46.1	5.3	3.8	3.4	2.1	1.3	2.3	2.3	3.1	2.5	27.7	3.9	2324
	06-08	36.9	6.4	4.5	4.5	2.4	1.9	2.3	3.0	3.4	3.4	31.3	4.5	2324
	09-11	60.9	8.0	5.7	4.2	3.2	2.1	2.5	3.2	2.3	2.2	5.5	1.9	2325
	12-14	77.5	4.6	3.7	2.2	2.2	1.7	1.7	1.3	1.4	.8	2.6	1.0	2325
	15-17	78.3	5.1	3.4	2.7	1.5	1.3	1.7	1.2	1.5	.9	2.3	.9	2325
	18-20	76.8	6.3	2.9	2.8	1.7	1.2	1.4	2.2	1.7	.8	2.2	1.0	2322
	21-23	79.3	4.0	3.7	2.6	1.7	1.0	1.6	1.2	1.3	.6	2.9	.9	2324
TOTALS		66.4	5.5	3.9	3.2	2.1	1.5	1.9	2.0	2.2	1.5	10.7	2.0	18594

Table 3-16a. Percentage frequency of occurrence of cloud cover for Elmendorf AFB (from hourly observations), by month.

25401	ANCHORAGE ALASKA/ELMENDORF AFB	46-53,56-68	ALL
STATION	STATION NAME	PERIOD	MONTH

PERCENTAGE FREQUENCY OF OCCURRENCE
(FROM HOURLY OBSERVATIONS)

MONTH	HOURS (L.S.T.)	PERCENTAGE FREQUENCY OF TENTHS OF TOTAL SKY COVER											MEAN TENTHS OF SKY COVER	TOTAL NO. OF OBS.
		0	1	2	3	4	5	6	7	8	9	10		
JAN	ALL	21.4	3.8	3.9	3.4	3.0	2.3	3.1	3.9	5.6	5.1	45.1	6.3	14856
FEB		20.0	3.7	3.8	2.9	2.5	1.9	3.0	4.2	6.0	5.5	46.4	6.5	13553
MAR		22.5	4.1	3.8	3.4	2.7	2.1	3.2	3.8	6.0	5.5	42.9	6.2	14878
APR		14.6	4.0	4.1	3.8	3.2	2.6	3.6	4.6	7.1	7.3	45.4	6.8	14830
MAY		8.1	3.3	3.5	3.1	3.1	3.0	3.8	5.2	9.0	9.0	48.9	7.5	15622
JUN		4.0	2.7	3.4	3.5	3.7	3.2	3.7	6.4	9.2	10.4	50.0	7.8	15118
JUL		5.5	3.0	3.4	3.6	3.6	3.2	3.7	4.9	7.6	9.1	52.4	7.7	15618
AUG		5.7	2.8	3.7	3.3	3.3	3.1	3.2	5.0	8.1	8.9	52.8	7.8	15622
SEP		8.0	2.7	2.9	2.9	2.9	2.8	2.9	4.1	7.0	7.7	56.2	7.8	15111
OCT		12.7	3.3	3.4	2.8	2.8	2.8	3.3	4.4	6.5	7.1	51.0	7.2	15381
NOV		18.2	3.6	3.7	3.4	3.1	2.3	2.9	3.9	5.5	5.2	48.4	6.6	13654
DEC		19.4	3.0	3.3	2.8	2.7	2.0	2.8	3.8	5.4	5.0	49.9	6.7	14129
TOTALS		13.3	3.3	3.6	3.2	3.1	2.6	3.3	4.5	6.9	7.2	49.1	7.1	178372

Table 3-16b. Percentage frequency of occurrence of cloud cover for Elmendorf AFB (from hourly observations), for January.

26401 (STATION) ANCHORAGE ALASKA/ELMENDORF AFB (STATION NAME) 46-53, 57-68 (PERIOD) JAN (MONTH)

PERCENTAGE FREQUENCY OF OCCURRENCE
(FROM HOURLY OBSERVATIONS)

MONTH	HOURS (L.S.T.)	PERCENTAGE FREQUENCY OF TENTHS OF TOTAL SKY COVER											MEAN TENTHS OF SKY COVER	TOTAL NO. OF OBS.
		0	1	2	3	4	5	6	7	8	9	10		
JAN	00-02	25.7	2.7	3.0	2.6	2.2	2.3	3.0	3.8	5.5	3.7	45.4	6.1	1857
	03-05	25.4	2.6	3.1	3.1	2.6	2.3	2.5	3.8	5.3	3.7	46.2	6.2	1857
	06-08	21.4	3.1	4.1	3.0	3.2	2.6	3.6	3.7	6.0	4.1	45.1	6.3	1857
	09-11	15.1	4.1	4.3	3.7	3.1	2.5	3.8	4.7	6.6	6.8	45.3	6.7	1856
	12-14	16.3	4.1	4.3	4.4	2.8	3.0	2.9	4.1	6.7	7.4	44.2	6.6	1857
	15-17	17.0	4.4	5.1	4.1	4.1	1.7	3.2	3.9	5.3	6.0	45.3	6.5	1857
	18-20	24.4	2.9	3.4	3.1	3.6	2.0	3.3	3.5	5.1	5.0	43.8	6.1	1858
	21-23	25.7	2.8	3.7	2.9	2.7	2.2	2.8	3.9	4.1	4.1	45.1	6.1	1857
TOTALS		21.4	3.3	3.9	3.4	3.0	2.3	3.1	3.9	5.6	5.1	45.1	6.3	14856

Table 3-16c. Percentage frequency of occurrence of cloud cover for Elmendorf AFB (from hourly observations), for July.

26401 STATION | ANCHORAGE ALASKA/ELMENDORF AFB STATION NAME | 46-52, 56-60 PERIOD | JUL MONTH

PERCENTAGE FREQUENCY OF OCCURRENCE
(FROM HOURLY OBSERVATIONS)

MONTH	HOURS (L.S.T.)	PERCENTAGE FREQUENCY OF TENTHS OF TOTAL SKY COVER											MEAN TENTHS OF SKY COVER	TOTAL NO. OF OBS.
		0	1	2	3	4	5	6	7	8	9	10		
JUL	00-02	6.9	3.0	3.5	3.3	3.6	3.0	3.4	4.2	7.6	7.3	54.2	7.7	1951
	03-05	5.2	2.9	3.5	3.0	2.8	3.5	3.2	3.6	8.0	8.4	55.7	7.9	1951
	06-08	4.9	3.3	3.7	2.9	3.0	2.5	3.2	5.0	5.7	8.7	57.2	7.9	1953
	09-11	5.7	3.1	2.7	3.6	2.7	3.3	4.0	4.5	7.8	9.4	53.1	7.8	1953
	12-14	5.8	2.6	2.8	3.7	4.2	3.3	4.3	5.4	7.7	10.2	50.2	7.7	1952
	15-17	5.7	2.4	3.5	4.6	4.0	3.4	4.8	5.2	8.0	10.3	48.0	7.6	1953
	18-20	5.1	2.6	3.9	4.0	4.8	3.0	3.8	5.9	8.1	9.8	49.0	7.6	1953
	21-23	5.1	4.0	3.6	3.9	3.8	3.6	3.0	5.1	7.6	8.5	51.7	7.6	1952
TOTALS		5.5	3.0	3.4	3.6	3.6	3.2	3.7	4.9	7.6	9.1	52.4	7.7	15618

Table 3-17. Summary cloud-cover percentages for California and southern Alaska (by percent).

Area	Season	Clear skies (%)	0 to 30% obscured	30 to 70% obscured	70 to 100% obscured	Overcast conditions (%)
Santa Barbara	Spring	25	35	15	50	35
	Summer	20	25	10	65	50
	Fall	30	40	15	45	30
	Winter	30	40	15	45	30
California desert	Spring	50	65	10	25	15
	Summer	65	80	10	10	5
	Fall	60	75	5	20	10
	Winter	40	60	5	35	20
San Bernardino	Spring	30	40	15	45	30
	Summer	45	70	10	20	10
	Fall	45	65	10	25	15
	Winter	35	50	5	45	25
Long Beach	Spring	30	45	10	45	30
	Summer	35	55	0	45	30
	Fall	40	55	5	40	25
	Winter	40	50	5	45	25
San Francisco	Spring	35	50	10	40	25
	Summer	60	75	5	20	15
	Fall	45	60	10	30	20
	Winter	25	35	10	55	40
Southern Alaska and the Aleutians	Spring	15	25	10	65	45
	Summer	5	15	10	75	50
	Fall	15	25	5	70	50
	Winter	20	30	10	60	45

encompassing the four seasons are spring, March through May; summer, June through August; fall, September through November; and winter, December through February. The occurrence frequencies are averaged to the nearest 5%. It is readily apparent that the skies almost always have few to no clouds or complete overcast; they practically never have scattered clouds in the 30 to 70% range. The highest frequency of clear skies is only 65%, during the summer in the California desert region east of the Sierra Nevadas. The San Francisco summer follows closely with 60% clear, as does the desert region in the fall. All other regions have clear days less than 50% of the time throughout the year, except for the desert region in the spring. Including cloud cover up to the 30% obscured range improves the picture only marginally.

4. APPROACHES TO CORRECTING FOR PROPAGATION ERRORS

It is quite apparent from the development of the previous sections that the range and range-rate errors attributable to tropospheric refractivity establish a lower limit for the accuracy and resolution of a Clogeos-like system. Tropospheric refractivity is by no means the only technical obstacle to deploying a space-based system with an accuracy of ±1 cm, but it is the least tractable problem, one that will simply not yield to state-of-the-art improvements to existing hardware.

The following subsections discuss the effectiveness of two possible approaches to correcting for tropospheric propagation errors: 1) multiple-wavelength optical systems, and 2) overconstrained-grid radio systems. The two approaches are described independently since each is a possible solution to the propagation problem. However, the two techniques are not mutually exclusive: A single- or multiple-wavelength optical ranging system could be incorporated into an overconstrained-grid concept.

It should be noted that the two systems are not strictly comparable. The first is a hardware solution with significant, but limited, quantitative performance data available from field use; the second is a data-processing technique, a sophisticated way of interpreting data from relatively unsophisticated instruments.

4.1 Multiple-Wavelength Optical Systems

It is possible to correct for tropospheric propagation errors to a range accuracy of about 1 cm for elevation angles greater than 15° by installing a two-wavelength monostatic optical radar in the Clogeos satellite and having the satellite receive returns from ground-based retroreflectors. This technique exploits the frequency dispersion of the tropospheric refractivity at

optical frequencies, not unlike the approach by which ionospheric propagation errors are corrected in the radio spectrum by the well-established dual-frequency method.

The theory of the multiple-wavelength optical system was discussed in Section 3.3. The effectiveness of such a system in correcting for tropospheric errors under real-world conditions has been analyzed by Thayer (1967), who generated a family of model atmospheres representative of the range of conditions likely to be encountered in nature. Computerized ray-tracing techniques were then employed to estimate the residual rms range errors for a single-wavelength optical system, a dual-wavelength optical system, and a triple-wavelength system (two optical wavelengths and one radio frequency; the radio frequency is necessary to correct for the contribution of the water-vapor term). The results of this analysis are shown in Figures 4-1 and 4-2. It should be noted that these two figures show residual range errors about the total refractive-index contribution of the troposphere of approximately 2.4 m. Therefore, it must be recognized that this analysis is an indication of the performance capabilities of multiple-wavelength systems and that large bias errors with seasonal and diurnal terms are possible. Also, the effects of turbulence or horizontal inhomogeneities were not considered, because of the difficulty of including them in the ray-tracing model.

Figure 4-1 shows an estimated range residual error of about 20 mm at zenith for a single-wavelength system, with the error rising to about 20 cm at an elevation angle α of 15°. For the dual-wavelength system, with λ_1 = 3660 Å and λ_2 = 6328 Å, the residual error is reduced to 2 mm at zenith and about 30 mm for α = 15°, with almost all the residual being the contribution of the water-vapor term. The estimate for the triple-wavelength case, neglecting the effect of the ionosphere on the radio frequency, is approximately 0.05 mm at α = 90° and 4 mm at α = 15°. Figure 4-2 presents the same data in a slightly different form, giving the ratio of residual errors for various combinations of systems as a function of zenith angle.

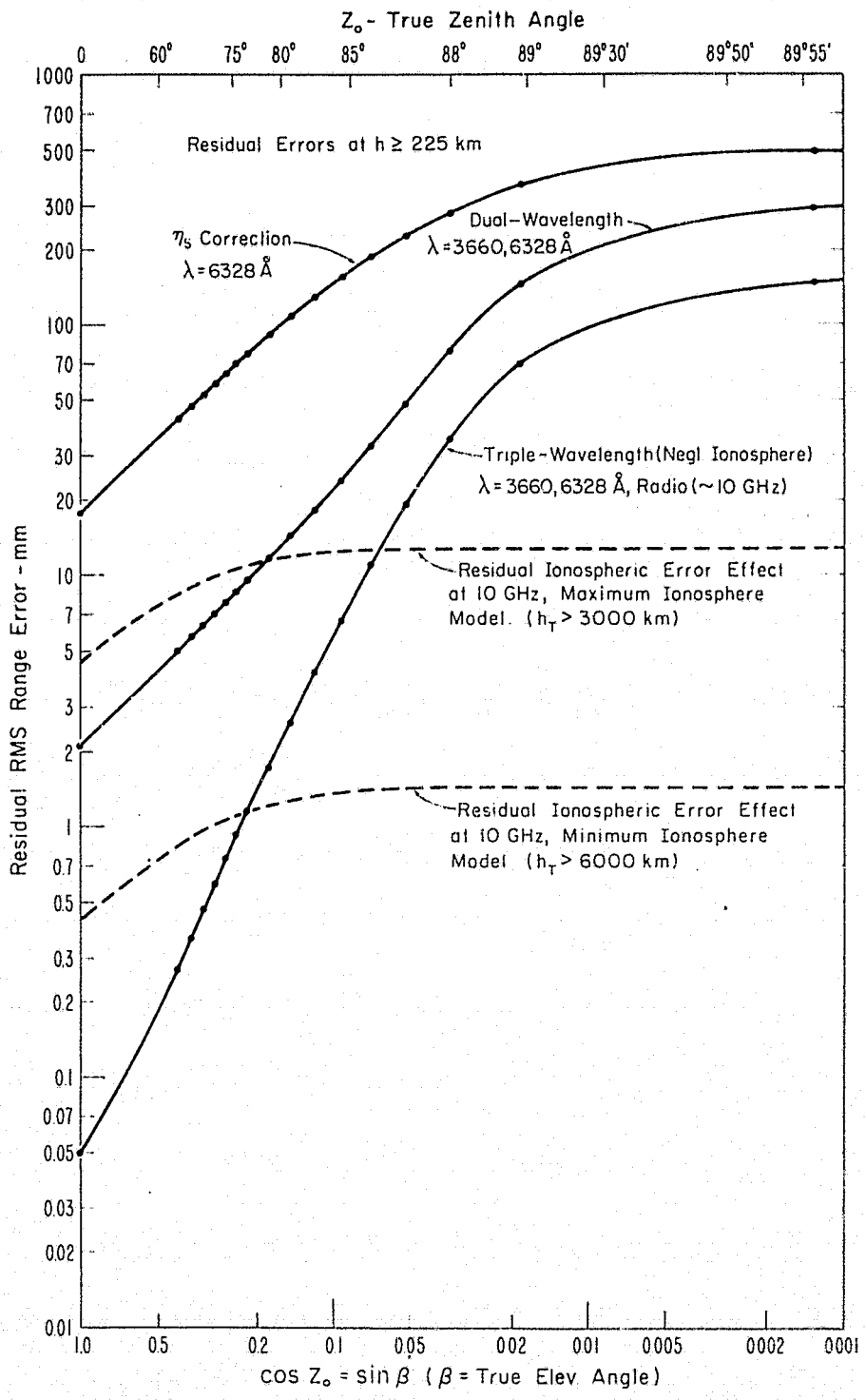

Figure 4-1. Ground-to-space residual errors for multiple-frequency ranging systems (from Thayer, 1967).

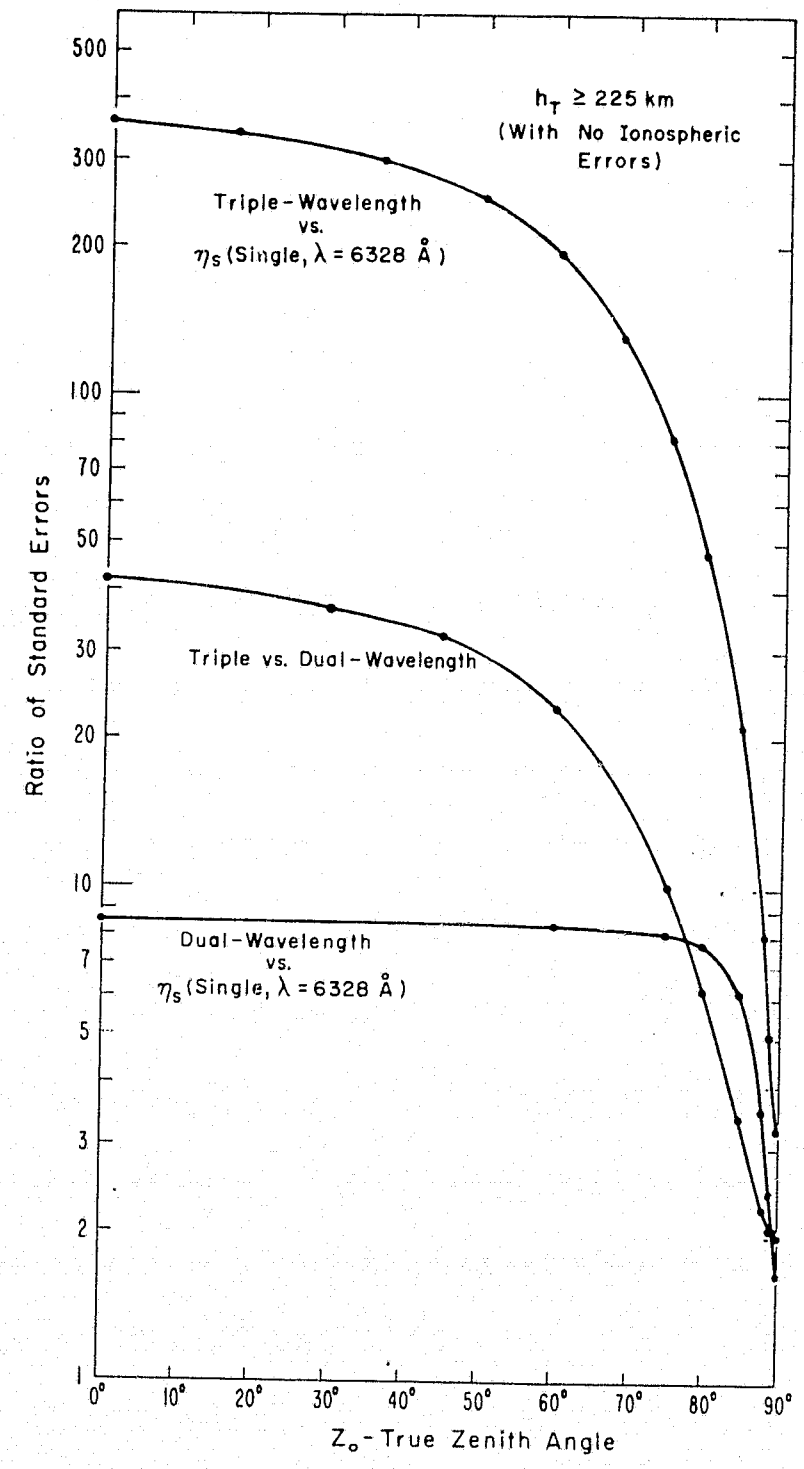

Figure 4-2. Relative residual errors of multiple-frequency ranging systems (from Thayer, 1967).

The single 10-GHz radio-frequency carrier is obviously adequate to provide an excellent estimate of the water-vapor contribution to the optical refractivity. In practice, however, in order to remove the ionospheric error in the 10-GHz link, a second microwave carrier, say at 5 GHz, must be added, making a total of four wavelengths, two optical and two radio, for a complete system.

4.2 Development Status of Multiple-Wavelength Systems

Owens and Earnshaw (1968), Earnshaw and Hernandez (1972), and Bouricius and Earnshaw (1974) have reported on the development of optical multiple-wavelength ranging systems that have demonstrated good capabilities for correcting for tropospheric errors in both monostatic and bistatic configurations. At the current state of development, these systems exhibit range ambiguities at 15-cm intervals and would require modification for application to a Clogeos system.

The most recent of these experiments (Bouricius and Earnshaw, 1974) obtained long-term residual errors of less than 1 cm over a horizontal 6-km path. The device employed two 15-mw continuous-wave gas lasers operating at 3683.6 and 6329.9 Å, each of which was polarization-modulated at approximately 2.0 GHz.

4.3 Overconstrained-Grid Systems

An overconstrained-grid system approach involves tracking a network of ground-based transponders from a geodetic satellite by using a two-way radio link operating in the VHF/UHF band. The proposed system would have a single-frequency downlink and a dual-frequency uplink. It would collect satellite-to-ground "apparent range" and "apparent velocity" data from nine transponders simultaneously, providing at least 16 good-quality data points in 25 observations.

The transponders would be 50 to 100 km apart and comprise a network covering 10^5 to 10^6 km^2 over a region of tectonic interest. Every 3 months or so, each transponder would be interrogated so that the system can detect the occurrence of motion and distortion in the ground-based transponder network.

The downlink would contain address codes to interrogate a specific group of transponders simultaneously. Transponder-to-transponder time interlacing would be ensured by delaying the answer of each transponder to a specific time segment. Each answer would contain the transponder's identification code, as well as information on the status of the base of the troposphere just above the array.

Auxiliary information would include data on ground pressure, temperature, and relative humidity collected by a grid of unattended meteorological posts located every 10 km or so in a circle centered around the transponder site. Data on winds, as well as measurements of pressure, temperature, and humidity taken on hills and mountains at various heights, would also be transponded to the satellite.

The auxiliary data and the primary range and doppler information would be telemetered to a ground-based data-collection center, where, after an initial reduction, they would be submitted to a process schematically illustrated in Figure 4-3. Other pertinent information collected, such as VLBI observations and high-accuracy radar-range determinations, would also be included in the data base.

During the processing, the ground-based meteorological data pertaining to the base of the troposphere above the network and collected as described above would be utilized to construct a first-cut tropospheric model for refractivity corrections; the ionospheric error would be totally removed from the data by the dual-frequency method in the uplink. Some information on tropospheric-refractivity variation versus height would be obtained from the tops of hills and mountains. Variation with height would be expressed by a polynomial expression. The model would interpolate between verticals 10 km apart, 10 km being the spatial width of the tropospheric-refractivity autocorrelation function, to cover the entire tracking array in three dimensions with a margin of 75 km from the most external sites. The model would be time invariant for medium-height satellite passes because the time width of the tropospheric autocorrelation function, 15 to 30 min, is longer than the pass duration. By bringing in models (Figure 4-3) of crustal dynamics, earth motion, and satellite dynamics, which are all assumed to be error free to start with, we could compare the apparent range and range-rate data collected by the satellite with a computer simulation of the same quantities constructed on the basis of the four models listed at the top of Figure 4-3.

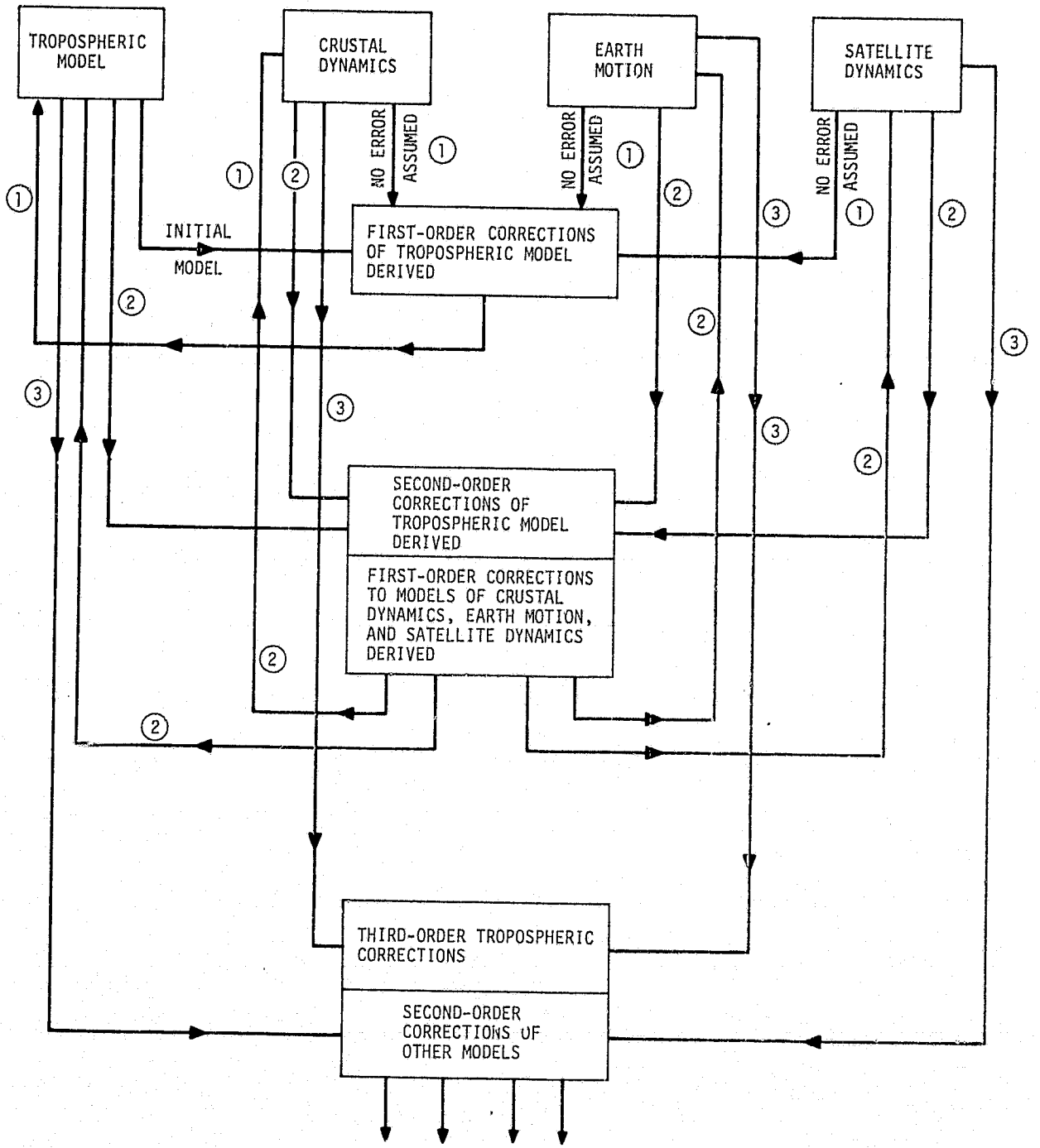

Figure 4-3. Block diagram of the computational procedure.

Discrepancies between the simulation and the observations would be attributed solely to the tropospheric model, which would be corrected accordingly until a good simulation/observations match is obtained. The computation cycle would then be iterated after introducing errors realistically attributable to the models of crustal dynamics, earth motion, and satellite dynamics. At the end of this step, we would have a second-order correction for the tropospheric model and a first-order correction for the other three models.

This process would be continued by also bringing in the tracking data corresponding to successive positions of the satellite in the entire pass above the complete return. Ultimately, we would arrive, for every pass, at an accurate determination of the satellite position, of the tropospheric refractivity, and of the geometry of the ground-based grid.

5. CLOGEOS SYSTEM INSTRUMENTATION

5.1 Introduction and Overall Considerations

A complete analysis of the instrumentation and its potential usefulness in implementing a Clogeos system is beyond the scope of this report. Rather, this section attempts to bound the problem, to provide a qualitative basis for further, more detailed studies of particular hardware configurations. It is not possible at this point to define "optimum" systems or to reach even tentative conclusions regarding the feasibility of a Clogeos system; however, an effort will be made to point out the merits and drawbacks of several approaches to the solution of the Clogeos problem.

The three major elements to the proposed system are as follows:

A. Grid-point ground equipment (markers). As pointed out in Section 2.1, the ground installation is a much more complex undertaking than might appear at first glance. In order to obtain 1-cm accuracy, the grid-point markers must maintain their relative positions to better than 1 cm in the absence of actual tidal or seismic motions. The implication is, of course, that the markers, whatever their nature, must be carefully emplaced to avoid spurious motion. Concrete monuments, excavated to bedrock, are undoubtedly a minimum requirement; in certain geological structures, more elaborate and expensive installations may be required. The markers must be able to provide a direct line of sight to the interrogation satellite over a wide range of elevation angles and azimuths. Further, the markers must be protected from earthquake or other accidental damage, vandalism, and snow or foliage cover and yet be accessible for service. The marker problem is compounded if the device requires a local source of operating power. The provision of either batteries (and the means to replace them regularly) or solar arrays immensely complicates the siting and logistics problems associated with the maintenance

of the grid.* If the additional requirement is imposed on the ground equipment that local environmental conditions (temperature, barometric pressure, and humidity) be measured and reported, then each grid-point site becomes a miniature weather station with all the associated instrumentation and shelters.

B. Satellite-borne interrogation equipment. The Clogeos concept places the complex, expensive portions of the system aboard the interrogation satellite. Although the details of the spacecraft instrumentation depend on the type of system selected, as discussed in the following sections, certain operational parameters are common to all systems. The most important of these is visibility; the spacecraft must be able to observe each of the grid points regularly and frequently since the accuracy of any satellite geodetic survey is a strong function of the number of data points available (I. Mueller, private communication, 1975). Unfortunately, this requirement implies a tradeoff between the signal-to-noise ratio, which is obviously better at low satellite altitudes, and the data rate, which improves rapidly with increasing satellite altitudes. Table 5-1 is a summary of a computer simulation showing the total time over a period of 7 days for which a grid point at 37°N is visible from satellites orbiting at altitudes of 500, 1000, and 2000 km. The satellite is assumed to be in a slightly retrograde circular polar orbit, and only elevation angles greater than 20° are considered useful. The increase in total observation time at the higher altitudes is apparent from the table. Furthermore, operating the interrogation satellite at altitudes of 1000 km or greater has an additional advantage: The ability to predict satellite ephemerides improves as atmospheric-drag effects decrease. Knowledge of the ephemeris is particularly important if precise pointing mechanisms are required aboard the satellite to aim narrow laser beams at specific grid markers.

C. Data-reduction and data-analysis programs. Data analysis and data reduction are integral components of virtually every satellite experiment. The Clogeos program differs from most in one important respect, however: Although a very large amount of data must be processed, nothing of interest may occur for long periods of time, perhaps for many years. Therefore, the

*Alternative power sources, such as radioactive thermal generators, cannot be considered for ground stations because of radiological hazards, both real and imagined.

Table 5-1. Total time of visibility for elevations >10° (7-day period only).

500-km orbit	
	110 min of passes where peak elevation >20°
	29 min of passes where peak elevation <20°
	139 min, total time of visibility
1000-km orbit	
	297 min of passes where peak elevation >20°
	52 min of passes where peak elevation <20°
	349 min, total time of visibility
2000-km orbit	
	646 min of passes where peak elevation >20°
	97 min of passes where peak elevation <20°
	743 min, total time of visibility

data analysis must be routine, efficient, and relatively inexpensive in order to avoid the almost inevitable temptation to trim costs by reducing or eliminating the analysis phase if immediate results are not forthcoming.

Clogeos systems can be designed to operate in either the radio or the optical portion of the electromagnetic spectrum. In both spectral regions, range or range-rate instrumentation can, in principle, be designed and implemented. In practice, certain techniques or combinations of techniques must be excluded from serious consideration because of insufficient development to date. The rest of this section discusses some of the considerations involved in using radio range, radio range-rate, and optical systems for Clogeos.

5.2 Radio Range Systems

The radio ranging systems are essentially conventional pulsed radars operating in the active transponder mode. Although there are a number of other problems associated with the use of a radio ranging system in Clogeos applications, the stringent time-resolution requirements alone are sufficient to eliminate this class of systems from serious consideration. Range accuracies on the order of ±1 cm require time-delay measurements with accuracies on the order of ±60 psec. It can be shown (Skolnik, 1962) that

$$\delta T_R = \frac{1}{B(2SNR)^{1/2}} \quad , \tag{5-1}$$

where δT_R is the error in the time-delay measurement for a single pulse, B is the system bandwidth, and SNR is the postdetection signal-to-noise ratio. For simple noncoherent detection systems, the signal-to-noise ratio must be larger than 1. If we arbitrarily select a minimum value of SNR = 10 and calculate the system bandwidth using the realistic link parameters shown in Table 5-2 for an uplink path between a marker transponder and an orbiting radar transmitter/receiver, then the maximum bandwidth is approximately 1.0 MHz. Putting this value into equation (5-1), we obtain

Table 5-2. Uplink signal-margin analysis.

Parameter	Nominal value
Carrier frequency	8500 MHz
Range	1000 km
Transmitter power (ground)	100 w (peak)
Receiver noise figure (satellite)	10 db
Transmitter antenna gain (ground)	0 db (omnidirectional)
Receiver antenna gain (satellite)	20 db
Free-space attenuation	171.45 db
Received power	-141.45 dbm
Carrier-to-noise ratio	62.54 db

$$\delta T_R = \frac{1}{10^6(2 \times 10)^{1/2}} \simeq 2 \times 10^{-7} \text{ sec} \quad , \tag{5-2}$$

an error approximately 3×10^3 larger than the derived time-delay uncertainty of 60×10^{-12} sec. The problem is actually intractable; the time-delay uncertainty improves only as the square root of the received signal strength, so the transmitter peak power, or the antenna gain, must be increased by a factor of 10^7 to satisfy the system requirements (if the bandwidth is maintained constant). Alternatively, both the received power and the system bandwidth can be increased by factors of 3×10^3, an equally unpalatable prospect. Of course, pulsed radar signals average a large number of time-delay measurements to obtain an estimate of the range. However, the time-delay uncertainty decreases only as the square root of the number of measurements, but effective use of pulse averaging is complicated by the rapid motion of satellites with respect to the grid-point-marker transponders.

It should also be noted that the accuracy of any transponder ranging system is a function of the absolute stability of the transponder time delay. Any change in this time delay is indistinguishable from actual physical movement of the transponder, and signal averaging or other processing techniques are not applicable for correcting this type of error. Long-term time-delay stabilities of less than ±60 psec would be very difficult to obtain for conventional pulsed radar transponders; typical values for state-of-the-art transponders currently in service are 0.5 to 2.0 nsec, which is equivalent to marker displacements of 7.5 to 30 cm.

5.3 Radio Range-Rate Systems

The prototype radio range-rate location system is the familiar U.S. Navy Transit system, which employs a constellation of medium-altitude (500-km) satellites in inclined circular orbits. Stable crystal oscillators aboard the satellites control the carrier frequencies of two downlink transmitters at 225 and 450 MHz. An updated satellite ephemeris, loaded into the spacecraft from ground control systems, is modulated onto the lower

frequency carrier. Ground stations passively receive satellite transmissions and interpret the doppler signature to calculate the location of the receiver. Two transmission frequencies are necessary to exploit the dispersivity of the ionosphere and to correct for ionospheric refractivity errors.

A typical Clogeos system could be similar to the Transit concept except that the ground receivers would be replaced by phase-coherent transponders to retransmit the received carrier frequencies to the interrogating satellite. Extracting the doppler information would be performed by instrumentation aboard the spacecraft. This "two-way" doppler system would offer a major advantage over the one-way Transit approach in that instabilities of the spacecraft's master oscillator, to first order, would be canceled. Master-oscillator noise and drift are serious sources of both random and systematic errors in the Transit-type radio location systems.

5.3.1 System description

A typical two-way doppler system suitable for Clogoes applications is shown in block diagram form in Figure 5-1. In this concept, the satellite transmits one downlink frequency to the coherent radio transponder at the grid point. The phase-lock receiver in the transponder locks onto the carrier frequencies and retransmits two carrier frequencies, coherently offset from the received one, back to the satellite. The satellite receivers then compare the uplink frequencies with the transmitted frequency, extracting the doppler component of the difference. These data are digitized, stored in the spacecraft memory, and telemetered to the ground on command.

A number of grid points can be monitored during a given pass by frequency diversity, in which several downlink carrier frequencies are transmitted simultaneously and a pair of receivers is provided for each uplink. Each grid-point transponder could be tuned to respond only to a specified downlink frequency, although all transponders in the grid would otherwise be physically identical.

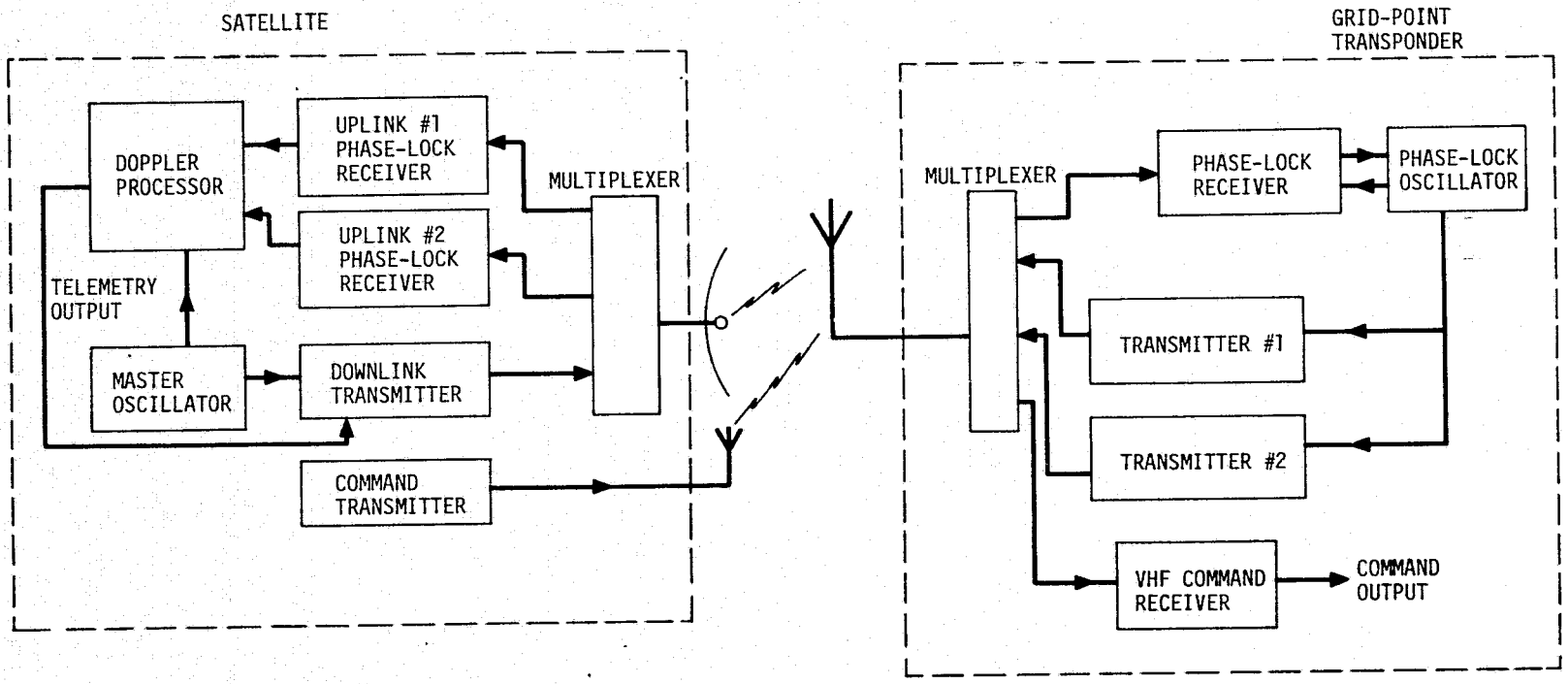

Figure 5-1. Block diagram of the radio doppler system.

The doppler-frequency change of a two-way doppler system varies directly as the carrier frequency for a given radial velocity. Thus, the highest possible carrier frequencies compatible with economic, power-consumption, and atmospheric-attenuation considerations would be desirable for a Clogeos application. S-band frequencies (2000 to 3000 MHz) are a good choice for initial studies, especially since a great deal of hardware has been developed for the unified S-band tracking and communications networks. However, UHF transmitters and receivers are relatively inefficient, and the standby power drain would probably prove to be excessive for a battery-powered grid-point transponder. A desirable component of the overall system, therefore, would be an addressable command receiver operating in the VHF range at approximately 100 MHz. During stand-by periods, only the command receiver would be powered. A VHF transmitter aboard the satellite would command the grid station via the command receiver to power the S-band transponder up and down. When only specific grid stations are called for, the command transmitter could send coded sequences to address individual or selected groups of grid stations. VHF command receivers consume very lower power, requiring only 200 to 400 mw of battery power for normal continuous operation and slightly more when addressed by an interrogation satellite.

5.3.2 Grid-point transponder

A typical grid-point transponder for a radio range-rate system is shown in block-diagram form in Figure 5-2. The center frequency of the received carrier is assumed to be 2300 MHz, and the coherent retransmission frequencies are precisely 240/229.5 and 480/229.5 times the received carrier frequency.

The transponder is actually a single phase-lock loop with almost all the phase-critical components — oscillators, frequency multipliers, and dividers — located within the loop to minimize environmentally induced phase shifts. If it is assumed, for convenience, that the 10.02179-MHz voltage-controlled crystal oscillator (VCXO) has been locked in phase to the incoming carrier signal, then the first local-oscillator signal, which is sampled from the output of the lower frequency transmitter's power amplifier, will be at exactly

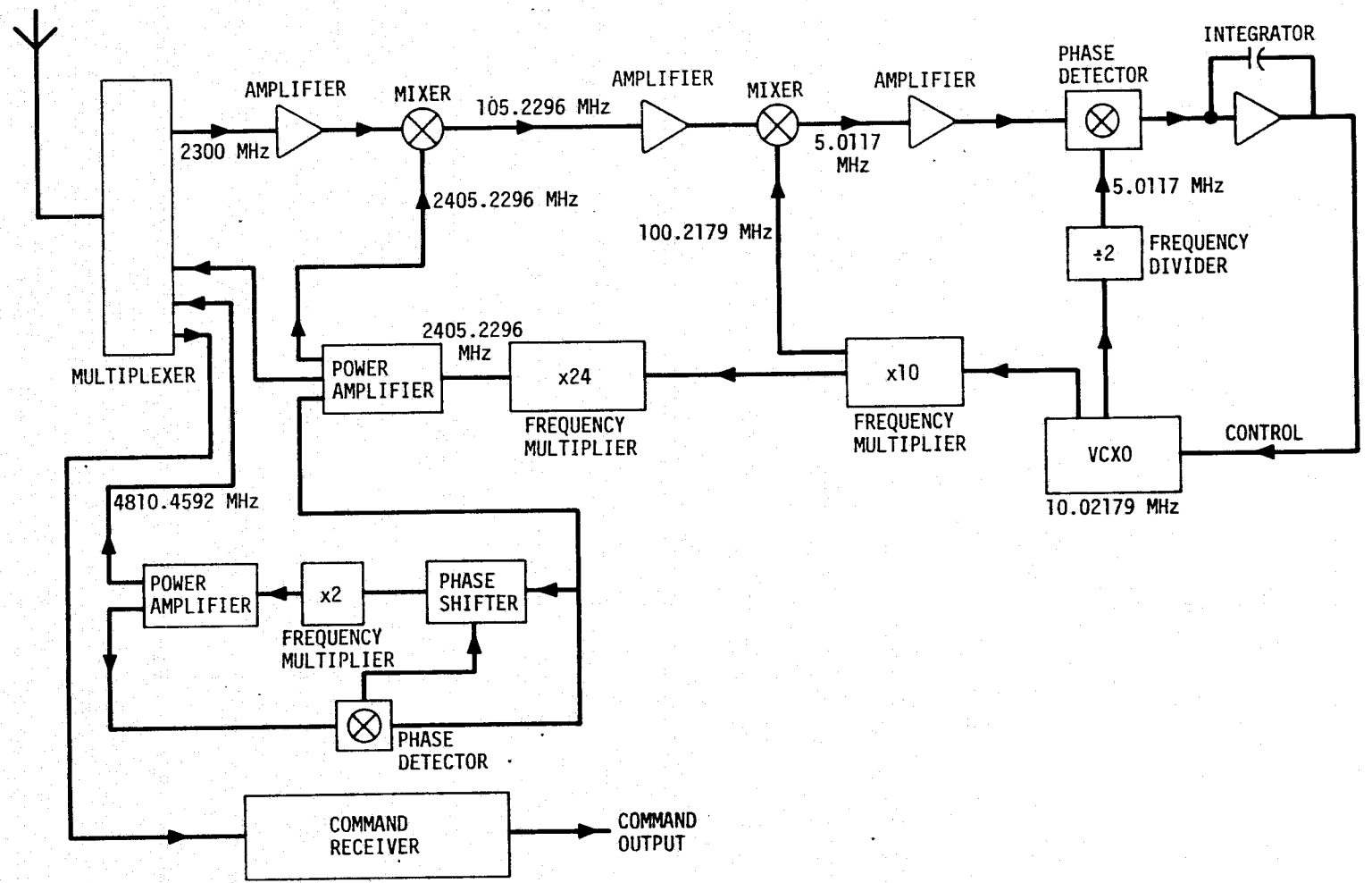

Figure 5-2. Block diagram of the grid-point transponder.

240 × 10.02179, or 2405.2296 MHz. The first intermediate frequency (IF), therefore, is 105.2296 MHz. The IF signal is filtered, amplified, and mixed with the tenth harmonic of the VCXO to yield a second IF signal at 5.0117 MHz, which is then amplified and filtered to form one input to the phase detector; the reference for the phase detector is the VCXO frequency divided by 2. The output of the phase detector is amplified, low-pass filtered, and used to hold the VCXO frequency phase-locked to the received carrier frequency.

The output of the power amplifier at 2405 MHz is also used to drive a ×2 frequency multiplier, which generates the 4810-MHz uplink frequency. The 4810-MHz signal is amplified by a second power amplifier before transmission. The frequency multiplier and 4810-MHz power amplifier are outside the main phase-lock loop, and phase shifts in this portion of the circuit will not be corrected by negative feedback within the loop. The auxiliary phase correction shown in Figure 5-2 uses a harmonic mixer to compare the phase of a sample of the output of the 4810-MHz power amplifier with the second harmonic of the 2405-MHz amplifier. The resulting error signal is amplified and fed back to an electronically controlled delay line to maintain phase coherence between the two transmitted carrier signals.

Frequency multiplexing can be used effectively in a radio range-rate system to interrogate many grid points simultaneously. A large number of carrier frequencies, limited only by frequency allocations and physical constraints, can be transmitted from the satellite, each carrier addressed to a different grid-point transponder. The transponder, as described, is tuned to receive a carrier signal at a nominal center frequency of 2300 MHz. The receiver frequency can be varied over a wide range, 100 to 200 MHz, by properly selecting the VCXO frequency and retuning the frequency multiplier and IF amplifier filter circuits. The transponder ratio, the ratio of the transmitted to the received frequency, remains constant at 240/229.5. This technique permits each of the transponders in the grid to be physically identical, thus contributing to lower unit costs.

The function of the VHF command receiver shown in Figure 5-2 was discussed in Section 5.3.1. Power input to the S-band receiver and the two uplink

transmitters is under the control of the command receiver, which, in turn, is controlled by coded command signals from the interrogation satellite. A backup timer and associated logic, internal to the transponder, limit the on-time of the transponder in the event that power-off commands from the satellite are improperly received or are misinterpreted.

A single vertically polarized monopole antenna is employed for reception of the S-band tracking and VHF command signals and for retransmission of the two uplink carriers. This antenna offers a relatively uniform azimuthal power pattern with a rather deep null at zenith. However, the probability of a satellite pass directly overhead through the null of the antenna is small, and very few data would be missed because of the loss of signal strength near zenith.

Additional auxiliary circuitry is required to sweep the frequency of the VCXO for phase-lock acquisition, to charge batteries, and to detect and report internal malfunctions. The transponder is packaged into a gasket-sealed housing approximately 20 cm × 15 cm × 15 cm, exluding batteries and primary power supplies. Total power consumption, assuming approximately 0.5-w output for both uplink transmitters, is approximately 7 w in the transpond mode and less than 0.5 w in the stand-by mode.

5.3.3 Satellite transmitter/receiver

The block diagram in Figure 5-3 shows the satellite transmitter/receiver configuration. The transmitted downlink frequency is assumed to be 2300 MHz, and the nominal center frequencies of the two uplinks are 2405 and 4810 MHz.

The transmitter is a simple frequency multiplier and power amplifier driven by the satellite's master oscillator, a 10-MHz precision crystal oscillator. The 10-MHz input signal is multiplied by 230, filtered, amplified to the 5-w level by a transistor or traveling-wave-tube power amplifier, and routed through a multiplexer to the satellite's directional antenna. A sample of the power-amplifier output is used as the first local-oscillator signal for the satellite uplink receivers.

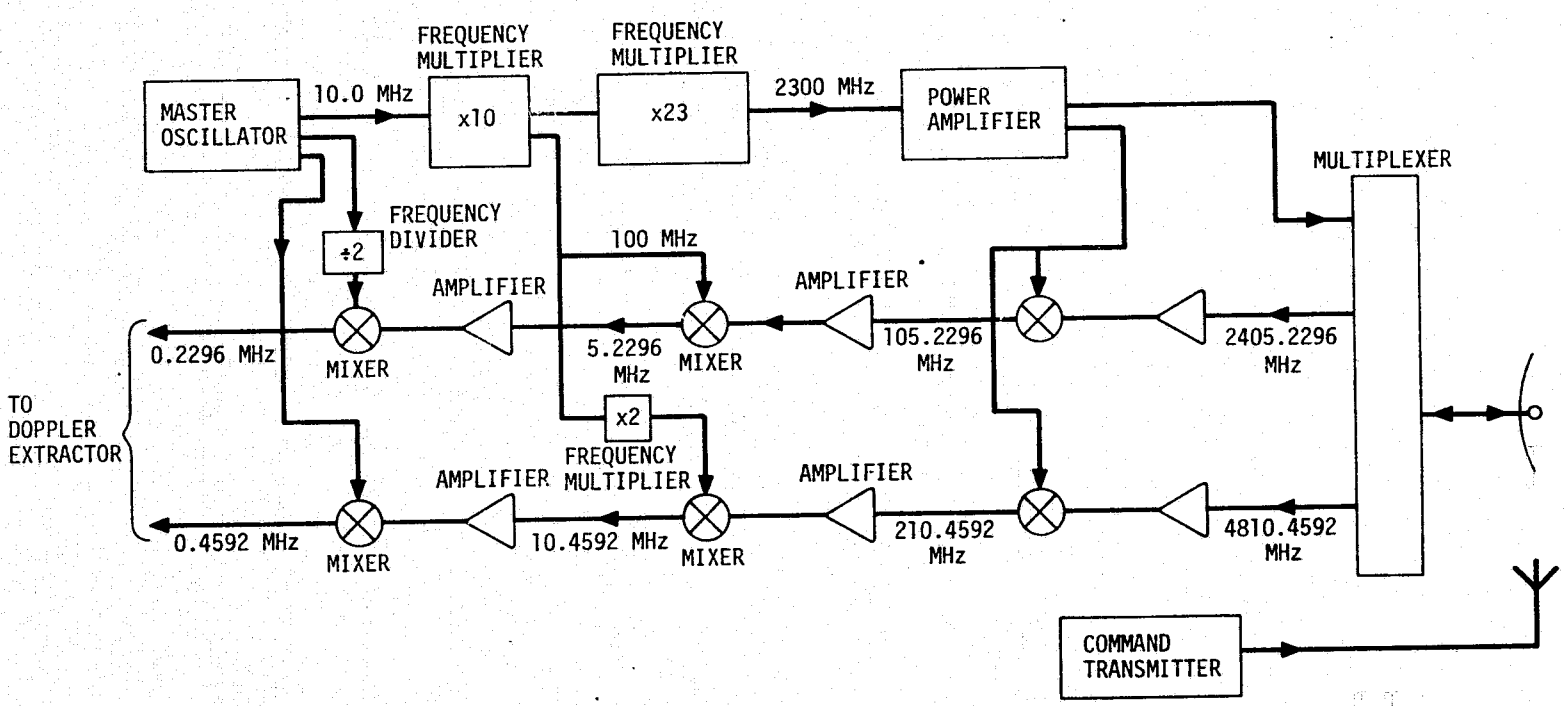

Figure 5-3. Block diagram of the satellite transmitter/receiver.

The two receivers at 2405 and 4810 MHz utilize the fundamental and second harmonics, respectively, of the transmitted frequency as the first local-oscillator signal. Thus, the first IF amplifier frequencies are nominally 105 and 210 MHz. The second local-oscillator frequencies, also tapped off the transmitter's frequency-multiplier chain, are 100 and 200 MHz, producing second IF signals at 5 and 10 MHz. (These are nominal values; the actual center frequencies are approximately 5.2296 and 10.4592 MHz, respectively.) The third local-oscillator signals, 5.0 and 10.0 MHz, are derived directly from the satellite's master oscillator and are used to produce intermediate frequencies of 229.6 and 459.2 kHz in the two received channels.

These two IF signals are sufficiently low in frequency to be digitally processed by the satellite's doppler extractor, yet high enough to prevent the frequency from going near or through zero for the worst-case doppler shift.

For multiple-transponder accessing, an additional transmitter/receiver is required for each grid point to be interrogated. The basic block diagram remains that of Figure 5-3, except that the transmitted and received frequencies are different, in steps of 5 to 10 MHz, from the prototypical design described above. A large number of simultaneous transmissions would require the use of digital synthesizers to generate the transmitter output and receiver local-oscillator frequencies in place of the simple frequency-multiplier chain shown in the figure.

The command transmitter operates at approximately 110 MHz, transmitting through its own antenna system. The carrier is frequency-shift keyed by pre-programed code sequences, under on-board computer or ground control, to select specific grid-point transponders. The addressed transponders, and only those, are turned on to an active mode during a given satellite pass. In general, only five to 10 transponders will be activated at one time because of satellite-equipment limitations and the relatively small size of the satellite antenna beam's footprint.

5.3.4 Satellite antenna

The satellite antenna is a steerable parabola, 1 m in diameter, that transmits and receives circularly polarized waves in the 2300- to 4800-MHz range. (A separate, turnstyle antenna is used for the VHF command transmissions.) The antenna half-power beamwidth is 4.4 at 4810 MHz. The resulting footprint on the earth's surface from an altitude of 1000 km is a spot approximately 77 km in diameter,* too small to encompass an entire Clogeos grid. Therefore, the antenna must be steerable by satellite or ground command to point at the desired portion of the grid, and this pointing must be coordinated with the addressing of grid-point transponders within the selected portion of the grid.

5.3.5 Satellite doppler extractor

The doppler extractor is basically a pair of multiple-period-average frequency counters, one for each uplink receiver. Figure 5-4 is a block diagram of the two-channel doppler extractor, showing the two input signals at center frequencies of 229.6 and 459.2 kHz. Since the operation of both counter chains is identical, only the lower-frequency processor is described in the following.

The input frequency to the doppler extractor, nominally 229.6 kHz, varies from approximately 100 to 300 kHz, depending on the magnitude and sign of the two-way doppler shift of the received 2405.229-MHz carrier. Immediately after an initializing reset, the first positive-going zero crossing of the input opens the main gate, which begins the count of a 100-MHz clock in the X counter register. The same zero crossing starts the countdown of a preset 10-sec timer, Y. The zero-crossing counter Z counts the total number of crossings that occur while the main gate is open. At the expiration of the 10-sec counting period, the timer enables the end-of-count logic, which, in turn, closes the main gate at the first zero crossing after expiration of the 10-sec interval. A time delay of 10 μsec before the next reset pulse provides time for the control logic to transfer the contents of the X and Z counters into storage registers. The contents of the X and Z registers, taken together, completely characterize

* This calculation is for a satellite at zenith. At lower elevation angles, of course, the footprint is elliptical in shape.

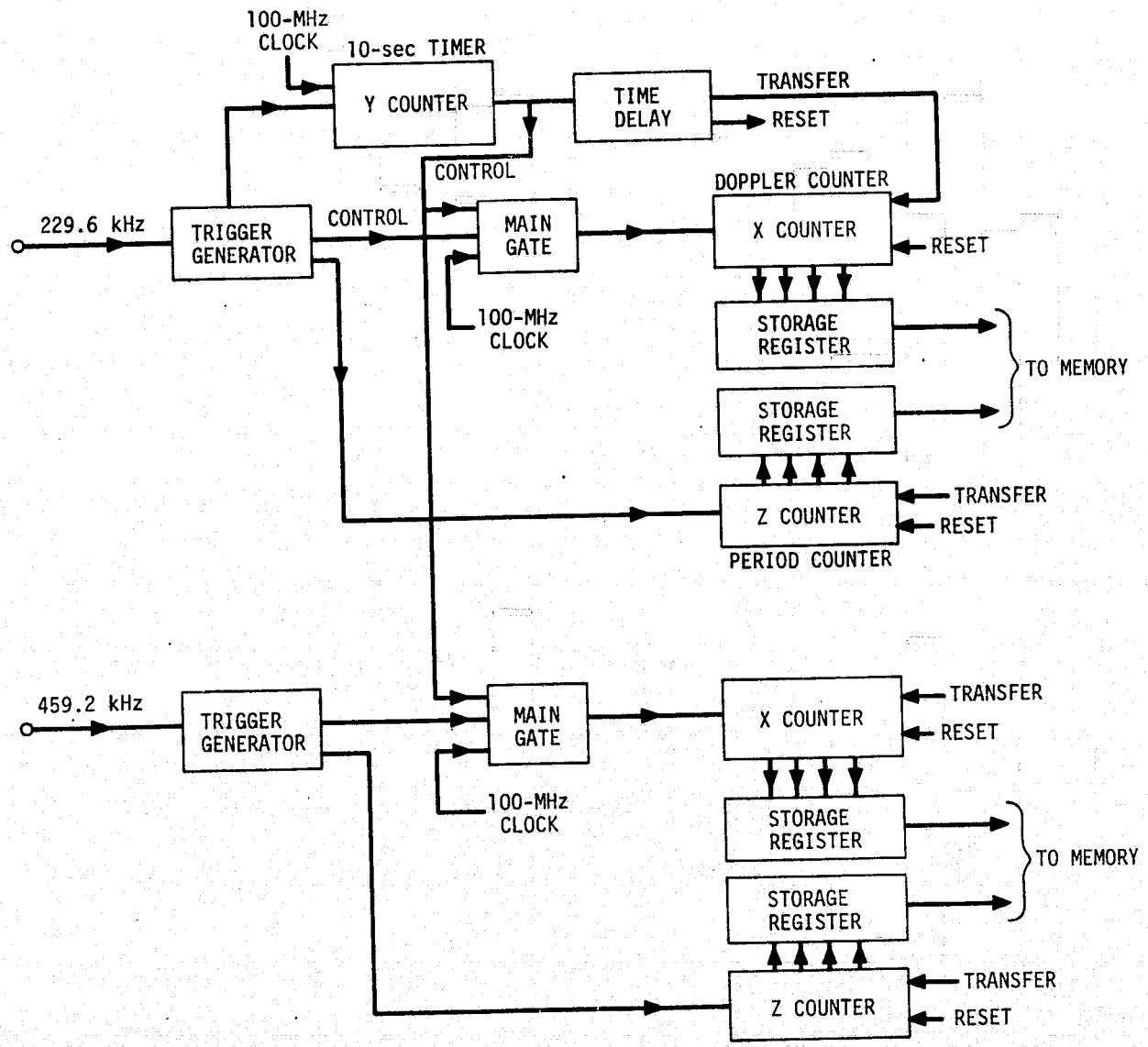

Figure 5-4. Block diagram of the satellite doppler extractor.

the frequency of the doppler-extractor input signal and form the doppler word. The efficiency of data storage can be increased by allowing the X register to overflow, as only the least-significant digits of the register contain non-redundant information. Including epoch, taken from the satellite's master clock, 32 bits are required for each doppler word.

Each pass over a Clogeos grid would generate a maximum of 60 doppler words per channel. A practical maximum of 10 simultaneous two-channel observations would generate approximately 1200 32-bit words per pass. Therefore, a random-access-memory main memory of 2K bytes would be the maximum size required under worst-case conditions. Mass storage could be provided by a digital tape recorder, which would come from main memory and be under command from the control logic. The tape-recorder memory would need a capacity sufficient to allow at least one full day of operation between data dumps to a ground station.

No on-board data processing would be attempted, all doppler information being transmitted to ground stations. Off-line processing equipment would extract the ionospheric doppler information by comparing the measured doppler shift on the two transponder channels (Grossi and Gay, 1976; Gay and Grossi, 1976) and correct the lower frequency range-rate data for ionospheric refraction. The positions of the grid-point transponders would then be computed from standard programs.

5.3.6 System performance

The system parameters outlined in the previous sections are summarized in Table 5-3.

Doppler measurements in a Clogeos system would be limited by two instrumental factors, signal-to-noise ratio and frequency-measurement resolution, discussed separately below.

Table 5-3. System parameters.

Parameter	Nominal value
Satellite	
Orbit	Circular, near-polar
Altitude	1000 km
Transponder	
Receiver channel	1
Transmitter channels	2
Receiver frequency range	2300 to 2400 MHz
Transmitter frequency range	2400 to 2500 MHz, 4800 to 5000 MHz
Antenna gain	-10 db
Receiver noise figure	6 db
Transmitter power	0.5 w, each channel
Satellite transmitter/receiver	
Receiver channels	2
Transmitter channel	1
Receiver frequency range	2400 to 2500 MHz, 4800 to 5000 MHz
Transmitter frequency range	2300 to 2400 MHz
Antenna gain	
2405 MHz	25.3 db
4810 MHz	31.4 db
Antenna beamwidth (half-power)	
2405 MHz	8°9
4810 MHz	4°4
Receiver noise figure	6 db
Transmitter power	5.0 w, each channel
Satellite doppler extractor	
Input frequencies	200 ± 100 kHz, 400 ± 200 kHz
Clock resolution	100 MHz (10^{-8} sec)

The signal-to-noise ratio of a complete round-trip measurement determines the phase uncertainty of the resultant doppler signal and therefore limits the accuracy of a range-rate measurement. It can be shown (Skolnik, 1962) that the uncertainty in a frequency measurement is given by

$$\Delta F_1 = \frac{1}{2\pi (CNR)^{1/2} T} \quad , \tag{5-3}$$

where T is the observation interval and CNR is the carrier-to-noise ratio in the system bandwidth. Ionospheric correction requires that two measurements be made to compensate for refractivity errors. Therefore, equation (5-3) becomes

$$\Delta F_2 = \frac{\sqrt{2}}{2\pi (CNR)^{1/2} T} \quad . \tag{5-4}$$

It can readily be seen from Table 5-3 that because of the limited power capability of the transponder amplifiers, the transponder-to-satellite uplink is the determining factor in the overall system signal-to-noise ratio. Table 5-4, therefore, is a link-margin analysis for both uplink channels. The low-frequency uplink introduces the larger equivalent random-velocity error, slightly less than 10^{-5} m/sec for the link parameters selected.

The frequency-measurement resolution error is a function of the last intermediate frequency and the clock rate of the doppler-extractor counter. The resolution error for the doppler extractor shown in Figure 5-4 is identical for the two channels, so only the low-frequency, 2405-MHz carrier will be considered here. The two-way doppler shift at the satellite receiver is

$$\Delta F_d = \frac{2 v_r f_c}{c} \quad , \tag{5-5}$$

where v_r is the radial velocity, c is the velocity of light, and f_c is the carrier frequency. The time difference associated with a given frequency shift ΔF_d is

Table 5-4. Link-margin analysis of the uplink channels.

Parameter	Nominal value	
	2405 MHz	4810 MHz
Transmitter power	0.5 w	0.5 w
Transmitter antenna gain	-10 db	-10 db
Range	1000 km	1000 km
Free-space attenuation	160.5 db	166.5 db
Polarization loss	3 db	3 db
Cable loss	2 db	2 db
Receiver antenna gain	25.3 db	31.4 db
Receiver power	-123.2 dbm	-123.2 dbm
System bandwidth	10 Hz	10 Hz
Carrier-to-noise ratio	34.8 db	34.8 db
Averaging time	10 sec	10 sec
ΔF_2	4.1×10^{-4} Hz	4.1×10^{-4} Hz
Equivalent velocity error (random, per 10-sec measurement)	5.9×10^{-3} mm/sec	2.9×10^{-3} mm/sec

$$\Delta T_c = \frac{2v_r T}{c} \quad . \tag{5-6}$$

The time difference referenced to the last IF, f_I, is

$$\Delta T_I = \frac{f_c 2v_r T}{f_I c} \quad . \tag{5-7}$$

For a given time resolution ΔT_I, the minimum detectable change in radial velocity can be written as

$$\Delta v_r = \frac{c f_I \Delta T_I}{2 f_c T} \quad . \tag{5-8}$$

If $c = 3 \times 10^8$, $f_I = 299$ kHz, $f_c = 2405$ MHz, $T = 10$ sec, and $\Delta T_I = 10^{-8}$ sec (1/100 MHz), then

$$\Delta v_r = 1.4 \times 10^{-5} \text{ m/sec} \quad \text{or} \quad 1.4 \times 10^{-2} \text{ mm/sec} \quad .$$

Thus, the system resolution is compatible with system noise, and the overall instrument accuracy of the radio range-rate system described is approximately 2×10^{-2} mm/sec.

5.4 Optical Systems

Optical measuring systems using lasers offer very high-gain (directional) transmitting antennas and the possibility of passive ground stations with no transponder time jitter; operating in the optical spectrum also minimizes the refraction error. Drawbacks to the two-way optical system include the large path losses and the susceptibility to cloud cover, plus the chance of some ground-clutter problems under certain conditions.

A number of groups are currently employing pulsed laser systems to range from ground stations to satellites for geophysical research. These systems are essentially optical radars that use short-pulse lasers (a few nanoseconds or less) as transmitters and retroreflectors as remote transponders. The photodetectors are photomultipliers with appropriate collecting optics and spatial and spectral filtering. Except for the problems of pointing from a moving spacecraft and the presence of ground clutter, the inverted system would basically be the same as those now in use.

With this type of system, a sufficient number of return photoelectrons from the retroreflector must be accumulated to average measurements to the required accuracy in a period short enough to isolate the smallest feature of interest. In the most stringent case, each return pulse must have enough photoelectrons for range to be determined to the desired accuracy.

In the following subsections, we discuss some of the specific factors to be considered in evaluating the usefulness of optical systems for the Clogeos project.

5.4.1 Received energy

The energy received from a distant (ground) retroreflector is given in terms of photoelectrons by the range equation (Skolnik, 1965)

$$N = \frac{E_T D_R^2 E_f \eta (T_0 \cos \phi)^2 \sigma_s}{2\pi \theta_T^2 R^4 h\nu} \quad , \tag{5-9}$$

where E_T is the transmitted energy per pulse, D_R is the receiver aperture diameter, E_f is the receiver optical efficiency, η is the photocathode quantum efficiency, T_0 is the atmospheric transmission at zenith, ϕ is the zenith angle to the satellite, θ_T is the output beam divergence, R is the range to the target, $h\nu$ is the energy per photoelectron, and σ_s is the retroreflector-array cross section. We can expect a return signal strength at zenith of about 2500

photoelectrons if we use the following parameters for the spacecraft and ground system: E_T = 0.25 Joule, D_R = 30 cm, E_f = 30%, η = 0.03, T_0^2 = 0.5, θ_T = 0.5 mrad, ϕ = 0°, σ_s = 0.6 x 10^6 m^{-2} (the retroreflector-array cross section for the Starlette satellite), and satellite altitude H = 500 km. The returns at zenith angles of 45° and 60° are 310 and 40 photoelectrons, respectively. For these three zenith angles and a satellite altitude of 1000 km, the average return signal strength becomes 150, 20, and 2 photoelectrons, respectively.

These are typical parameters that can be expected for a small narrow-pulse ruby-laser system (pulse width of 5 nsec or less) at 6943 Å. Although short-pulse doubled Nd^+ Yag laser systems operate closer to a 0.1-Joule output, and atmospheric attenuation is a bit larger owing to Mie scattering, detection-system efficiencies at 5300 Å are a factor of 4 greater than at the ruby wavelength and the results should be comparable.

5.4.2 Noise sources

5.4.2.1 Background clutter

Near zenith, the dominant signal-to-noise problem with the inverted ranging concept will be background clutter. The laser beam illuminates a spot on the ground around the retroreflector array, which produces a backscattered signal. At zenith (or very high elevation angles), the spot on the ground is a circle of radius $\theta_T R/2$, and the signal-to-clutter-noise ratio (SNRC) becomes

$$SNRC = \frac{\sigma_s}{\pi(\theta_T/2)^2 R^2 \rho} , \qquad (5\text{-}10)$$

where ρ is the earth's albedo at the laser wavelength. Using an average albedo of 0.5 and assuming σ_s = 0.6 × 10^6 m^{-2}, R = 500 km, and θ_T = 0.5 mrad, we get SNRC ∼ 25; this ratio decreases to 6 at an orbital altitude of 1000 km.

Off zenith, the ratio of the received energy from the retroreflector to that of the background decreases as $(R^2 \cos \phi)^{-1}$ owing to the increased range and the aspect angle of the illuminated region (assumed Lambertian). However, the SNRC improves dramatically because of the distribution in time for the clutter return signal. If the pulse width of the laser $\Delta\tau$ is considerably less than the dimensions of the beam-intersected ellipse on the ground, then the laser beam illuminates only a segment of the ellipse at that time (see Figure 5-5). The area intercepted, $\Delta A(\phi,t)$, then becomes

$$\Delta A(\phi,t) = 2\sqrt{(\phi_T R/2)^2 - c^2(t - t_0)^2 \cot^2 \phi}\left(\frac{c\,\Delta\tau}{\sin \phi}\right) \quad , \tag{5-11}$$

where c is the speed of light and t_0 is the range time to the center of the ellipse. The clutter cross section then becomes

$$\sigma_n(\phi,t) = \rho\, \Delta A(\phi,t) \cos \phi \quad . \tag{5-12}$$

The return from the retroreflector, on the other hand, is instantaneous in time and can be written as

$$\sigma_s(\phi,t) = \sigma_s(\phi)\, \delta(t) \tag{5-13}$$

if we assume that the array is at the center of the ellipse. Then,

$$SNRC(\phi,t) = \frac{\sigma_s(\phi)\, \delta(t - t_0) \sin \phi}{2\rho\sqrt{(\theta_T R/2)^2 - c^2(t - t_0)^2 \cot^2 \phi}\, c\, \Delta\tau \cos \phi} \quad . \tag{5-14}$$

For $\phi = 45°$ and t close to t_0, where the noise is maximum, we have

$$SNRC \sim \frac{\sigma_s(\phi)}{c\theta_T R\, \Delta\tau\, \rho} \quad . \tag{5-15}$$

Using the earlier example with θ_T = 0.5 mrad, ρ = 0.5, and $\Delta\tau$ = 5 nsec, the SNRC is in excess of 1000; this indicates that the return signal strength

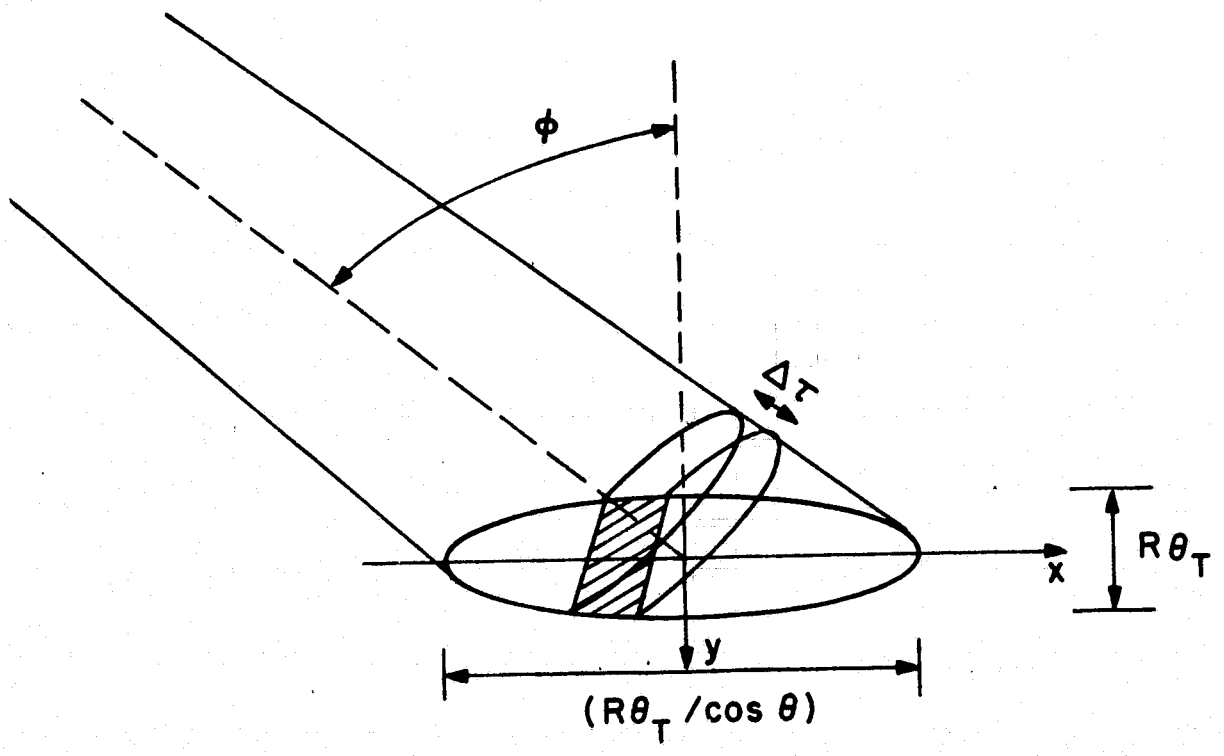

Figure 5-5. Geometry of the beam intersecting the ground.

stands out well from the background noise in a 5-nsec sampling interval. Even if the beam divergence is expanded by a factor of 10, to several milliradians, SNRC is still ∿100 at these off-zenith angles. At an orbital altitude of 1000 km, this ratio degrades by only a factor of 2.

With θ_T = 1.0 mrad, H = 500 km, and the above parameters, the average return signal strength at ϕ = 45° would be about 80 photoelectrons, and the total return from the surrounding area would be about one-fourth that, or about 20 photoelectrons. These noise photoelectrons, however, are spread over a range of 700 m (∿5 μsec). Even with ϕ as large as 60°, where the return signal strength would be about 10 photoelectrons, the total clutter signal is about 3 photoelectrons but spread over 1250 m (8.3 μsec), giving an average of only ∿0.015 photoelectron per 5-nsec sampling interval.

From all the above examples, we believe that the retroreflector returns can be discriminated on a shot-by-shot basis simply from the amplitude. Detection can be improved even further if necessary by averaging 8 to 12 pulses in each pointing.

5.4.2.2 Reflected sunlight

The effect of reflected sunlight can be determined by assuming that the earth is a Lambertian surface with a reflectance of ρ. Then the power density for reflected sunlight, P_s, received at the satellite is given by

$$P_s = \frac{P_0 \theta_T^2 T_0^2}{4} \cos^2 \phi_s \cos^2 \phi \quad , \tag{5-16}$$

where P_0 is the irradiance of the sun at the top of the atmosphere, θ_T is the angular field of view of the receiver (taken as equal to the transmitted beamwidth), and ϕ_s is the solar zenith angle to the target.

The most stringent condition for this background noise occurs when the sun is at zenith over the target; solar irradiation at the top of the atmosphere is about 0.20 w/cm^2 μm at 5300 Å and 0.12 w/cm^2 μm at 7000 Å. For a 0.5-mrad receiver beamwidth, $\phi = 0°$, and $T_{o0}^2 = 0.5$, the power density at the receiver will be about 1.5 photons/μsec cm^2 Å. For a 30-inch-diameter receiver with 1% efficiency (6943 Å), reflected sunlight produces about 250 photoelectrons/μsec, even with a 1 Å etalon filter. At the Nd^+ Yag wavelength, the situation would be about a factor of 3 worse owing to the enhanced detector efficiency. The return signal from the target, however, is about 2500 photoelectrons, which should be readily distinguishable by means of amplitude discrimination.

At $\phi = 60°$ and $\theta_T = 0.5$ mrad, the return from reflected solar radiation is about 60 photoelectrons/μsec, or about 0.3 photoelectron in a 5-nsec sampling interval. The expected return signal strength from the target is still fairly healthy, ∿40 photoelectrons. Expanding the beam to $\theta_T = 1.0$ mrad at $\phi = 60°$ will still give a SNRC of 10 for a 5-nsec sampling interval. If a higher orbital altitude (1000 km) were used, SNRC would drop to about 4, and some data averaging may be required.

5.4.2.3 Range noise versus signal strength

Range noise will be dependent on the laser pulse width, the return signal strength, and the characteristics of the detection system. If the laser pulse is gaussian and the detection-system risetime is fast compared to the output-pulse dimensions, then a perfect centroid detector would give a range noise of $\sigma \sim 0.4W/\sqrt{N}$, where W is the pulse width (half-power points) and N is the number of photoelectrons returned. This would hold for normal points when data aggregation is used.

If a laser with a 3- to 5-nsec pulse width is used with centroid detection, a total return signal strength of about 250 photoelectrons will be required to reduce the random noise due to pulse shape to about 2 cm. Once the system has acquired the target and is operating at $\theta_T = 0.5$ mrad, this should be nearly satisfied on a shot-by-shot basis at 45° or with an aggregation of 8 to 10 shots at 60°.

For the short-pulse lasers with 100- to 300-psec pulse widths, 2-cm range noise is satisfied even at the single-photoelectron level if a proper centroid-detection system can be built. In reality, a fixed or adaptive threshold would probably be used with these short pulses, and, depending on how the data are analyzed, 1 to 5 photoelectrons may be required.

5.4.3 Grid-point retroreflector array

The retroreflector arrays at the grid points must provide strong return signals up to zenith angles of 70°. The solid angle of reflection must be large enough to account for the velocity aberration due to the orbital motion of the satellite, and the range correction must be "correctable" to a simple reference point on the ground to within a few millimeters. The optical ground stations, or grid points, themselves must be completely passive and should not require attendance during a satellite pass. On the other hand, they must be serviced (i.e., washed or cleaned) regularly without resulting degradation and will need to be housed when necessary to avoid exposure to weather extremes such as wind storms and snow.

An individual cube corner, of the type used on Starlette, produces an effective cross section of about 10^5 m^2 at zenith, which falls off with zenith angle, going to zero at about 57°. Starlette's cube corners, which have a 33-mm-diameter circular aperture, have aluminum coating on their back surfaces to enhance the acceptance angle. According to signal-strength calculations, at least 6 to 10 such cubes will need to face the satellite at all times during operation. On the other hand, since the individual cube corners must be able to withstand environmental extremes of temperature, humidity, and atmospheric constituents without degradation, total internal reflection is called for, rather than silver- or aluminum-coated back surfaces, and this would reduce the acceptance angle to as low as 17° for some cube-corner orientations.

A flat array would have the advantages of simplicity. However, with a limited acceptance angle, a flat retroreflector array could be used only over portions of the orbital geometry; for wider coverage, the array would have to

be reoriented from pass to pass, as well as during a pass. The array orientation may have to be adjusted several times on a high-elevation satellite pass regardless of whether the cube corners have total internal reflection or are coated.

Cost factors aside, the most applicable geometry would be a spherical array, similar to Starlette's, with total-internal-reflection cubes. Starlette is a 24-cm-diameter sphere with 60 retroreflectors mounted nearly flush with the spherical surface. This array configuration provides an isotropic cross section and range corrections. The retroreflector spheres could be made out of aluminum and mounted on a small reference platform just above the ground. The disadvantages of a spherical array are the large number of cube corners required and the high cost of machining the spheres. By manufacturing in volume, however, costs could be reduced.

5.4.4 Satellite-borne systems

5.4.4.1 Satellite laser systems and photodetectors

Although a detailed discussion of the hardware components that would be involved in a Clogeos optical system is impossible in the context of this report, we wish to make a few comments on the system philosophy and hardware availability. The two possibilities for the pulsed laser system aboard the spacecraft are 1) a 3- to 5-nsec Q-switched laser with some type of pulse-processing system and 2) a mode-locked short-pulse (100 to 300 nsec) laser with a fast risetime detection system. Although neither is space qualified at the moment as far as we know, both are commercially available.

The 3- to 5-nsec Q-switched laser is available in both the ruby wavelength (6943 Å) and a doubled Nd^{+} Yag wavelength (5300 Å). The Yag system appears to be the more promising option since operating efficiencies are much higher and the shorter wavelength offers considerably enhanced detector efficiencies (10% versus 3%). Yag systems, already available from several vendors, produce 3- to 5-nsec pulses at energy levels in excess of 100 mJ with pulse-repetition rates of

5 to 10 pps. At this rate, the requirements for data averaging are satisfied, even at the lowest spacecraft altitude angles of interest, and the acquisition procedure could be carried out within the first 60 sec of a pass.

Both analog and digital (waveform-sampling) processing would have to be examined for application in the detection system. Pulse-center measurements with electronic integrators and adaptive threshold-triggering systems should give pulse-to-pulse range stabilities of better than a few tenths of a nanosecond. Waveform digitizing with intervals of 1 nsec or less should yield even better results. Measurements with the waveform digitizer of the NASA and SAO laser systems show pulse-to-pulse stabilities of less than 0.2 nsec for 3- to 5-nsec pulses.

A mode-locked Nd^{+} Yag laser system that produces well in excess of 100 mJ with a pulse-repetition rate of 10 pps or more is now commercially available; pulse widths of less than 300 psec are output at 5300 Å. At the moment, these lasers are very delicate and sensitive to the environment, but work is progressing rapidly to make them more rugged. At lower energies, considerably higher pulse-repetition rates have been obtained.

The detection system for the mode-locked laser needs to consist of only a fast-risetime static cross-field photomultiplier and an adaptive threshold discriminator. Added accuracy can be derived from range corrections for pulse amplitude.

Both types of lasers are now being employed in satellite ranging programs from the ground.

5.4.4.2 Pointing accuracy and acquisition

Laser ranging from the ground relies on precise satellite ephemerides for laser pointing. Satellite predictions accurate to 1 arcmin and better are now generated by several groups.

In this program, the situation will be more complicated, however. The vehicle that will carry the equipment, perhaps the Space Shuttle or Space Lab, may be in a fairly low orbit (500 n.mi.), and the complex shape of the spacecraft will present large unmodeled errors in the orbit owing to atmospheric drag and radiation pressure. In addition, we expect that venting, outgassing, and other activity aboard the spacecraft will also corrupt the orbit. From our experience with Skylab, we can anticipate orbital position errors as large as several hundred meters at the end of a 72-hour prediction period, which could account for pointing errors of 2 to 3 arcmin.

A second source of pointing error is the uncertainty with which the laser system can be pointed relative to inertial space. This is basically the error in spacecraft-attitude reference. Typically, stabilized platforms can be pointed to ±5 mrad relative to inertial space, and we anticipate that this source of error will dominate the laser-pointing error. With the minimum 10-mrad beam required to overcome the pointing problem, the signal-to-noise ratio at zenith would be far below 1. At sufficiently off-zenith angles, however, where the signal-to-noise ratio is proportional to $1/\theta_T$, we would still get an SNR of ∿50 for 5-nsec sampling intervals at a range of 1000 km.

The problem, therefore, becomes one of signal strength. With a 10-mrad beam, the return signal strength will be only a few photoelectrons even at zenith for the 500-km-altitude case examined earlier. There are a number of ways to improve this situation. Although the pointing from the space platform may be in error by as much as 5 mrad, short-term stability should be considerably better. This would permit the use of a search mode with a much narrower beam. A 10-mrad x 10-mrad matrix could be covered by a hundred laser pulses with θ_T = 1 mrad, which would give return signals of about 10 photoelectrons at $\phi = 60°$. It may then be practical to employ a sequential scanning system that uses several beamwidths to get down to 0.3 to 0.5 mrad, enhancing the signal strength even more. At the 1000-km orbital altitude, we would be at the single-photoelectron level for $\phi = 60°$ and θ_T = 1 mrad, and some pulse averaging would be necessary.

Substantial signal enhancement can be derived from pulse averaging if we consider the fact that the photoelectrons returning from the background clutter are randomly distributed in time during the "clutter interval," whereas those returning from the cube corners are fixed in time (corrected for the ephemeris). Thus, if we average over many pulses, the returns from the retroreflector should reinforce each other and those from the clutter should average out to a background baseline signal. Section 5.4.2.1 described the theory of clutter discrimination by means of range gating.

5.4.4.3 Operating strategies and data averaging

In this application, the interstation baselines will probably be determined in a differential mode, with either a geometric or a translocation-type analysis. Observations would be made on an array of cube corners in a time short enough to use the satellite orbit as a short-arc interpolation device. The orbit itself can be maintained by either ground or satellite-to-satellite tracking of the spacecraft or by satellite tracking of an array of reference ground stations.

There are a number of possible strategies that can be used, depending on the tracking systems available and the array being measured. The scheme that places the most stringent constraints on the time available for data acquisition is a system whereby the on-board ranging machine must be time-shared between "orbit reference" cube corners and those at ground measurement points.

Examination of 5-cm-quality range data from Goddard Space Flight Center indicates that with a 700-km-altitude orbit (such as that for satellite BE-C), orbital accuracy can be maintained to approximately the quality of the data for data points at least 60 to 120 sec apart. This can be seen from the residuals to short arcs developed from points selected from full data sets. If we devote 15 sec to acquisition and data taking on each cube corner, six cubes could be included in each cycle: one or two for orbital maintenance and the remainder for ground positions. The 15 sec per target would permit 120 to 140 shots for

acquisition and 10 to 15 for data averaging. In this mode of operation, 30 to 40 individual range measurements could be made during a typical 10-min pass, with 20 to 30 measurements being on ground-positioning targets.

The number of data points can be increased significantly if two or more independently steered channels can be operated simultaneously. Alternatively, the pulse-repetition rate of the laser (and the system) could be increased with some reduction in output power. The signal is sufficiently high in most cases that some tradeoffs are possible. Some improvement in data acquisition can also be achieved by using alternative independent tracking techniques.

5.4.4.4 Timing

Since the data will be analyzed in the differential mode, the only real requirements are short-term stability during a pass and long-term epochs accurate enough to support pointing predictions. During a sequence of (short-arc) measurements, the satellite epoch reference must remain stable to less than 1 μsec. On the average, a 1-μsec error will introduce a shift of about 4 mm in station position.

The long-term epoch accuracy must be sufficient to keep the retroreflector within the 10-arcmin "search area." Since the pointing accuracy of the laser itself will be the dominant source of error here, the timing requirement will not be very stringent. A timing accuracy of 20 to 50 msec should be sufficient to keep the influence due to timing errors small.

6. CONCLUSIONS AND RECOMMENDATIONS

It is apparent from the content of the preceding sections that we cannot come to definitive conclusions regarding the feasibility of the Clogeos concept. Certain preliminary conclusions, however, as well as recommendations for future study and experimentation, can be made at this time.

A primary conclusion is that the basic goal of 1-cm accuracy for the location of the Clogeos grid elements does not appear to be hardware-limited. That is, at least two types of systems — the radio doppler and the optical-pulse radar — can, at the current state of the art or in the very near future, provide the resolution and repeatability required for the 1-cm Clogeos network. A third approach, the microwave-modulated optical doppler system, is very promising but does not appear to be at the same advanced state of development that the other two systems are.

This optimistic appraisal must be tempered by the realization that the grid-point elements, though much simpler and cheaper than tracking stations, cannot be merely cube-corner reflectors scattered from a helicopter. The radio doppler system requires active electronics and a source of power, while the optical system calls for retroreflector arrays. Any of these devices must be precisely positioned and very carefully emplaced to avoid spurious motion. It is difficult to estimate the volume cost of the radio transponders or retroreflector arrays, but figures of $1,000 to $2,000 per unit in 1976 dollars appear to be reasonable. Placement costs, for labor and transportation, will vary according to the weather, terrain, and local labor and cannot be reliably predicted at this time.

As is abundantly clear from Sections 3 and 4 and Appendix A, tropospheric transmissivity and refractivity are the primary problem areas in implementing a 1-cm Clogeos grid. Optical systems, either doppler or pulse, are strongly affected by scattering mechanisms in the atmosphere (clouds, haze, and aerosols). In certain areas of interest, such as southern Alaska, overcast skies (greater

than 70% obscured) can be expected 60 to 75% of the hours of the year, severely limiting the applicability of optical interrogation.

It should be noted here that inverted systems such as Clogeos differ in one important respect from Lageos and other satellite-tracking systems. For the purpose of determining satellite orbits, the ground tracking stations can be sited in meteorologically desirable locations: in desert areas or on mountain tops. No such choice is available to the Clogeos-system designer; the grid must be located in the area to be surveyed, regardless of the climatic conditions obtaining.

In contrast to the optical systems, the radio doppler system is reasonably well suited to all-weather operation, but atmospheric refractivity errors are on the order of 20 cm to 2 m, approximately 10 times the clear-air refractivity error expected at optical wavelengths.

The second major conclusion arising from this study, therefore, is that knowledge of atmospheric influences on both radio and optical polarization is simply insufficient to proceed with the design of a 1-cm Clogeos system. No systematic, long-term, and global-propagation data base exists on which a system design can be predicated. It appears that multiple-wavelength optical systems can provide the range or range-rate accuracies required, but the question of scattering and cloud cover remains. Overconstrained grids offer an approach to the design of radio systems (and optical systems as well) that might overcome the atmospheric refraction problem, but a great deal of modeling, analysis, and experimentation is necessary before such a system could be deployed with confidence.

At the present time, our state of knowledge of the effects of the atmosphere on electromagnetic wave propagation lags sadly behind the rapid progress of hardware techniques for both the radio and the optical regimes. A recent National Science Foundation conference (McIntyre and Kerr, 1977) reemphasized the basic limitations imposed on optical communications by atmospheric scattering, concluding that "... the poor understanding of atmospheric effects makes it difficult to assess the impact of improvements in device and system technology on communication system performance."

The conference participants proposed the development of mobile field facilities for optical propagation measurements. However, similar facilities used in the past have not provided data that would be relevant to the problem of satellite-to-ground communications in essentially vertical propagation paths. SAO proposed a satellite-based propagation experiment that has the potential of providing a broad sampling of propagation data on a worldwide basis (see Appendix B). The experiment envisions a spacecraft-borne receiving terminal operating at three optical wavelengths, 0.48, 0.63, and 10.6 μ, and three microwave wavelengths, 20, 13.6, and 1.87 cm. The three optical carriers provide sufficient information to solve for the average refractive index, for a dry atmosphere, of the transmission path between the satellite and the ground terminal. A small correction, on the order of 0.5 cm, is necessary to allow for the variable water-vapor content of the atmosphere. This correction can be estimated from an additional measurement taken at one of the three microwave frequencies.

For convenience of measurement, the optical uplink carriers are each modulated at 500 MHz. The phase of the modulation can then be compared readily to the phase of a microwave carrier after the appropriate frequency conversions. The phase difference among the six channels is a measure of the relative time delay at each wavelength and therefore a direct measurement of the average refractive index of the transmission path at each wavelength. Because only one-way transmission paths are involved, the received signal strengths at the satellites are relatively high, and simple, straight-forward detection systems can be employed. The ground transmitting stations can be made to be easily transportable, and data can be collected at any location along the ground track of the satellite. Figure 6-1 shows a block diagram of the overall experiment system.

The experiment as described in the proposal can easily be modified to incorporate continuous monitoring of the optical carrier intensity. This measurement will provide valuable data on fading statistics and transmission reliability as a function of locale and weather conditions.

On a more immediate basis, SAO recommends a geodetic error analysis incorporating the cloud-cover statistics outlined in Section 3. Preliminary error studies

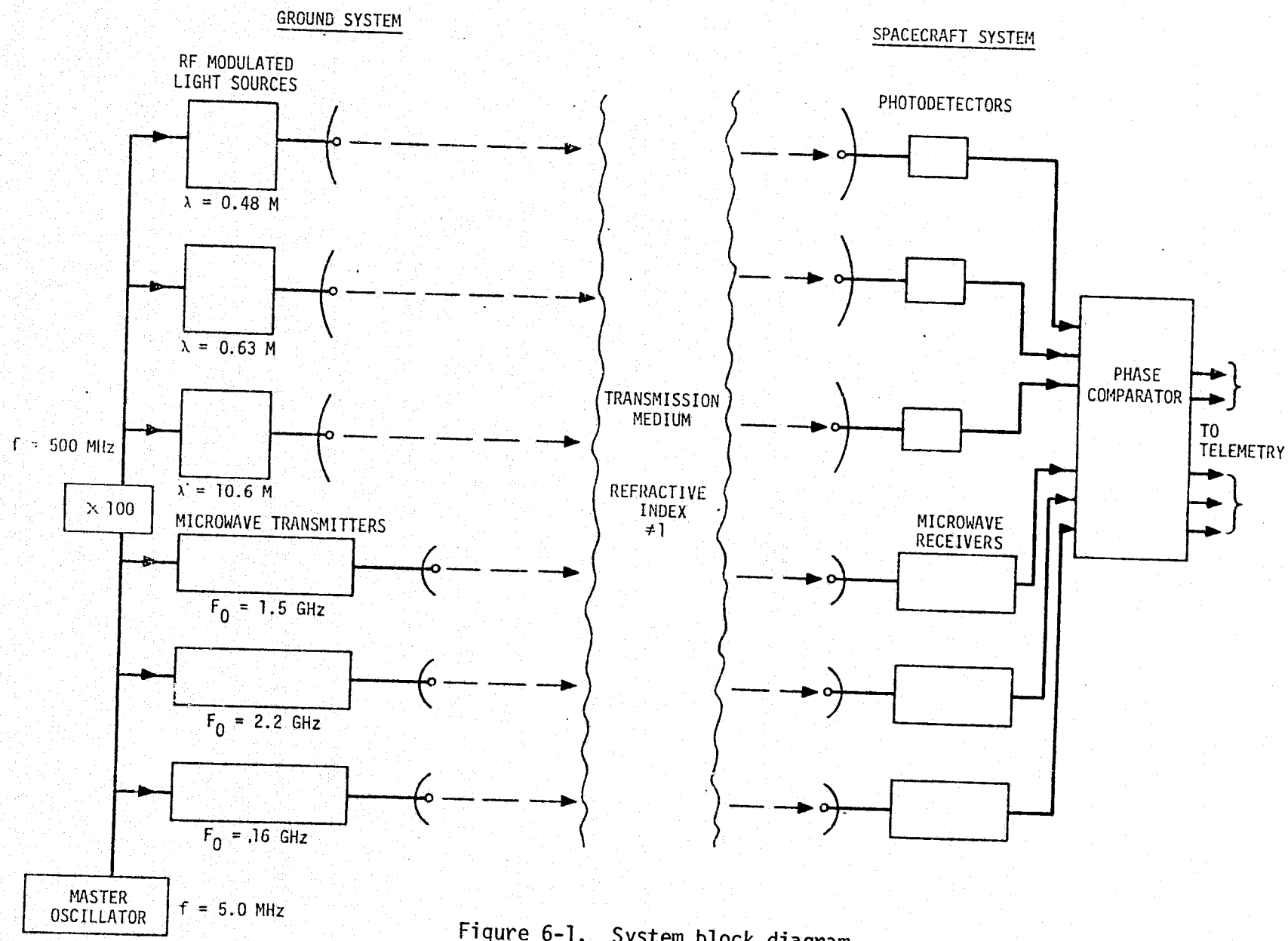

Figure 6-1. System block diagram.

(I. Mueller, private communication, 1975) at Ohio State University show that the position uncertainties converge quite slowly with increasing data. It is important to determine the feasibility of optical ranging or range-rate systems in the presence of clouds or other scatterers that may limit the data rate or cause loss of data entirely for relatively long periods. The convergence of the grid terminal positions under these conditions may be too slow to permit the operation of a practical Clogeos system.

7. REFERENCES

Bean, B. R., 1961, Concerning the Bi-exponential nature of the tropospheric refractive index. Beitrage zur Phys. der Atmos., Bd. 34, pp. 81-91.

Bean, B. R., and Dutton, E. J., 1966, Radio Meteorology. NBS Mono. 92, Washington, D.C., 435 pp.

Bean, B. R., and Horn, J. D., 1961, On the average atmospheric radio refractive index structure over North America. Beitrage zur Phys. der Atmos., Bd. 34, pp. 92-104.

Bean, B. R., and Thayer, G. D., 1958, A model radio refractivity atmosphere. NBS Rep. 5576, Boulder, Colorado, 89 pp.

Bouricius, G. M. B., and Earnshaw, K. B., 1974, Results of field testing a two-wavelength optical distance-measuring instrument. Journ. Geophys. Res., vol. 79, pp. 3015-3018.

Bucher, E. A., Lerner, R. M., and Niessen, C. W., 1970, Some experiments on the propagation of light pulses through clouds. Proc. IEEE, vol. 58, pp. 1564-1567.

Crane, R. K., 1964, Ray-tracings in cloud cross sections for a long baseline interferometer. In Proceedings of the Third Tropospheric Refraction Effects Meeting, vol. I, Results and Status of Tropospheric Effects Measurement Programs, ed. by L. J. Galbiati, Tech. Doc. Rep. No. ESD-TDR-64-148, pp. 57-87.

Cunningham, R. M., 1964, Scale and type of atmospheric refractive index anomalies. In Proceedings of the Third Tropospheric Refraction Effects Meeting, vol. I, Results and Status of Tropospheric Effects Measurement Programs, ed. by L. J. Galbiati, Tech. Doc. Rep. No. ESD-TDR-64-148, pp. 33-41.

Earnshaw, K. B., and Hernandez, E. N., 1972, Two-laser optical distance-measuring instrument that corrects for the atmospheric index of refraction. Appl. Opt., vol. 11, pp. 749-754.

Edlén, B., 1966, The refractive index of air. Metrologia, vol. 2, pp. 71-80.

Erickson, K. E., 1962, Investigation of the invariance of atmospheric dispersion with a long-path refractometer. Journ. Opt. Soc. Amer., vol. 52, pp. 777-780.

Gay, R. H., and Grossi, M. D., 1975, Doppler measurements of the ionosphere on the occasion of the Apollo-Soyuz Test Project. Part II: Inversion of differential and rotating doppler shifts. Smithsonian Astrophys. Obs. Spec. Rep. No. 367, 37 pp.

Grantz, A., 1971, The San Fernando, California, earthquake of February 9, 1971. Geol. Survey Prof. Paper 733, U.S. Geological Survey and National Oceanic and Atmospheric Administration.

Grossi, M. D., and Gay, R. H., 1975, Doppler measurements of the ionosphere on the occasion of the Apollo-Soyuz Test Project. Part I: Computer simulation of ionospheric-induced doppler shifts. Smithsonian Astrophys. Obs. Spec. Rep. No. 366, 54 pp. plus appendix.

Guier, W. H., and Weiffenbach, G. C., 1960, A satellite doppler navigation system. Proc. IRE, vol. 48, pp. 507-516.

Hopfield, H. S., 1963, The effect of tropospheric refraction on the doppler shift of a satellite signal. Journ. Geophys. Res., vol. 68, pp. 5157-5168.

Hopfield, H. S., 1969, Two quartic tropospheric refractivity profile for correcting satellite data. Journ. Geophys. Res., vol. 74, pp. 4487-4499.

Hopfield, H. S., 1970, Tropospheric effect on electromagnetically measured range: Prediction from surface weather data. Johns Hopkins Univ. Rep. TG-1119, 39 pp., July.

McIntyre, C. M., and Kerr, J. R., 1977, Communications without fibers. Laser Focus, vol. 13, no. 4, pp. 46-49.

National Academy of Sciences, 1973, U.S. Program for the Geodynamics Project, Scope and Objectives.

Owens, J. C., and Earnshaw, K. B., 1968, Development of a microwave modulated, dual optical wavelength geodetic distance-measuring instrument. ESSA Tech. Rep. ERL 117-WPL 8, U.S. Dept. of Commerce, Boulder, Colorado, 108 pp., September.

Savage, J. C., Prescott, W. H., and Kinoshita, W. T., 1973, Geodimeter measurements along the San Andreas Fault. In Proceedings of the Conference on Tectonic Problems of the San Andreas Fault System, Stanford Univ. Press, Stanford, California, pp. 44-53.

Scholz, C. H., Sykes, L. R., and Aggarwal, Y. P., 1973, Earthquake prediction: A physical basis. Science, vol. 181, pp. 803-810.

Sherr, P. E., Glaser, A. H., Barnes, J. C., and Willand, J. H., 1968, World-wide cloud cover distributions for use in computer simulations. NASA CR-61226, 140 pp. plus appendices.

Skolnik, M. I., 1962, Introduction to Radar Systems. McGraw-Hill Book Co., New York, 648 pp.

Thayer, G. D., 1967, Atmospheric effects on multiple-frequency range measurements. ESSA Tech. Rep. IER 56-ITSA 53, 57 pp. plus appendix, October.

Wilson, R. W., 1970, Attenuation on an earth-space path measured in the wavelength range of 8 to 14 micrometers. Science, vol. 168, pp. 1456-1457.

APPENDIX A

SUMMARY OF A CONFERENCE ON TROPOSPHERIC TRANSMISSION EFFECTS

The Geoastronomy Division of the Center for Astrophysics hosted a 2-day conference in June 1975 to discuss the effects resulting from the propagation of radio and optical signals through the troposphere. The basic purpose was to discern both whether the refractive index of the troposphere can actually be estimated and, if so, corrected for and whether such refraction errors are homogeneous over short baselines. Such knowledge would have a direct bearing on two ground-to-space ranging systems that the Smithsonian Astrophysical Observatory (SAO) has been studying. It was hoped that the conference would make recommendations that would enable a ranging system to achieve a residual error of 1 cm for elevation angles of 20° to 90°.

Participants at the conference were Helen Hopfield, Applied Physics Laboratory, Johns Hopkins University; Robert Lawrence, Wave Propagation Laboratory, National Oceanic and Atmospheric Administration; Robert Crane, Lincoln Laboratory; Duane Haugen, Air Force Cambridge Research Laboratory; and George C. Weiffenbach, Martin W. Levine, Mario D. Grossi, Ashok Gupta, and Richard Brown, SAO. The discussion itself was both informal and wide ranging, making an actual outline of the presentation difficult. The following summarizes the possibilities discussed and the major recommendations and conclusions made.

A.1 Background

SAO is currently investigating two ground-to-space ranging systems that have geophysical and geodetic applications, both of which require information on tropospheric refraction. The first study is to upgrade SAO's existing worldwide network of laser tracking stations to an absolute range accuracy of 1 to 2 cm. Using short-pulse, high-peak-power ruby lasers, the system determines

slant range by measuring the go-return time from the ground to retroreflectors mounted on medium-altitude satellites such as Lageos. One of the major contributions to the current error budget of the range measurement is the refractive index of the troposphere. It is essential, therefore, to determine the magnitude of this error and its variability with time, weather conditions, and geographic location. Furthermore, from our knowledge of surface meterological conditions, can we then correct for this error?

The second study concerns a proposed satellite-to-earth radio (or optical) ranging system wherein active components are on board a spacecraft and passive retroreflectors (or transponders) are on the ground. Such a system would be used to determine the deformation of a grid of control points over a limited area on the earth's surface; typical baselines between adjacent control points might be on the order of 5 to 10 km, with a length on the order of 100 to 200 km. The purpose is to be able to recognize a 1- to 2-cm change in the grid configuration over a 3-month sampling interval. The extent to which tropospheric refraction errors are homogeneous over the short baselines proposed is the key to the success of a system of this type. The horizontal gradients of the dry and wet components of tropospheric refractivity, anomalous radio refractivity through or near cloud masses, and again, the degree to which the propagation errors can be estimated from surface meteorological data are all of primary concern.

Both of these programs are intended to operate at low data rates and will depend on averaging many satellite passes to obtain overall system accuracies. Therefore, measurements taken during known or suspected periods of tropospheric instability, such as the passage of a front, can be excluded, as can those taken at very low elevation angles, less than 15°. Operation of the systems will be restricted to land-based ground stations and, particularly for the short-baseline project, to areas of high seismic activity, such as the California fault zones, Nevada, and the southern coast of Alaska.

A.2 Meteorology as Applied to the Troposphere

In general, the participants felt that the meteorologist can offer little or no help to the system designer in achieving the 1-cm requirement for satellite-to-ground ranging accuracies. Meteorological conditions on the whole are too complex, too rapidly changing, and too poorly estimated by surface measurements to be factored directly into an operating system. Upper air measurements, either by means of radiosonde balloons or instrumented aircraft, cannot provide an instantaneous "snapshot" of the troposphere; at best, the meteorologist can construct model tropospheres that are essentially composites of the possible tropospheric conditions at a particular location, which, of course, vary considerably over different geographic locations. Furthermore, current weather-measurement techniques are not precise enough. The spatial and temporal variations of such significant factors as humidity and horizontal N gradients are difficult to measure and analyze synoptically in different geographic areas. For example, large horizontal N gradients may give rise to relative range errors as high as 10 cm, and the patterns of these variations vary for different elevation angles. Crane showed a sample curve of this error for zenith angles of 0° and 70°, obtained from Mistram experiments. He also suggested that N may change by one unit owing to rain and by 20 units owing to clouds. All participants largely agreed with Crane that from models based on meteorological parameters, only the error bound and the statistical properties of the troposphere can be studied, and these may not be relevant for our applications.

Barometric-pressure measurements at the surface seem to be the only meteorological data of possible value in correcting for range errors. Surface pressure provides a direct measure of the total tropospheric content above the observation point. It had been proposed that range errors could thus be corrected to an accuracy of 1 cm or better. The pressure correction is derived from integrating the hydrostatic equation and the equation of state for the column of air immediately above the observer. Radiosonde balloons measure barometric pressure and ambient temperature, and the altitude of the balloon is calculated by application of the hydrostatic equation. But it appears that neither

radiosonde nor rawinsonde observations would help correct for optical or radio measurements over slant paths through the troposphere. The consensus of the meeting was that radiosonde observations would not contribute information of value to the program and that SAO should not engage in any campaign of meteorological observations in the field, including radiosonde flights or mesoscale surface-pressure-measurement networks. Although the usefulness of such a simple measure of the integrated refractivity is apparent, the reliability of the correction and its application at elevation angles less than 90° have not been determined.

Questions were raised by the participants as to whether the range error for the dry term can be determined by surface pressure alone, since surface pressure does not necessarily reflect synoptic changes in the troposphere. As wind velocity also affects surface-pressure measurements, Haugen claims that this relation can be used on the average with an error within 0.1% for the dry component; for zenith angles, this error amounts to $\sim$3 mm. The consensus of the conference was that the dry component of the integrated tropospheric refractivity can be estimated from barometric-pressure measurements for a zenith ray to an accuracy of between 0.01 and 0.1% (0.2 to 2.0 mm for typical tropospheric conditions). It was suggested that the data from an array of pressure sensors located throughout a grid of ground stations could serve as a useful supplement to the redundant data obtained from an overconstrained network, described in the next section. This appears to be particularly possible for situations in which slowly varying pressure gradients in both time and position blanket the grid. The conferees pointed out that the pressure-measurement concept has very definite limitations: In particular, because internal waves are present within the troposphere, the pressure correction cannot be extended to nonvertical propagation paths. Furthermore, this correction applies only to the dry component of the refractivity and is useful only in the optical regime. Even at optical wavelengths, a small error, on the order of 3.0 mm, is attributable to fluctuations of the wet component, and a still smaller temperature-dependent error is caused by the contribution of the water-vapor partial pressure to the measured total pressure.

Haugen suggested that a carefully planned, long-term mesoscale surface-pressure measurement program in the San Andreas fault zone could possibly be of some value, although small-scale dynamic effects produced by boundary interactions are not necessarily reflected throughout the depth of the atmosphere and would best be filtered out.

It seems that although the constraints on achieving the desired accuracy in the range error are imposed by the troposphere, the problem itself should be categorized as a wave-propagation problem rather than as a meteorological one. It was generally agreed that meteorological data are so poorly correlated with the results of propagation studies that the only reliable way to obtain tropospheric-error data is to perform properly designed experiments that measure the errors directly. In other words, system designers should try to "correct" the meteorology of the troposphere, rather than "incorporate" it.

A.3 Multiple-Wavelength Systems

Because of uncertainties in the meteorological parameters and their measurements, it was recommended that high-accuracy ranging systems be "self-correcting," that is, that they be inherently independent of the state of the atmosphere. The errors introduced by horizontal N gradients, for example, would no longer be factors.

Multiple-wavelength systems, such as the Wave Propagation Laboratory's two-color optical instrument, fall into the self-correcting category. Their two-color laser range finder can measure distances along a 6- to 7-km ground-to-ground path with a root-mean-square precision on the order of 0.05 cm over periods of up to 6 months. Lawrence called attention to the fact that the types of errors that arise from this system are instrumental, dispersion, and wet term. The consensus was that this system has the potential of achieving the desired specifications for a high-accuracy ranging system. Using a two-wavelength optical technique will not necessarily double the complexity or bulk of the hardware; for example, beam splitting and frequency doubling enable two wavelengths

to be emitted from a single laser. The major problem with this method would be obtaining the required high-frequency modulation.

Similar radio systems, also self-correcting, could be devised, but they might present even more difficult technical problems because of the very low dispersion in the vicinity of the water-vapor lines — about 0.01 N units, compared to 15 to 20 N units across the visible spectrum. Highly sensitive instrumentation might therefore be required. Also, a radio approach does not obviate cloud problems, because of the relatively large refractive-index changes associated with the high water content of cumulus clouds. The refractivity of the interior of a cloud can exceed that of the clear atmosphere by 10 to 30 N units; for example, a 1-km-deep cloud layer could cause a range error of 1 to 3 cm. Even greater errors have been attributed to the large gradients of refractivity at the edges of clouds, with recorded instances of multipathing resulting from ray bending at the perimeter of sharply defined cloud masses. It was mentioned that if lasers are used for radio-frequency systems, continuous-wave lasers should be employed rather than pulsed ones. Pulsed lasers currently in use at Goddard Space Flight Center have 2-cm residual errors due to the instrument alone, together with a 13-psec jitter in pulse duration.

The possibility of using only one optical frequency was briefly discussed. Although it might appear that a one-frequency optical system would be better than a radio system because of the smaller contribution of the wet term, it was felt that it would be very difficult to calibrate such a system. Errors due to atmospheric refraction may be small, but orbital perturbations pose a serious problem. No particular recommendation was made either for or against such a system; however, if a satellite experiment using dual optical frequencies should be performed, data for the individual frequencies can be analyzed separately.

The system that generated the most discussion was a crossed-integration scheme, or overconstrained network, suggested by Lawrence. An alternative, or

perhaps an adjunct, to a self-correcting system, this method utilizes surface-pressure measurements, indicative of the integrated range error in the vertical, and oblique apparent range measurements via satellite to determine the true range to ground targets. Range measurements would be made to a large number of closely spaced stations from a satellite as it moves from horizon to horizon. If the troposphere is represented by the excess optical path length without regard to the tropospheric composition, it appears possible to extract both the grid geometry and the optical path length from the data. It is, of course, necessary to separate range differences due to crustal motion from those caused by the troposphere. Slow, uniform plate motions with time constants on the order of months should not be difficult to separate spectrally from tropospheric fluctuations; however, rapid changes in ground-station position associated with earthquakes could be a problem. Experimental results exhibited at the conference demonstrated that the power spectral density of tropospheric refractivity measured at radio frequencies extends to frequencies as low as 1 cycle per 10^6 sec.

The meeting concluded with a brief discussion of radiometric techniques for probing the line of sight between a satellite and a ground station. In general, the feeling was one of pessimism about the applicability of radiometric measurements because of the difficulty of calibrating the instruments absolutely, the sensitivity of the radiometer to the temperature profile of the line of sight, and the presence of background radiation in the case of satellite-to-ground measurements.

A.4 Conclusions and Recommendations

Given a system requirement for satellite-to-ground ranging accuracies on the order of 1 cm, the participants generally agreed that no technique nor technology for dealing with tropospheric-refractivity errors exists that can guarantee this performance level at the present state of the art. There are, of course, a number of promising approaches, but each of these requires further analysis and experimentation before general applicability can be proved. Furthermore,

there was agreement on the paths that should be taken toward the design of a high-accuracy ranging system and those that should be avoided.

The consensus of the meeting appeared to favor measurements in the optical rather than the radio range because of the large (30 cm) and rather unpredictable range-error fluctuation contributed by atmospheric water vapor. However, it was pointed out that either the self-correcting or the redundant measurement system would work at radio frequencies, although with greater technical difficulties owing to the small dispersions in the first case and the larger total errors in the second.

The use of two optical frequencies seems desirable because wide geographic and seasonal variations can be covered synoptically. However, for areas with a high frequency of cloud cover, such as Alaska, radio systems might be better; this suggestion is, of course, highly debatable, as discussed above. In the long run, regardless of whether radio or optical means are used, the distribution of clouds, both geographically and seasonally, must be considered.

Recommendations for further work were two-fold, coinciding in time. The first was that an experiment (satellite- or possibly aircraft-borne) be designed and flown to test the obtainable satellite-to-ground ranging accuracy by means of a multiple-wavelength, self-correcting system. It is hoped that tropospheric effects on the measurement vehicle could thus be evaluated and a baseline for future tests established. However, the high precision demonstrated by such systems over short ranges on the surface is not directly transferable to the much greater path length and rate of change of path length associated with satellite-to-ground measurements.

The second major recommendation was that a series of typical and extreme digital models of the troposphere be constructed from existing data and known tropospheric physics to test various approaches to the measurement technique. The models should be reasonably fine grained, with details of internal waves and horizontal gradients included down to scale sizes approaching the distance

between ground stations (3 to 6 km). The model would be used to determine the bounds of the propagation error under a variety of conditions and at various locations on the earth's surface. Combined with a model of the ground-station array and of expected crustal motion, the entire redundant measurement system could be exercised. The integrated model would be particularly useful for determining the extent to which crustal motions can be distinguished from atmospheric fluctuations by means of filtering in the frequency domain. This statistical-modeling study is desirable not as a means of solving the problem, but as a means of understanding the problem in more detail and determining the bounds of the errors involved.

APPENDIX B

ATMOSPHERIC-REFRACTIVITY EXPERIMENT

DATE: November 7, 1975
Proposal P 579-11-75

EXPERIMENT SUMMARY
ADVANCED APPLICATIONS FLIGHT EXPERIMENT

EXPERIMENT TITLE: Atmospheric-Refractivity Experiment

PRINCIPAL INVESTIGATOR: Dr. Martin W. Levine, Smithsonian Astrophysical Observatory, Cambridge, Massachusetts, 02138. Tel. (617) 495-7274.

DESCRIPTION AND PURPOSE OF EXPERIMENT: To measure directly, from ground stations to a satellite, range and range-rate errors caused by variations in the refractivity of the earth's atmosphere. To provide data to enable the design and operation of satellite-borne systems to measure distances and altitudes, and their variations, to an accuracy on the order of 1.0 cm, the accuracy level required for support of the Earth and Ocean Dynamics Applications Program in such areas as earthquake hazard assessment, plate tectonics, subsidence studies, and crustal motion.

EXPERIMENT TECHNIQUES: Transmit six frequencies simultaneously from the ground station to the receiving terminal in the satellite. Measure the electrical path-length differences at the transmitted frequencies by means of phase differences between the carriers (or the modulation envelopes of the carriers). Telemeter the phase-difference signals to the ground station and process them. Compute the line integral of the refractivity over the transmission path for each frequency from the phase-difference signals.

APPARATUS: A set of ground transmitters and satellite-borne receivers to measure the difference in the time of flight of electromagnetic radiation at different frequencies over a given transmission path to determine the total path-length error at each frequency. The instrument exploits known dispersive characteristics of various components of the atmospheric refractive index to estimate the absolute value of the range error at each transmitted frequency.

MEASUREMENT PARAMETERS: The phase difference between one carrier frequency, designated as the master, and that of each of five other frequencies as received at the satellite terminal, using transmission wavelengths of 0.48 μ, 0.63 μ, 10.6 μ, 20 cm, 13.6 cm, and 1.87 cm.

PRIOR DEVELOPMENT: Multiple-frequency distance-measurement equipment and line-integral refractometers have been developed and tested over short terrestial paths, and the feasibility of apparatus of this type has been well established. No previous SR & T development has been undertaken.

PROPOSED DEVELOPMENT: Fabrication of an engineering model of the proposed payload and a breadboard model of the associated ground equipment. The engineering-model payload will be used for tests over surface transmission paths in a variety of climatological conditions; no aircraft nor balloon flight tests are anticipated.

DISCIPLINE: Support of the Earth and Ocean Dynamics Applications Program.

POTENTIAL MISSION: The Application Explorer Mission, in an approximately circular polar orbit at an altitude on the order of 800 km, is a suitable spacecraft for the proposed experiment.

PROPOSAL TO

NATIONAL AERONAUTICS AND SPACE ADMINISTRATION

FOR PARTICIPATION IN THE

ADVANCED APPLICATIONS FLIGHT EXPERIMENT

Atmospheric-Refractivity Experiment

Proposal P 579-11-75

For the period 1 July 1976 to 31 December 1978

Principal Investigator

Dr. Martin W. Levine
Physicist

Associate Director for Geoastronomy

Dr. George C. Weiffenbach

November 1975

Smithsonian Institution
Astrophysical Observatory
Cambridge, Massachusetts 02138

Director: Dr. George B. Field

Assistant Director: Mr. John G. Gregory

The Smithsonian Astrophysical Observatory
and the Harvard College Observatory
are members of the
Center for Astrophysics

TABLE OF CONTENTS

ABSTRACT

Satellite-borne systems to measure ground-station positions and the variations in these quantities on the earth's surface with accuracies of 1.0 cm or less are required for a wide range of tasks in support of the Earth and Ocean Dynamics Applications Program. The accuracy capability of these ranging systems is limited, not by instrumentation, but by variations in the refractive index of the earth's atmosphere that cause commensurate changes in the electrical path length between the satellite and the ground.

The proposed program is an experiment to measure directly the propagation path errors at optical, infrared, and microwave frequencies in order to provide 1) much-needed design information for future earth-sensing systems, 2) a data base for the construction of a model of the refractivity structure of the atmosphere for the prediction and correction of propagation errors, and 3) basic meteorological data for microscale and mesoscale studies of the earth's atmosphere.

The basic experimental technique is the measurement of received phase differences between signals transmitted over six different communications links from a ground station to a space-borne receiving terminal. The proposed transmission wavelengths are 0.48 and 0.63 μ in the visible, 10.6 μ in the infrared, and 20, 13.6, and 1.87 cm in the microwave spectrum.

PROPOSAL TO
NATIONAL AERONAUTICS AND SPACE ADMINISTRATION
FOR PARTICIPATION IN THE
ADVANCED APPLICATIONS FLIGHT EXPERIMENT

Atmospheric-Refractivity Experiment

Proposal P 579-11-75

1. INTRODUCTION

The Smithsonian Astrophysical Observatory (SAO) proposes to obtain information on atmospheric refractivity at both radio and optical wavelengths that can be used to evaluate and improve existing algorithms for propagation-error correction.

Atmospheric-propagation errors are a fundamental limitation on the accuracies that can be obtained in all present geodetic measurements, both for satellite systems and for surface-to-surface techniques. The requirements are very stringent in programs such as the Earth and Ocean Dynamics Applications Program (EODAP) of the National Aeronautics and Space Administration (NASA), where accuracies of 1 to 2 cm are desired. Algorithms to correct for atmospheric-propagation effects in satellite systems have been developed that are particularly convenient and practical because they require as inputs only measurements of surface barometric pressure, temperature, and humidity. However, no data are currently available to make a satisfactory assessment at the centimeter level of the accuracy of this approach. It is the purpose of this experiment to provide such data.

It is essential that EODAP programs function over wide geographic areas and over extended periods of time. Indeed, this is one of the great strengths of satellite systems. For this same reason, the proposed experiment is most naturally suited for implementation by satellite. This is the only practical means to make observations that are adequately synoptic both geographically and in time.

2. EXPERIMENT APPLICATIONS

2.1 Electromagnetic Wave Propagation in the Atmosphere

2.1.1 Introduction

All current high-accuracy geodetic methods are based on the measured time of flight or (equivalently) the measured wavelength of an electromagnetic signal, be it optical or radio, pulsed or continuous. In all cases, it is necessary to know the propagation velocity in order to obtain the desired parameter — viz., range or range-rate — from the observed time intervals that constitute the raw data.

The neutral earth's atmosphere reduces the effective propagation velocity of electromagnetic waves, with the result that the measured propagation times are longer than would be the case in vacuum. The magnitude of the apparent change in range caused by this phenomenon is roughly 2½ m for a vertical path through the entire atmosphere for both optical and radio signals. Obviously, this reduction in propagation velocity will cause errors in the desired geodetic parameters if we do not correct for the effect.

The index of refraction n of a medium is defined as

$$n = \frac{c}{v} \quad ,$$

where c is the vacuum velocity of propagation of an electromagnetic signal and v is its propagation velocity in the medium. The vacuum velocity is very accurately the same for all wavelengths of interest from radio to optical, but n varies with both wavelength and the medium.

The velocity of propagation v is the time derivative of S, the distance traversed,

$$v = \frac{dS}{dt} = \frac{c}{n}$$

or

$$c\, dt = n\, dS \quad .$$

For convenience, the refractivity N is defined as

$$N = (n - 1) \times 10^6 \cong 300.$$

Therefore,

$$c\,dt = (N \times 10^{-6} + 1)\,dS.$$

In making a distance measurement, one observes the elapsed time $\tau = \int dt$, so that

$$S = c\tau - 10^{-6}\int N\,dS \quad .$$

The refractivity N along the propagation path must be known to obtain the correct geometric distance S. Determining N(S) is the essence of the tropospheric-propagation problem.

2.1.2 Optical Refractivity

The refractivity of the atmosphere at radio and optical wavelengths has been measured in the laboratory as a function of temperature, pressure, and atmospheric composition. The results in the optical case are particularly accurate. The best values are those of Owens (1967). Owens' simplified formula for the group refractive index for air of standard composition with 0.03% CO_2 is more than adequate for our present purpose. This is his equation (42), which, with a change in notation and with some of the smaller terms dropped, is

$$N = f(\lambda)D + g(\lambda)D_w \quad ,$$

where $f(\lambda)$ and $g(\lambda)$ are functions of wavelength only:

$$f(\lambda) = 23.7134 + 6839.397\,\frac{(130+\sigma^2)}{(130-\sigma^2)^2} + 45.473\,\frac{(38.9+\sigma^2)}{(38.9-\sigma^2)^2} \quad ,$$

$$g(\lambda) = 64.8731 + 1.74174\,\sigma^2 - 0.035575\,\sigma^4 + 0.0061957\,\sigma^6 \quad ,$$

where σ is the wave number in microns^{-1}. The dispersion functions $f(\lambda)$ and $g(\lambda)$, plotted in Figure 1, are the basis for determining atmospheric refractivity from measurements at two optical wavelengths. D is a function of the partial pressure P_d (in mbar) of dry air and absolute temperature T, and D_w is a function of the partial pressure e of water vapor and T, viz.,

$$D = \frac{P_d}{T}\left[1 + P_d\left(57.90\times 10^{-8} - \frac{9.3250\times 10^{-4}}{T} + \frac{0.25844}{T^2}\right)\right] \quad ,$$

$$D_w \cong \frac{e}{T} \quad .$$

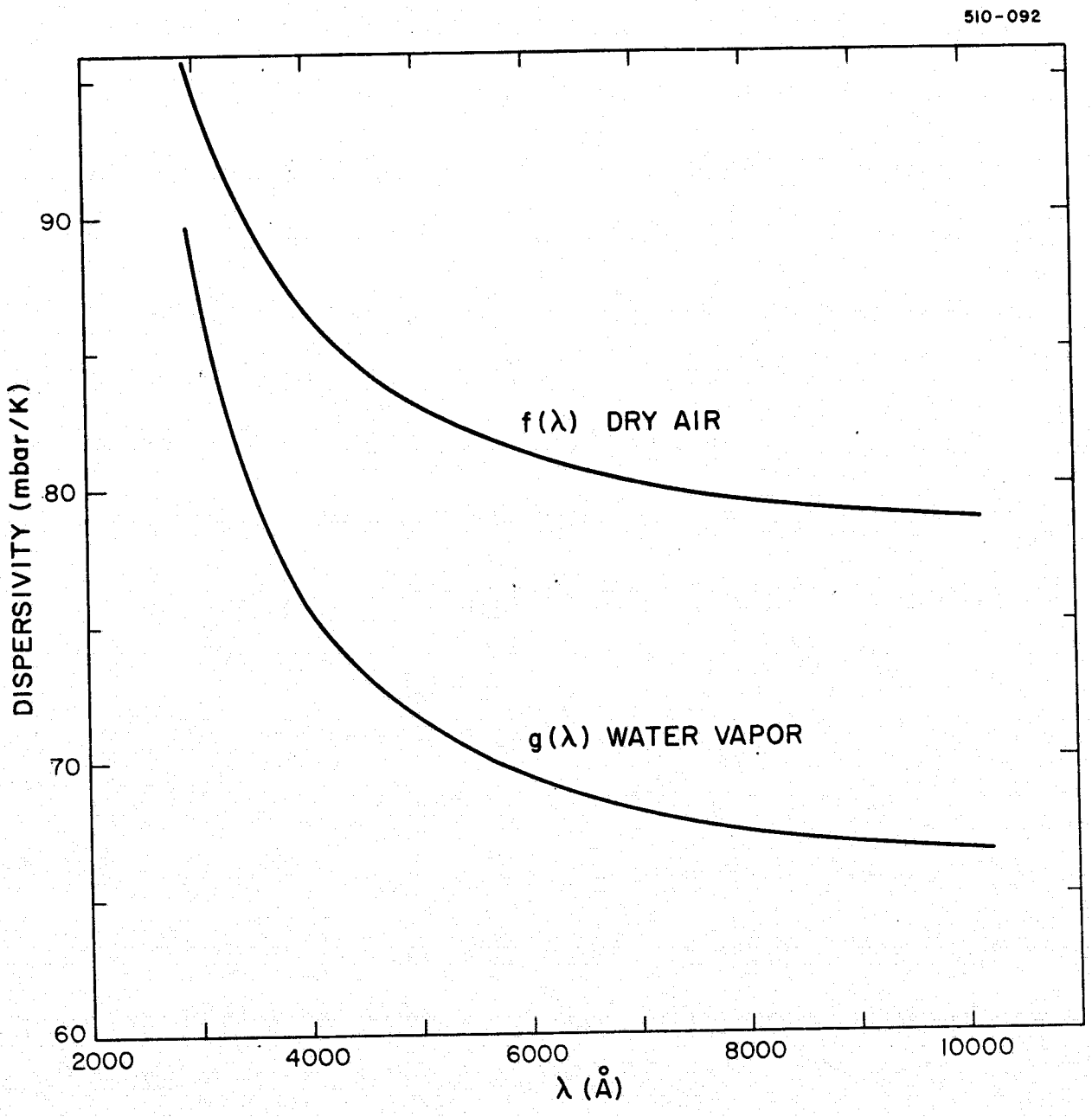

Figure 1. Optical dispersion functions for dry air and water vapor.

For a ruby laser with $\lambda = 0.6942\ \mu$,

$$N = 80.286\,D + 68.39\,D_w \quad .$$

In terms of the total pressure,

$$P = P_d + e \quad ,$$

$$N = 80.286\,\frac{P}{T} - 11.9\,\frac{e}{T} + \delta \quad , \tag{1}$$

where δ is a small correction term,

$$\delta = 80.29\,\frac{(P-e)^2}{T}\left[57.9\times 10^{-8} - \frac{9.325\times 10^{-4}}{T} + \frac{0.25844}{T^2}\right] \quad .$$

2.1.3 Radio-Frequency Refractivity

Corresponding formulas for radio frequencies have been derived. The radio-frequency refractivity of air (Bean and Dutton, 1966) is given by

$$N = (n-1)\times 10^6 = K_1\left(\frac{P_d}{T}\right) + K_2\left(\frac{e}{T}\right) + K_3\left(\frac{e}{T^2}\right) \quad .$$

The constants K_1, K_2, and K_3 are related to the molecular weights of the respective constituents. For dry air, K_1 has been computed by assuming the air to have the so-called standard composition (Bean and Dutton, 1966), including 0.03% CO_2. These constants have the following values:

$$K_1 = 77.607 \pm 0.13 \text{ K mbar}^{-1}$$

$$K_2 = 71.6 \pm 8.5 \text{ K mbar}^{-1}$$

$$K_3 = (3.747 \pm 0.031) \times 10^5 \text{ (K)}^2 \text{ mbar}^{-1} \quad .$$

If P (= P_d + e) is the total pressure of moist air, then equation (1) can be written as

$$N = 77.6\left(\frac{P}{T}\right) - 5.6\left(\frac{e}{T}\right) + 3.75\times 10^5\left(\frac{e}{T^2}\right) \quad , \tag{2}$$

which can be simplified to (Smith and Weintraub, 1953)

$$N = 77.6\left(\frac{P}{T}\right) + 3.73\times 10^5\left(\frac{e}{T^2}\right) \quad . \tag{3}$$

This yields values of N within 0.02% of those obtained by equation (2) for the temperature range of -50 to 40°C.

Some typical values of N at various temperatures (for fixed pressure and relative humidity) are given in Table 1. To show the weak dependence of N versus frequency, the refractivities of water vapor, dry air, and oxygen are given in Table 2 for frequencies of 9, 24, and 72 GHz. Thus, it would be very difficult to get information on N by using atmospheric dispersion at radio wavelengths, in contrast to the optical case.

Table 1. Determination of N from meteorological measurements, assuming no error in the equation of N.

Source	-50°C	0°C	+15°C	+40°C
Smith and Weintraub equation (1)	352.61	306.18	318.79	419.55

Table 2. Refractivities of water vapor and dry gases (dry gases at 0°C, 760 mm Hg; water vapor at 20°C, 10 mm Hg).

Gas	9 GHz	24 GHz	72 GHz
Water vapor	60.7 ± 0.20	60.7 ± 0.20	61.0 ± 0.2
Dry air	288.1 ± 0.10	288.15± 0.10	287.66± 0.11
Oxygen	266.2 ± 0.2	266.4 ± 0.2	263.9 ± 0.2

On the other hand, the contribution of atmospheric water vapor to N is much larger at radio than at optical wavelengths. In fact the ratio of the coefficients of e in equations (1) and (3) is

$$\frac{N_w^{RF}}{N_w^{opt}} \cong \frac{3 \times 10^4}{T} ,$$

so the dependence of N on water vapor is some 2 orders of magnitude greater at radio frequencies than in the optical.

Thus, comparison of radio and optical propagation can provide a measure of water-vapor content along the propagation path.

2.1.4 Tropospheric-Refractivity Correction Algorithm

A significant factor to be noted in equations (1) and (3) is that the dominant term in each case has the form

$$N = k\frac{P}{T} \quad .$$

Based on this relationship, a particularly useful method of obtaining tropospheric-propagation corrections has been developed by Hopfield (1970). Assuming the atmosphere is in hydrostatic equilibrium, the surface pressure P_S is given by

$$P_S = \int_S^\infty \rho(h)\, g(h)\, dh \quad ,$$

where h is the altitude, $\rho(h)$ is the atmospheric density at h, and $g(h)$ is the gravity acceleration at h. Assuming that the air is of standard composition and that it follows the ideal gas law,

$$\frac{P}{T} = R\rho \quad ,$$

where R is the gas constant for air. Noting that

$$N \tilde{=} k\frac{P}{T} \tilde{=} k\, R\rho \quad ,$$

$$\int N\, dh = k \int R(h)\, \rho(h)\, dh \quad .$$

If $R(h)$ = constant = R and $g(h)$ = constant = g, then

$$\int_S^\infty N\, dh = k\, R \int \rho(h)\, dh = k\, R\, \frac{P_S}{g} \quad . \qquad (4)$$

This result states that the atmospheric-propagation correction for a vertical propagation path — the integral on the left side of equation (4) — can be calculated from three parameters (k, R, and g) that are known a priori and a single observable (P_S), the barometric pressure at the ground station. This can be understood in terms of two facts. The influence of the atmosphere on propagation velocity is proportional to the total quantity of air along the propagation path, and the surface pressure "weighs" the total quantity of air above the ground station.

If this relationship is sufficiently accurate, it is of enormous importance because it would remove the need for determining meteorological parameters at every point along each and every propagation path and would permit the calculation of

correction factors from the one atmospheric parameter that can easily be measured with high accuracy.

The relationship defined in equation (4) has been tested through comparison with a very large body of measured height profiles (radiosonde balloons) of the atmosphere. The data cover many geographic locations, several years, all times of year, and daytime and nighttime. The results of this comparison indicate the following:

A. At optical wavelengths, propagation corrections based on equation (4) for zenith propagation paths always have errors less than 1 cm.

B. At radio frequencies, propagation corrections for the dry component of the atmosphere can be determined to essentially the same accuracy as in the optical case.

C. At radio frequencies, propagation corrections for the wet component of the atmosphere cannot be calculated accurately from the kind of algorithm implied by equation (4).

There are several problems in using this comparison to assess the accuracy of the algorithm. First, it is to some extent a self-consistency test, because the same instruments obtain both the surface data used in the algorithm and the height profile data used in the numerical integration. Second, the radiosonde instrumentation is not accurate enough. The humidity measurement, which is particularly important in the radio-frequency regime, is especially poor.

In actual fact, it is not at all feasible to make sufficiently detailed and accurate meteorological measurements over a large enough region of the atmosphere that one could accurately reconstruct atmospheric refractivity for precise satellite observations.

2.2 Experiment Description

2.2.1 General

The proposed experiment differs from some earlier approaches in that only a single dependent variable, and the only one of interest for geodetic satellite systems — that is, the integrated refractivity over the propagation path and its time derivative — is measured and modeled. Previous experiments relied on measurements of meteorological parameters, which were then converted to refractive-index variations, from which range errors were computed. These studies were less than completely successful, because of the practical problems involved in obtaining real-time measurements of the state of the atmosphere over the distances in ground-to-satellite transmission paths.

The proposed satellite system is to measure the integral of the refractivity in the visible spectrum (0.35 to 0.7 μ) and the microwave spectrum (3 to 100 cm).

Two additional regions of the spectrum, the infrared at 10.6 μ and the millimeter wave in the vicinity of the water-vapor resonance at 22 GHz, are proposed for study. Although these two wavelengths are particularly interesting from both a

scientific and an operational viewpoint, technical problems at the present state of the art cast some doubt on the feasibility of their being included in the proposed experiment.

The proposed experiment is not a prototype for an operational system. Rather, it is an experiment designed to provide basic data to support future operational systems in the areas of high-precision geodesy, geodetics, earth physics, tracking, and navigation.

The experiment is designed to measure directly those range and rate-rate errors introduced into ground-to-satellite links by atmospheric and ionospheric refractivity. The basic concept is to determine precisely ground-to-satellite path-length differentials at six transmission frequencies: three in the microwave portion of the spectrum (1.5, 2.2, and 16 GHz), one in the infrared (10.6 μ), and two in the visible (0.48 and 0.63 μ). Absolute range to the satellite is not required; all we need are the differences in measured range between one of the transmission channels, designated as the reference channel, and each of the five others.

2.2.2 Experiment Strategy

The operating frequencies must be selected to enhance our ability to distinguish among the following:

A. Dry component of the atmosphere. This component is essentially nondispersive at radio frequencies but exhibits moderate dispersion in the visible (Edlén, 1953). The refractivity varies from approximately 315 N units at 3500 Å to 285 N units at 6500 Å (see Figure 1). It is this dispersive quality that enables the dry-component contribution to be estimated by simultaneous range measurements at two or more visible wavelengths. This property has been very successfully exploited by the Wave Propagation Laboratory (WPL) of the National Oceanic and Atmospheric Administration in their Two-Wavelength Distance-Measuring Instrument, with which they achieved a resolution of the order of 1 mm (Earnshaw and Hernandez, 1972).

B. Wet component of the atmosphere. The total range error caused by precipitable water vapor in the atmosphere is highly variable in the radio regime, with an error contribution between 0 and 30 cm. No measurable dispersion occurs outside the water-vapor absorption lines at 15 and 30 GHz. The wet-component contribution in the visible portion of the spectrum is small, approximately 5 mm, for vertical transmission through the entire atmosphere.

C. Ionosphere. The ionospheric range error is highly dispersive at radio frequencies, with the refractive index varying as $1/f^2$. The range-error contribution, for normal ionospheric conditions, is on the order of 2 m at 1.6 GHz. The ionospheric error is negligible for the infrared and visible wavelengths. The dispersion property can be used very effectively to estimate the ionospheric contribution by simultaneous range measurements at two or more frequencies, by means of a technique analogous to that described in A above.

It is possible to solve for each of these three components by operating four ranging channels simultaneously, two in the visible and two in the radio regime (Thayer, 1967). The dispersive nature of the dry component in the visible portion of the spectrum permits a relatively simple approach to the estimation of its contribution. Both visible channels, one at the blue end of the spectrum and the other at the red, are amplitude modulated at the same radio frequency. The two

wavelengths are transmitted over a common path and detected by photomultipliers at the receiving terminal; the phase angle between the RF outputs of the two photodetectors is then measured. The phase angle between the two demodulated RF signals is a measure of the difference of the line integrals of the group refractivity at the two wavelengths over the transmission path. As noted in Section 2.1.2 above, the group refractivity of the atmosphere for the visible spectrum is accurately known from laboratory measurements (Owens and Earnshaw, 1968), so the major uncertainty in this measurement is the variability of the atmospheric composition, chiefly water vapor.

In a similar fashion, the received carrier phase angles of the two RF channels can be compared to determine the ionospheric component. For unmodulated RF carriers, we must use the phase velocity, rather than the group velocity used for the modulated visible-light measurements. For the frequencies in this experiment, the refractive index of the ionosphere is (Jackson, 1962)

$$n_I \cong 1 - \frac{1}{2}\frac{f_N^2}{f^2} \quad , \tag{5}$$

where f is the carrier frequency and f_N the plasma frequency; $f_N \cong (81\ N)^{\frac{1}{2}}$, where N is the electron density in electrons per cubic meter.

The measurements described above yield two range estimates, one at RF corrected for the ionosphere and a second for visible wavelengths corrected for the dry component of the atmosphere. If ΔR_{opt} is the residual range error as measured in the optical regime and ΔR_{RF} the same quantity determined at RF, then

$$\Delta R_{opt} = \Delta R_{d,opt} + \Delta R_{w,opt} \quad , \tag{6}$$

$$\Delta R_{RF} = \Delta R_{d,RF} + \Delta R_{w,RF} + \Delta R_{ion} \quad , \tag{7}$$

where ΔR_d is the range error attributable to the dry component, $\Delta R_{w,opt}$ and $\Delta R_{w,RF}$ are due to the wet components at optical and radio frequencies, respectively, and ΔR_{ion} is caused by the ionosphere.

In equations (6) and (7), ΔR_{opt} and ΔR_{RF} are measured, $\Delta R_{d,opt}$ is determined from the known dispersion between the two optical measurements, $\Delta R_{d,RF}$ can be calculated from the known relationship between it and $\Delta R_{d,opt}$, and ΔR_{ion} is calculated from the known dispersion between the two radio-frequency carriers.

Since the water-vapor refractivity contribution is highly dispersive between the optical and the radio frequencies, equations (6) and (7) can be solved for both $\Delta R_{w,RF}$ and $\Delta R_{w,opt}$. The optical wet component is approximately 5 mm under typical atmospheric conditions, so a first-order correction based on the range difference $\Delta R_{RF} - R_{opt}$ is adequate to obtain an overall error of less than 1.0 mm.

Only four of the six transmission frequencies, two each in the visible and the UHF range, are used to determine the geometric range to the satellite from the ground station. The other two, one in the infrared at 10.6 μ and one in the millimeter range at approximately 16 GHz, are included to provide propagation information for spectral regimes that are becoming increasingly important for communications and radar. In particular, very little is known about the refractive index of the atmosphere in the 10-μ region of the spectrum. The 16-GHz frequency was selected because it lies near the peak of a water-vapor absorption line. The dispersion caused by this absorption line is small, on the order of 0.1 N unit, but is detectable by the proposed system.

2.2.3 Experimental System Configuration

The experiment system is comprised of one or more ground stations, each transmitting at six frequencies to the satellite. A command link from the ground to the satellite is required, as is a real-time telemetry link for experiment data.

The block diagram in Figure 2 shows the three modulated optical transmission channels, the three radio-frequency channels, and the command and telemetry provisions. As illustrated, the system will operate with one ground station at a time. Simultaneous interrogation by two or more ground stations would require additional receiving equipment, phase comparators, and telemetry channels. In this section, a simple system with one ground station will be discussed; extensions to the system required for multiplexing two or more stations will be described in Section 2.5.

Atmospheric and ionospheric refractivity causes changes in propagation velocity, which appear as phase changes in the received signals. In Figure 2, the 0.48-μ (blue) channel is shown as the reference. The uplink light beam is modulated at frequency f_m. The phase of the demodulated RF signal at the output of the photomultiplier receiver in the satellite is

$$\Theta_B = \frac{2\pi n_{gb}(t)\, R(t)\, f_m}{c} \quad , \tag{8}$$

where n_{gb} is the group index of refraction at the wavelength of 0.48 μ averaged over the entire path, R is the range from transmitter to receiver, and c is the vacuum velocity of light. Note that both n_{gb} and R are functions of time. Frequency is defined as the derivative of phase; the time rate of change of R(t) is the origin of the doppler shift. The time rate of change of the averaged refractive index, n_{gb}, is also a frequency shift and is indistinguishable, at a single measurement frequency, from a geometric doppler shift.

Similarly, the phase of the RF signal at the output of the photomultiplier receiver of the red channel is

$$\Theta_R = \frac{2\pi n_{gr}(t)\, R(t)\, f_m}{c} + \Theta_D \quad , \tag{9}$$

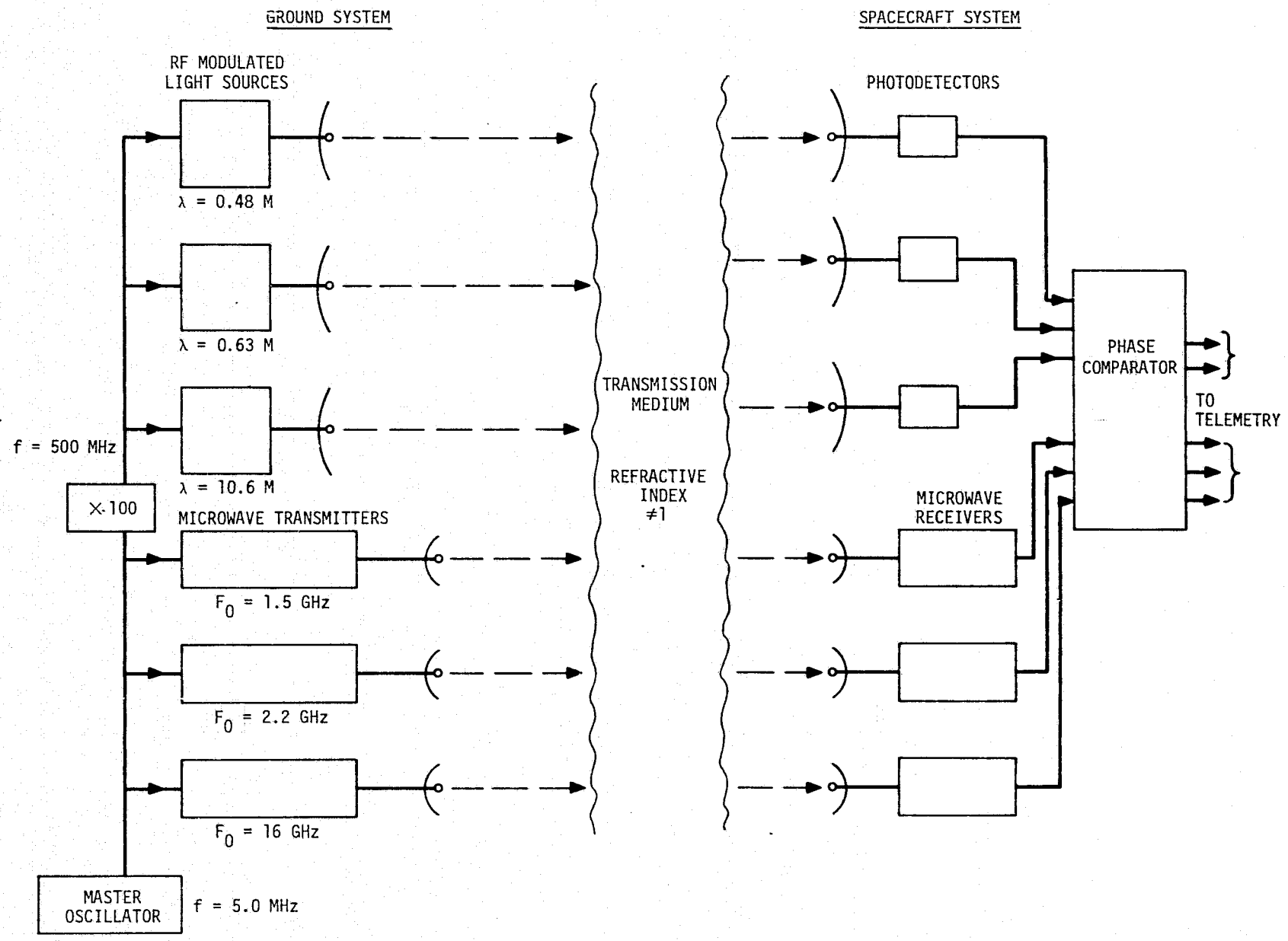

Figure 2. System block diagram.

where n_{gr} is the group index of refraction at the 0.63-μ wavelength averaged over the entire path and Θ_D is a constant representing the optical-path-length difference between the two channels.

The difference between the phases of the red and the blue channels, as measured by an on-board phase detector, is the crucial data output of the proposed experiment. The phase difference, which can be written in terms of N units as

$$\Delta\Theta = \frac{2\pi R(t)\, f_m}{c} (N_{gr} - N_{gb}) + \Theta_D \quad , \tag{10}$$

is a direct measure of the apparent range difference caused by refractive-index variations at two different optical wavelengths.

The quantity $\Delta\Theta$ is a very useful observable for several reasons. First, it is a range difference, and thus, most of the doppler shift normally associated with satellite-tracking signals does not appear at the output of the phase comparator. The telemetry bandwidth required for the phase-difference signal does not exceed 5 Hz. In comparison, the radio frequency at the photomultiplier output will vary by about ± 10 kHz for a typical satellite pass.

Second, and of greater importance, the range error between either the red- or blue-channel measurement and the geometric range can easily be extracted from the phase-difference signal. The phase difference between the blue channel and an ideal transmission path with a refractive index of unity is

$$\Delta\Theta \left(\frac{N_{gb}}{N_{gb} - N_{gr}} \right) = \frac{2\pi R(t)\, f_m}{c} N_{gb}$$

$$= \frac{2\pi R(t)\, f_m}{c} (n_{gb} - 1) \quad . \tag{11}$$

The term $N_{gb}/(N_{gb} - N_{gr})$, the ratio of refractivities at two wavelengths, is independent of density and is a function only of the transmission wavelengths for a dry atmosphere. The ratio is known to a high degree of accuracy from both theory and supporting laboratory measurements (see Section 2.1). A small correction, on the order of 0.5 cm, is necessary for the variable water-vapor content of the atmosphere. This correction can be estimated to the degree of accuracy required for the proposed experiment from an additional measurement taken at microwave frequencies, as described in Section 2.3.3.

The RF output of the blue receiver photomultiplier serves as the phase reference for the remaining optical link at 10.6 μ and the three microwave links, as shown in Figure 2. The operation of each of the four additional phase comparisons is very similar in principle to that described above; in each case, only the phase-difference signals are telemetered to the ground station.

The RF modulation on the blue channel serves as the reference for a frequency synthesizer, which provides the necessary local-oscillator and phase-comparator signals for the microwave receivers. The receiver configuration will be discussed in greater detail in Section 2.3, but it is important to note here that the phase-difference outputs of the receiver phase comparators are referenced to the respective carrier frequencies and not to the optical-link modulation frequency. The output of the receiver phase comparators is of the form

$$\Delta\Theta = \frac{2\pi R(t)\, f_c}{c} (N_{RF} - N_{gb}) + \Theta_D \quad ,$$

where f_c is the microwave-link carrier frequency, N_{RF} is the phase refractivity, including both atmospheric and ionospheric effects, and Θ_D is a constant reflecting the fixed path difference between the blue optical link and the microwave link.

2.3 Spacecraft Electronic Systems

2.3.1 General

The spacecraft experiment systems are shown in block-diagram form in Figure 3. Described more fully in the following sections, the major systems are outlined briefly here:

A. Optical receiving system. This system consists of two photomultiplier tubes (one each for the red and the blue channels), an infrared photodetector, optical bandpass filters for the three optical links, amplifiers for the nominal 500-MHz modulation frequency, two phase comparators, and a phase-lock loop for the receiving system for the three optical uplinks.

B. Microwave receiving system. Three multiple-conversion receivers with synthesizers to generate the required local-oscillator frequencies comprise the basic elements of the microwave receiving system. The three phase comparators are shown in Figure 3 as discrete elements for clarity, but in the hardware, they are integral to the receivers.

C. Receiving optics. The term "optics" refers to the receiving antennas for all transmission frequencies, optical through microwave. Because of the stringent requirements for constancy of path length, the optics must be designed as a unit. The phase centers of the antennas must maintain fixed relationships, or at least predictable ones, independent of how the spacecraft is oriented with respect to the ground station.

D. Telemetry. The five phase-difference outputs constitute the experiment data. Since no on-board signal processing is required, the difference signals are telemetered directly, in analog form, to the ground station.

E. Command. A minimum of command functions is required for the spacecraft experiment systems. There are, of course, the commands associated with spacecraft pointing and aspect; in addition, the reference uplink can be selected and the spacecraft 100-MHz master oscillator tuned by ground command.

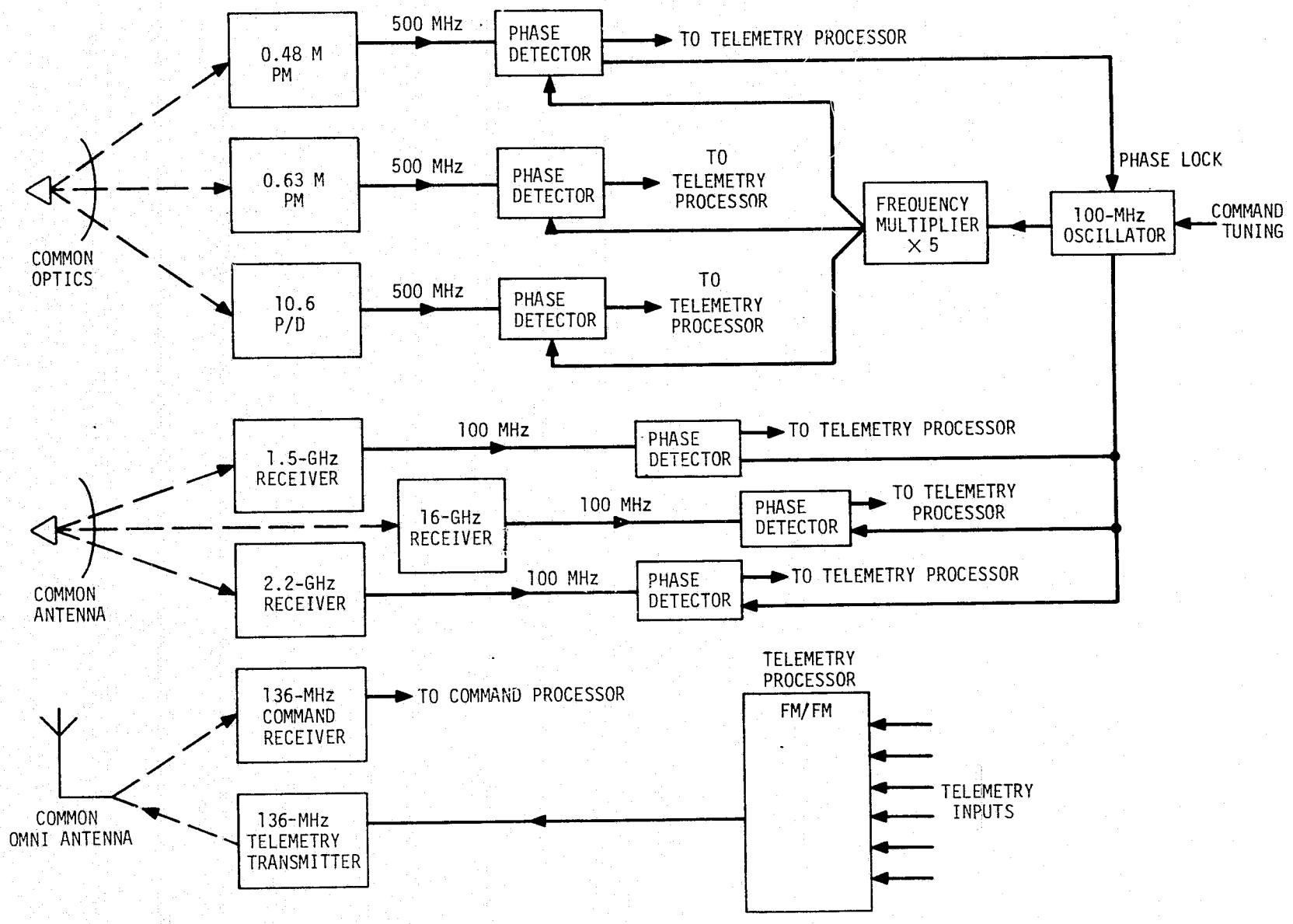

Figure 3. Spacecraft electronics.

2.3.2 Optical Receiving System

2.3.2.1 Blue channel

The 0.48-μ receiver is drawn at the top of Figure 3. For simplicity, the phase-lock loop for the spacecraft 100-MHz master oscillator is shown in this figure to be under the control of this uplink; control can be switched to any of the other uplinks by ground command.

The detector is a high-speed photomultiplier with an S-20 photocathode surface (ITT type F4034 or equivalent). In front of the photocathode is a conventionally designed interference filter with a half-power bandwidth of approximately 20 Å. It is anticipated that this bandwidth will be sufficient to avoid the necessity for on-board tuning equipment to compensate for ambient-temperature fluctuations or aging.

The 500-MHz modulation envelope is taken from the photomultiplier anode and then filtered, amplified, hard-limited, and applied to one input of the phase comparator. The reference input is furnished by a X5 multiplier from the 100-MHz voltage-controlled crystal oscillator. The DC-coupled output of the phase comparator is integrated by an operational amplifier and fed to the electronic frequency-control input of the oscillator. The phase-lock loop bandwidth, approximately 500 Hz at threshold, rises to about 2000 Hz for strong signals.

Once the loop is locked to the uplink modulation frequency, the master oscillator will track those phase variations of the signal caused by geometric range variations and refractive-index changes. Since the doppler shift is on the order of ±10 kHz at 500 MHz for a typical satellite pass, the voltage-controlled crystal oscillator must have a tuning range of at least ± 2 kHz at 100 MHz. The 500-MHz output of the frequency multiplier is distributed to the 0.63- and 10.6-μ channels as reference signals for the phase comparators. The 100-MHz output from the crystal oscillator is buffered and distributed to each of the three microwave receivers, where it is used as the reference for synthesizing the local-oscillator frequencies.

Two auxiliary functions are not illustrated in Figure 3. A quadrature phase detector provides a phase-lock indication, which is telemetered to the ground station. The amplitude of its output is a measure of the received signal strength. This detector also controls the operation of the lock-acquisition circuitry, which, in the absence of a lock indication, periodically sweeps the voltage-controlled crystal oscillator over a predetermined frequency range. The acquisition circuit is disabled when the quadrature phase detector indicates that phase lock has been achieved. The voltage-controlled crystal oscillator can also be tuned by command from the ground station to facilitate acquisition.

2.3.2.2 Red channel

The 0.63-μ receiver is identical in form to the 0.48-μ receiver described in the previous section. The blue-sensitive photomultiplier is replaced by a high-speed type with a GaAs photocathode (RCA type C31025 or equivalent), and the blue filter, by an appropriate red filter with a half-power bandwidth of approximately 30 Å.

The 500-MHz modulation signal at the output of the photomultiplier is processed in the same fashion as is the RF signal in the blue channel and is applied

to one input of the phase comparator. The reference input is the 500-MHz output of the frequency multiplier. The DC-coupled output of the phase comparator, the phase-difference signal, is filtered through a 5-Hz low-pass filter and then amplified and routed to the telemetry processor.

2.3.2.3 Infrared channel

The operation of the 10.6-μ receiver is identical in principle to that of the red (0.63-μ) one. However, at the present state of the art, the infrared photodetector is a possible problem area.

Efficient, high-speed photodiodes have been fabricated from HgCdTe; these appear to be satisfactory for the proposed experiment in every respect except one: they must be cooled to temperatures of 100 K or less (Melchior, Fisher, and Arams, 1970). Of the variety of cooling systems — open loop, closed loop, and passive — that have been designed for spacecraft applications (National Aeronautics and Space Administration, 1973), only the passive type seems to be suitable for the proposed mission duration. Unfortunately, however, passive coolers are generally better suited to geostationary or sun-synchronous orbits than to the medium-altitude polar orbit proposed herein.

The cooling problem and the design of a low-noise 500-MHz postamplifier are specific tasks in the statement of work. In any event, it should be reemphasized that the infrared investigation is only a secondary objective.

2.3.3 Microwave Receiving System

The three microwave receivers are similar in design, their obvious variations providing for the differing carrier frequencies. Only the receiver for the 1.5-GHz uplink, shown in the simplified block diagram in Figure 4, will be discussed in detail here.

The input carrier is amplified by a broad-band low-noise transistor amplifier and mixed with a 1400-MHz local-oscillator signal. The 100-MHz output of the mixer is further amplified and filtered and then utilized as one input to the phase detector. The first local-oscillator frequency is generated by a synthesizer, with the 100-MHz output of the spacecraft master oscillator, which is locked to the modulation frequency of the blue channel, as the reference. In this simplified example, the synthesizer is a X14 frequency multiplier; in general, the carrier frequency will not be a multiple of 100 MHz, and the synthesizer will be a somewhat more complex device. The second local-oscillator frequency (or phase-detector reference) is the output of the master oscillator at 100 MHz. The phase-detector output is band-limited, filtered, and used as an input to the telemetry processor.

As noted earlier, any one of the microwave receivers can be selected by ground command to phase lock the spacecraft master oscillator. In this case, the phase-detector output is electronically integrated, as shown in Figure 4, and routed through the selector switch to the electronic frequency control input of the voltage-controlled crystal oscillator. The lock bandwidth must be made wider to accommodate the doppler shift on the microwave carriers, which is larger than that on the lower-frequency RF modulation signals. The quadrature phase detector and the acquisition circuitry are essentially identical to those described in Section 2.3.2.1.

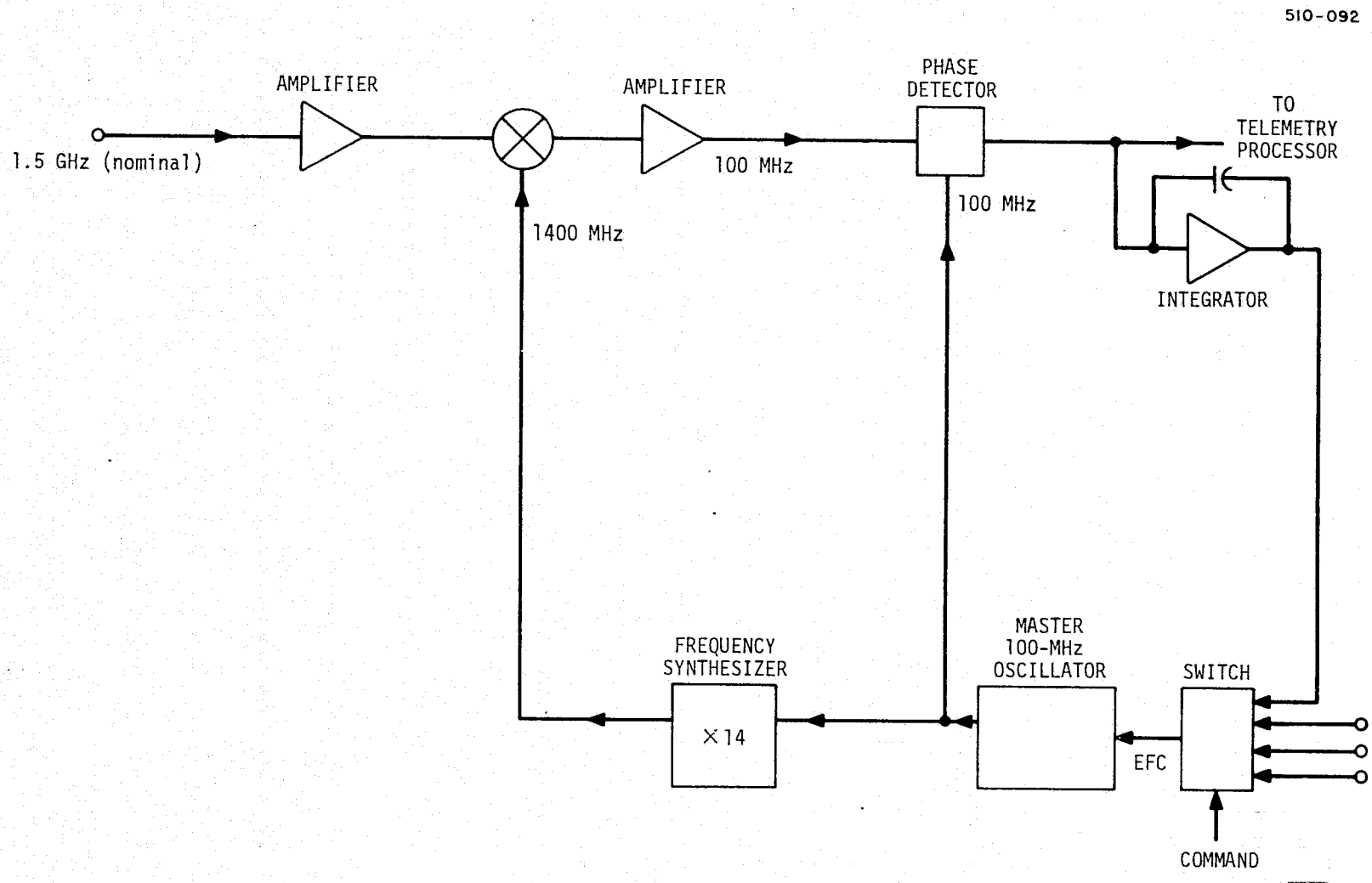

Figure 4. Typical microwave receiver.

2.3.4 Receiving Optics

The antenna system, which includes all components of the spacecraft that transmit or process microwave or optical energy, is a key element in the design of the experiment. The development of a system that will accurately maintain predictable phase relationships between received signals over a frequency range of six decades is the major task in the experiment-preparation phase of the proposed program.

The antenna design will be the result of a series of tradoffs among the following factors, most of which apply particularly to the optical channels:

A. Phase tracking accuracy.

B. Background noise, including

   1) Field of view.
   2) Predetection bandwidth.
   3) Reflected solar radiance.
   4) "Earthshine."

C. Received power level, including

   1) Transmitter power.
   2) Detector sensitivity or noise figure.
   3) Transmitter beam divergence.

D. Spacecraft attitude-control accuracy.

E. Spacecraft pointing accuracy.

It is evident that even a preliminary antenna design will require a detailed study of these tradeoffs.

The simplest and most reliable antenna system should have an extremely wide field of view, so that when it is installed in a gravity-gradient stablized spacecraft, no further pointing provisions are necessary. However, this may complicate both the remaining spacecraft systems and the ground stations to such an extent that a selective on-board pointing system may be desirable. This tradeoff, in particular, requires a careful analysis of the alternatives; even a tentative determination would be hazardous at this time.

2.3.5 Telemetry System

Since no on-board data processing is contemplated, the five phase-difference signals will be transmitted back to the ground station in analog form over standard IRIG FM/FM data channels. The required data bandwidth on each channel is approximately 0 to 5 Hz, with an accuracy requirement of about 2% of full scale.

Phase-lock and signal-strength indications from the quadrature phase comparators, spacecraft attitude and pointing information, and engineering data are also required; however, the total telemetry data rate is very moderate.

The entire telemetry system can be assembled from space-qualified, "off-the-shelf" components; no telemetry-system design or development effort is required in any phase of the proposed program.

2.3.6 Command System

Like the telemetry system, the command system is essentially completely standard. Command functions are necessary only for master-oscillator tuning, antenna pointing, and spacecraft power and attitude control.

2.4 Ground-Station Systems

2.4.1 General

The ground-station experiment systems, outlined briefly here, are shown in block-diagram form in Figure 5 and described more fully in the following sections:

A. Optical transmitting system. The basic elements of the transmitting system are three gas lasers, each modulated by a lumped electro-optic modulator operating at 500 MHz. A 500-MHz power amplifier and a power splitter complete the system.

B. Microwave transmitting system. The microwave transmitting system consists of three conventional transmitters, all phase coherent with the ground-station master oscillator. No modulation capability is required.

C. Transmitting optics. The ground-station transmitting antenna is similar to, but much simpler than, the spacecraft receiving antenna. Because the ground antenna is always pointed toward the spacecraft, the phase relationship between the carriers can be maintained much more readily than in the case of a spacecraft optical system.

D. Telemetry. The telemetry systems are compatible with the on-board telemetry and are standard in most respects.

E. Command. The ground command systems are compatible with the on-board command systems and are of standard design.

F. Data processing. The telemetry data are processed at the ground station to provide a quick-look capability in the field. All telemetry data are recorded in digital form for more detailed computer analysis at SAO.

2.4.2 Optical Transmitting System

The three optical transmitters are essentially identical with each other, except for the laser gas fill and the type of electro-optic material used in the amplitude modulator.

The blue transmitter is an argon ion laser operating at 0.48 μ with a multimode power output of approximately 0.5 w. (HeCd is a potential candidate at a wavelength of 0.44μ. The shorter wavelength increases the dispersion with respect to the red channel, but the available power output is considerably lower.)

The red laser is a HeNe device that operates at the 0.63-μ transition with a power output of about 100 mw. The infrared transmitter is a 10-w CO_2 laser radiating at 10.6 μ.

For maximum efficiency, each channel has its own electro-optic modulator, optimized for the wavelength of its laser output. The modulators, which produce an intensity-modulated output with almost complete extinction at the null, use lithium

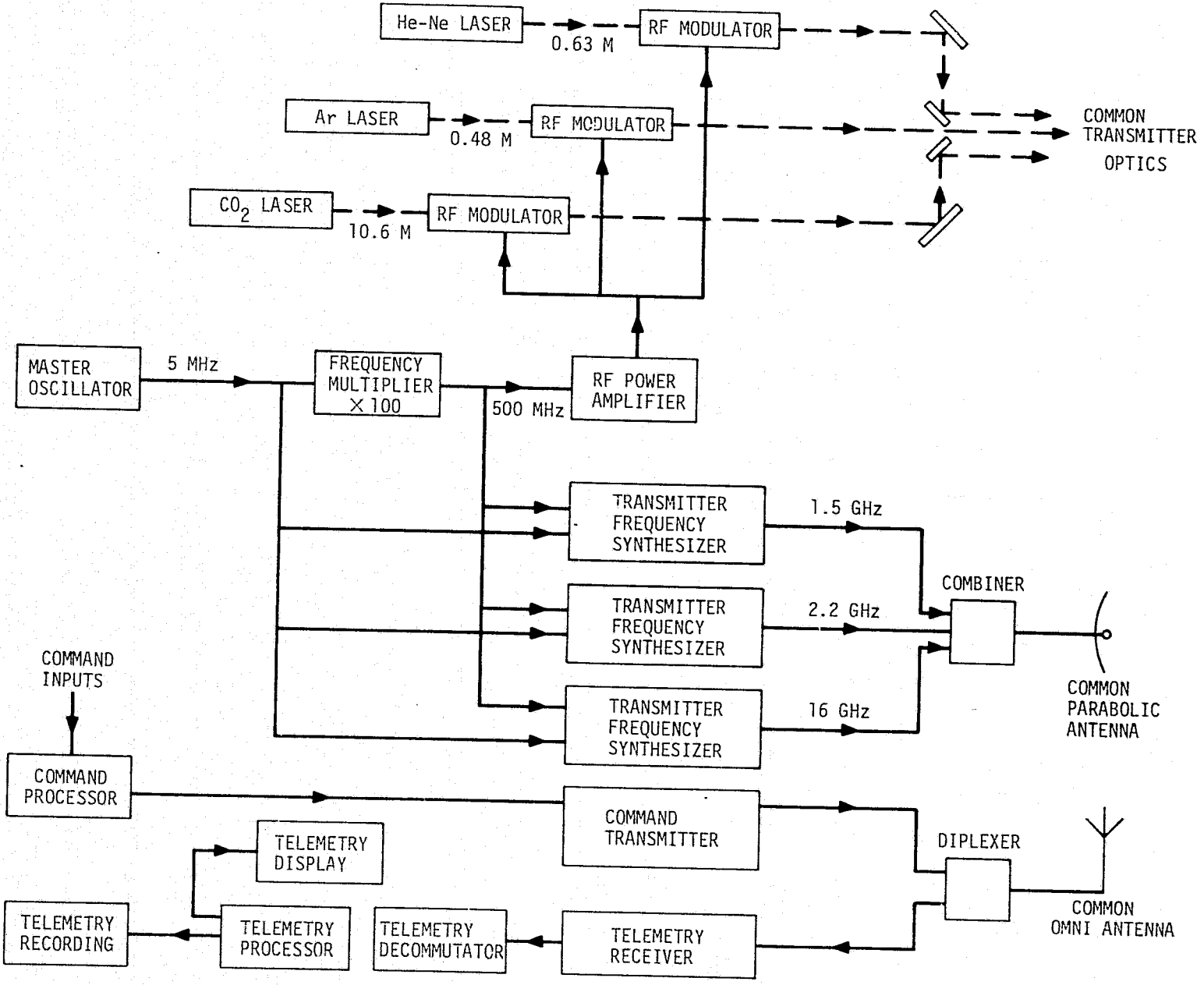

Figure 5. Ground-station block diagram.

tantalite as the electro-optic material in the red and blue channels and gallium arsenide in the infrared. The instantaneous-bandwidth requirement of the modulators is very small, so the modulation power requirement is also quite small (Chen, 1970), on the order of 1 to 2 w at 500 MHz for each channel.

Narrow-band modulators of the type required for the proposed experiment are not "standard" items, but they are relatively straightforward. No research or development effort is required to fabricate them.

It is estimated that a 10-w power amplifier is adequate to drive the modulators simultaneously for all three optical channels. The power amplifier, in turn, is driven by a X100 frequency multiplier from the ground station's 5.0-MHz master oscillator.

2.4.3 Microwave Transmitting System

The 1.5- and 2.2-GHz transmitters are conventional frequency-multiplier chains designed with particular emphasis on low phase noise and differential phase drift. Each transmitter has a 2-w transistor power output stage; the input signal is derived from the 5.0-MHz master oscillator.

The 16-GHz transmitter output stage is a varactor multiplier with a 250-mw power output, also driven by a low-noise solid-state frequency-multiplier chain from the 5.0-MHz master oscillator.

Although each transmitter is shown as an independent subsystem in Figure 5, the differential phase stability of the microwave transmitter system is optimized by using, to the greatest extent possible, frequency multipliers common to all three channels. Detailed design of this system cannot begin until specific frequency allocations have been assigned.

The most stringent requirement imposed on the microwave system is the tight specification on differential phase stability versus temperature necessary for measuring range differences with a precision of $\pm$ 1.0 mm. The most direct approach to minimizing this source of error is to place the entire transmitter system in a thermally controlled environment in order to isolate temperature-sensitive components from ambient variations.

2.4.4 Transmitting Optics

The ground station requires a pedestal capable of tracking the spacecraft with an angular error of less than 150 arcsec. Tracking and acquisition is open loop; the pedestal drives are controlled by the ground-station minicomputer, which is programed with a periodically updated satellite ephemeris.

The three optical transmitters are mounted directly on the pedestal and are bore-sighted with reflective optics to the optical axis of the mount. Simple refractive optics are employed to produce the desired beam divergence at each wavelength.

A 0.5-m parabolic dish is mounted on the pedestal coaxially with the optical axis of the laser transmitters. The three microwave transmitters are installed on the rear of the dish, avoiding the necessity for rotary joints or long flexible cables at microwave frequencies. When the outputs of the transmitters are combined, the surface of the antenna is illuminated through a wide-band cassegrain feed system.

2.4.5 Telemetry System

The telemetry receiver is a commercially available device that operates at approximately 136 MHz. Its output is demodulated by standard, IRIG format, FM detectors and is made available to the ground-station data-processing system.

All experiment data are routed to the ground stations through the spacecraft telemetry system. Telemetry support from the tracking network is not required, as data are acquired only when the spacecraft is in view of the experiment ground stations.

2.4.6 Command System

The command transmitter is also a commercially available unit, producing 5 w in the 135- to 145-MHz band. Commands are keyed in manually to the transmitter, and verification of execution, if required, is established through the telemetry system.

2.4.7 Data Processing

Processing of the experiment data will be off-line. The ground station provides telemetry processing and computer capabilities for quick-look, real-time data analysis and for data formating for digital recording.

The ground station is equipped with a minicomputer for pedestal pointing and tracking, real-time data presentation, digitization of the telemetry data, and control of the tape recorders.

The tape recorders, one primary and one backup, produce a nine-track computer-compatible record under direct control of the ground-station minicomputer. During a satellite pass, the following experiment data channels are recorded:

A. Phase-difference signals, 5 channels.

B. Signal-strength indications, 6 channels.

C. Phase-lock acquisition indication, 1 channel.

D. Spacecraft housekeeping data, 10 channels.

E. Surface meteorological data, 5 channels.

F. Ground-station housekeeping data, 10 channels.

G. Time of day, 1 channel.

The maximum data rate is less than 1 kbps, with a total taped record of less than 10^6 bits per pass. The tape reels will be mailed to SAO for data reduction and processing.

2.5 Multiple-Ground-Station Operation

One of the primary purposes of the proposed experiment is to determine the extent of the spatial correlation between refractive-index error sources for ground stations that are closely spaced — 2 to 100 km apart, for example. Correlated errors will tend to cancel when changes in ground-station separation are being measured, an important variable for geophysical studies.

Correlation can be determined only by measuring range and range-rate errors simultaneously from two or more ground stations. The basic spacecraft design described in Section 2.3 can be extended readily to operate with several ground stations on a frequency-multiplexed basis, as described in the following paragraphs.

2.5.1 Optical Channels

The optical channels are frequency-multiplexed by assigning a specific modulation frequency to each ground station. At the output of each photodetector, a series of filters separates the RF modulation frequencies associated with each station. A phase-lock loop, a nominal 100-MHz master oscillator, and a set of phase comparators are required for each modulation frequency. After the photomultiplier or photodiode output, each phase-difference signal is derived in precisely the manner described in Section 2.3.2.

Telemetry channels are required for the additional phase-difference signals, the number of such channels increasing linearly with the number of ground stations to be processed simultaneously.

2.5.2 Microwave Channels

Frequency multiplexing requires more hardware in the microwave portion of the payload than in the optical case, but it is equally simple in concept. A specific uplink frequency is assigned for each microwave channel at each ground station; the frequency difference for a given channel need not exceed a few megahertz. For example, on the lowest frequency channel, ground station 1 may be allocated a transmitter frequency of 1500 MHz; ground station 2, a frequency of 1502 MHz; and ground station 3, a frequency of 1504 MHz.

Each microwave frequency is down-converted and phase-detected by reference frequencies derived from the uplink optical modulation frequency transmitted from the same ground station. Each phase-detector output signal requires a separate telemetry channel; as in the optical system, the number of telemetry channels increases linearly with the number of ground stations.

2.5.3 Telemetry Data: Ground Stations

With multiplex operation, one ground station is designated as the master and receives, processes, and records all telemetry data. The cost and complexity of the slave stations are reduced by this technique, and the operational procedures are simplified by centralizing all data handling at a single location.

2.6 Experiment Payload Package

The proposed experiment is intended to be a Scout payload, and expected physical dimensions and weight are well within the performance capabilities of the Scout D vehicle for the desired orbit.

The anticipated overall envelope of the payload, excluding booms and solar-cell panels, is a cylinder approximately 85 cm in diameter and 130 cm long. The steerable portion of the gravity-gradient stablized payload, on the earthward end of the cylinder, is approximately 60 cm in length as stowed for launch.

The estimated payload weight, again without stablization wheels, booms, or solar-cell arrays, is approximately 60 kg. The overall weight will not exceed 100 kg. In the current state of development (Jacobs, 1975), the Scout D is capable of injecting 125 kg into a circular 800-km-altitude polar orbit.

The power requirements for the proposed payload can only be estimated at this time. If all systems operate continuously, the power consumption will be approximately 60 w. If certain systems, such as the telemetry transmitter, are turned on only on ground command, the power drain, based on an average over a normal operating day, could be reduced to approximately 30 w.

2.7 Link Margin Calculations

It is outside the scope of this proposal to evaluate the optical and microwave channel signal-to-noise ratios completely. Two links, an optical channel at 0.63 μ and a microwave channel at 1.5 GHz, have been selected as examples to demonstrate the feasibility of the proposed system.

2.7.1 Optical Uplink Margins

The following parameters are assumed for the optical uplink margin:

Wavelength: 0.63 μ

Atmospheric transmission: 0.5

Transmitter power: 0.1 w

Transmitter beamwidth: 300 arcsec (full width to first nulls)

Receiver (spacecraft) aperture: 10-cm diameter

Range: 1000 km

Photomultiplier quantum efficiency: 15%

By using the Friis formulation for received power (Kraus, 1950),

$$P_r = \frac{A_R A_T P_T T_A}{\lambda^2 R^2} \quad , \tag{12}$$

the power at the spacecraft photocathode is

$$P_r = 7.5 \times 10^{-10} \text{ w} \quad ,$$

where A_R is the receiver aperture, A_T is the transmitter aperture, P_T is the transmitted power, T_A is the atmospheric transmissivity, λ is the wavelength, and R is the range.

The signal-to-noise ratio of a received quantum signal in a 1-Hz bandwidth is (Harvey, 1970)

$$\frac{S}{N} = \eta \frac{P_r \lambda}{hc} \quad , \tag{13}$$

where η is the photodetector quantum efficiency, h is Planck's constant, and c is the velocity of light. For the parameters listed above,

$$\frac{S}{N} = \frac{7.5 \times 10^{-10}}{3.1 \times 10^{-19}} \times 0.15 = 3.6 \times 10^{8} \quad .$$

The signal-to-noise ratio in a 1-Hz bandwidth is numerically equal to the number of photoelectrons emitted from the photocathode per second. That in the 5-Hz bandwidth selected for the experiment data is

$$\left(\frac{S}{N}\right)_{5\ Hz} = \frac{3.6 \times 10^{8}}{5.0} = 7.2 \times 10^{7} \quad .$$

Background noise and fading will degrade the effective signal-to-noise ratio to an extent that cannot be precisely estimated at this time. As a conservative estimate, a reduction of the signal-to-noise ratio by a facter of 500 to account for scintillation and background will be applied. Then

$$\left(\frac{S}{N}\right)_{R} = \frac{(S/N)_{5\ Hz}}{500} = 1.4 \times 10^{5} \quad . \qquad (14)$$

The resulting signal-to-noise ratio of 51 db is more than adequate to ensure a precision of 1.0 mm or better in the estimation of the differential range error for a 10-sec averaging interval. In fact, it is apparent that, even with the conservative choice of parameters shown, there remains a very large signal margin for further tradeoffs or contingencies.

2.7.2 Microwave Uplink Margins

The following parameters are assumed:

Frequency: 1.5 GHz

Atmospheric transmission: 0.9

Transmitter power: 2 w

Transmitter beamwidth: 56°

Receiver (spacecraft) aperture: 0.5-m diameter

Range: 1000 km

Noise figure: 5.0 db

Applying equation (12) to the 1.5-GHz link, the recieved power at the spacecraft is

$$P_r = 1.8 \times 10^{-12}\ w \quad .$$

The resulting signal-to-noise ratio in a 5-Hz bandwidth is

$$\frac{S}{N} = \frac{P_r}{FkTB} \quad , \tag{15}$$

where k is Boltzmann's constant, F is the receiver noise figure, T is the background temperature (approximately 300 K), and B is the bandwidth, 5.0 Hz. For the selected parameters,

$$\frac{S}{N} = 2.7 \times 10^7 \quad .$$

This high signal-to-noise ratio, 71 db, is certainly adequate to guarantee the required 1.0-mm precision of the differential range measurement. The higher microwave frequencies, 2.2 and 16 GHz, provide still larger signal-to-noise ratios because of the greater antenna gain at the shorter wavelengths.

2.8 Current State of Knowledge

The atmospheric-refractivity contributions to range and range-rate errors are caused by spatial and temporal variations in the integrated molecular content along the transmission path. Because these variations are, in turn, the result of changes in pressure, temperature, and atmospheric composition, the major emphasis in past studies has been microscale and mesoscale meteorology. Although this indirect approach has not been completely successful, the basic analytical and experimental framework for further work has been established.

2.8.1 Analytic and Theoretical Background

The classic work of Bean and Dutton (1966) carefully summarizes the state of the art of radio meteorology as of that time. Although this basic reference covers a very wide field — including chapters on the measurement of refractivity, refractive-index climatology, ray-tracing, and attenuation of radio waves — of greater interest today is the collection of theoretical and experimental data on the refractive index of air.

As shown in Section 2.3.4, only the ratio of refractivities is required for extracting the dry-component range error from measurements taken at two optical wavelengths. Through the work of Edlén (1953, 1966), Erickson (1962), and Owens (1967), this ratio is known to an accuracy of better than 1×10^{-9}. The absolute values of refractive index in the optical regime are known to an accuracy of about 5×10^{-8} over a somewhat limited range of water-vapor content.

Implied in the entire concept of multiple-wavelength optical measurements is the assurance that the rays at different wavelengths traverse the same geometric path and that the errors introduced by bending of the beams are negligible. That this situation is indeed the case for reasonable elevation angles was demonstrated by Thayer (1967) in a series of ray-tracing computations. For elevation angles greater than 20°, the excess path length introduced by ray bending is typically less than 2.0 mm at both radio and optical wavelengths.

Hopfield (1970) has suggested that the path-length correction for a zenith ray can be very accurately estimated from knowledge of the barometric pressure at the ground station. The barometric pressure is a direct measure of the integrated atmospheric density above the observing station, and thus also a measure of the integrated refractivity over a path extending vertically upward from the station to the limits of the atmosphere. The Hopfield correction does not apply to the water-vapor error component, nor does it apply directly to paths with elevation angles less than 90°. Determining the extent to which the Hopfield correction can be applied to nonvertical transmission paths is a primary mission of the proposed program.

The theory of ionospheric refraction is well developed (Jackson, 1962), and it can be shown that the dominant error source in estimating ionospheric refractivity is the signal-to-noise ratio at the receiving terminals of the microwave channels (Grossi, 1975). Two-frequency transmissions to correct ionospheric range-rate errors have been an integral part of the U.S. Navy's Transit navigation system for many years.

2.8.2 Experimental Data Base

A very large number of experiments relating to refractivity errors in range and range-rate measurements have been described in the literature. Three such programs are of particular interest.

2.8.2.1 MISTRAM

MISTRAM was a radio-interferometer missile-tracking system installed off the east coast of Florida as a component of the Eastern Test Range. The system never met the range or range-rate error specifications established for it, and in 1964, a very large-scale program was begun to determine the cause of the poor performance of MISTRAM. A massive array of instrumentation, including U-2 aircraft to photograph cloud cover, three C-131 refractometer-equipped aircraft, and a large number of ground-based refractometers aand radiosonde stations, was deployed to develop a three-dimensional model of the atmospheric refractivity over the MISTRAM sites. A complex digital ray-tracing routine was developed to process the data returned from the field and to estimate the range and range-rate errors attributable to the tropospheric refractivity. Particular emphasis was placed on refractive-index anomalies in the vicinity of cumulus-cloud formations.

The MISTRAM refractivity program was never finished, nor was a complete analysis of the data ever published. However, the MISTRAM project, limited as it was to one geographical region at one time of year, provides the largest data base available on microscale spatial variations of refractive index.

Although no final report was generated, Weaver and Ringwalt (1964), Cunningham (1964), and Meyer (1964) have described the measurement system, the data-processing techniques, and a limited amount of experimental data in sufficient detail to be useful.

2.8.2.2 Line-integral refractometer

The MITRE corporation sponsored the construction and testing of an instrument to measure dispersion associated with the water-vapor absorption line at 22 GHz.

The technique employed was identical to that proposed in Section 2.3 except that two microwave frequencies (15.6 and 31.2 GHz) were used and the transmission path was between two terminals on the surface.

As in the case of the MISTRAM program, the line-integral refractometer project does not appear to have been carried through to completion, judging from the available literature. However, a large number of data were generated (Richardson, 1964), some of which are of value to the planning of the proposed experiment.

2.8.2.3 Two-wavelength optical distance measurements

The two-wavelength instruments developed by WPL provide the most significant data available on the effects of the refractive index of the air on optical range measurements (Owens and Earnshaw, 1968; Bouricuis and Earnshaw, 1974). The results of the tests made with these instruments, although limited to relatively short surface paths, are directly applicable to the proposed experiments and are discussed further in Section 3.1.1.

3. ENGINEERING DEVELOPMENT

3.1 Previous Research and Development Activities

3.1.1 Multiple-Wavelength Range Measurements

To the best of our knowledge, no direct measurements of tropospheric refractive range errors for satellite-to-ground transmission paths have been made. However, the particular technique proposed for the program — simultaneous multifrequency range measurements — has been studied in great detail (Thayer, 1967), and a very successful instrument, the WPL Two-Wavelength Distance-Measuring Instrument, has been built and carefully tested (Bouricuis and Earnshaw, 1974).

It should be noted that the problem attacked by the WPL instrument is much more difficult than the one proposed here; their instrument is designed to measure the absolute distance to a remote retroreflector over a 10-km surface path.

3.1.1.1 Two-Wavelength Distance-Measuring Instrument

The WPL instrument employs two gas laser transmitters: one of HeCd radiating at 0.44 μ and one of HeNe at 0.63 μ. The two transmitted beams are merged and polarization-modulated by an electro-optic modulator common to both transmitted wavelengths at a radio frequency of approximately 2.7 GHz.

Both beams are transmitted to a remote retroreflector and returned to the transmitter telescope. The red and blue beams pass through the polarization modulator again on the return trip and are then separated by dichroic mirrors and detected by separate photomultiplier tubes.

To determine the absolute distance to the retroreflector — that is, the number of wavelengths of either red or blue light in the path between the transmitter and the retroreflector — the modulation frequency is swept over a wide range, and the frequencies at which an integer number of wavelengths can be fitted into the path length are noted. From these data, a first-order estimate, accurate to one wavelength at the modulation frequency, can be determined.

After the number of wavelengths has been determined, the red and blue channels are operated alternatively with 10-sec averaging intervals for each measurement, to determine the range to within a small fraction of a wavelength. The modulation frequency is automatically adjusted so that the change in the plane of polarization of the out-going beam is precisely canceled by the reverse-polarization change on the return pass. Knowing the wavelength number and the frequency at which cancellation occurs, we can calculate the time of flight of the wave packet from the transmitter to the retroreflector and return with an accuracy of approximately ± 10 psec. The difference between the measurements made at 0.44 μ and those at 0.63 μ can be used, in conjunction with the known dispersion of atmospheric air, to calculate the geometric range by means of the technique outlined in Section 2.2.2.

3.1.1.2 Performance of the two-wavelength instrument

The WPL Two-Wavelength Distance-Measuring Instrument and an earlier generation of instruments operating on the same principles have all been extensively field tested.

The most important and convincing measurement series (Bouricuis and Earnshaw, 1974) was a side-by-side comparison, over a 7-km horizontal path, of the two-wavelength instrument with a conventional, single-wavelength geodimeter. The results can best be summarized by comparing the variance of the measured range under identical operating conditions. The range variance for the WPL instrument was 0.05 cm, while that for the geodimeter was 0.8 cm, even after correcting for path temperature as estimated from measurements taken at each end of the transmission path.

3.1.2 System Components

A detailed analysis of the state of the art of each of the components and subsystems proposed for this program is not possible at this time. Preliminary, and very tentative, studies indicate that all the proposed hardware is practical and capable of being qualified for space flight.

The spacecraft receiving antenna is the most challenging design task because of the stringent requirements on differential-path-length stability over a wide range of frequencies and satellite orientations with respect to the ground stations.

The problem of cooling an infrared photodetector to 100 K or less is made more difficult by the orbit of the proposed satellite, which will periodically point the radiator of a passive cooler directly at the sun. The infrared channel, however, is a secondary mission and we do not propose to expend an undue proportion of the total available resources to the solution of this engineering problem.

3.2 Expected Experiment Results

3.2.1 Experiment Definition Phase

The end result of this, the first, phase of the program will be a series of reports and documentations providing a complete experiment design, a critical study of all potential hardware-development problems, and a preliminary design of the experiment's critical components, that is, the spacecraft antennas and the infrared photodetector cooling system.

3.2.2 Experiment Preparation Phase

The experiment preparation phase will produce deliverable hardware as well as studies and analysis. A breadboard model of the spacecraft experiment system, excluding basically standard items, will be constructed. A breadboard of the ground-station hardware will also be fabricated in order to test and evaluate the payload.

The test results, an analysis of the test data, and a set of detailed engineering model specifications will constitute the major documentation results of this phase.

3.2.3 Engineering Model Development and Test Phase

The ouput of this phase will be, primarily, an engineering model of the proposed payload. The ground-station breadboard will be upgraded to provide realistic test conditions for the engineering model payload.

Documentation for this phase will include a complete set of as-built drawings and a final report detailing the test results and the analysis of the data. The analysis will incorporate conclusions as to the capability of the proposed payload to measure refractive range errors to the desired accuracy under space-flight conditions and recommendations for further studies and experiments.

4. STATEMENT OF WORK

We propose to design and construct an engineering model of a payload, together with the required ground-station equipment, to study and analyze the effects of atmospheric and ionospheric refraction on range and range-rate errors encountered in satellite-to-ground systems employed for geophysical, geodetic, and navigation applications. The ultimate purpose is to construct an atmospheric model to permit computation of ranging and velocity errors for particular systems under known conditions.

A three-phase program is proposed. It would encompass an experiment definition phase, an experiment preparation phase, and an engineering development phase, concluding with the construction of an engineering model of the proposed payload and a breadboard model of a ground station.

We propose a 30-month program; the experiment definition phase would be 8 months; the experiment preparation phase, 10 months; and the engineering development phase, 12 months.

4.1 Tasks for the Experiment Definition Phase

A. Analysis of signal-to-noise margins, including tradeoffs among pointing accuracy, antenna beamwidth, transmitter power, and predetection filter bandwidth.

B. Analysis of phase stability of critical components, including estimates of performance variations under flight conditions.

C. Design of critical components, in particular the optical and microwave antennas, with emphasis on predictable behavior of the antenna phase centers as the look angle varies. The cooled infrared detector feasibility study will be begun in this phase.

D. Initial development of the optical/microwave antenna system. This will be the longest lead item, and development should begin as early as possible in the program.

E. Preparation of the experiment plan, including an analysis of the spacecraft orbital parameters, the number of ground stations required, the selection of geographic areas best suited for ground-station locations, and an estimate of the extent of the measurement program. Also included will be an estimate of the number of measurements required at each ground-station location and the expected accuracy of the range-difference measurements as a function of the number of measurements.

F. Analysis of the spacecraft support-system requirements, including: power, thermal control, attitude stabilization, pointing (if required), tracking, telemetry, command, and structure.

4.2 Tasks for the Experiment Preparation Phase

A. Development and building of a breadboard model of the proposed payload, including the optical/microwave antenna system but excluding the RF telemetry and command systems.

B. Development and building of a breadboard model of the proposed ground station, exclusive of the telemetry and command systems.

C. Testing of the breadboard payload and ground station as a complete system, with particular emphasis on the performance of the optical/microwave antenna and the ability to resolve path-length differences as small as 1.0 mm.

D. Preparation of engineering model specifications in sufficient detail to permit construction of all or some components of the payload by outside contractors.

4.3 Tasks for the Engineering Development and Test Phase

A. Construction of an engineering model of a payload with the capability of operating with two ground stations simultaneously. The command and telemetry systems will be included in the engineering model.

B. Refitting of the breadboard ground station with multiple-frequency capability to permit simulation of two independent, simultaneously operating ground stations.

C. Testing of the engineering model payload with the refitted breadboard ground station; evaluation of experimental data and determination of the suitability of the design concept for flight application.

4.4 Deliverable End Items

A. Engineering model payload, including as-built drawings.

B. Breadboard ground station.

C. Contract-end-item specification.

D. Data-reduction computer programs.

4.5 Reporting

At the end of each phase, SAO will prepare a report that will document in detail the activities during that phase, present the conclusions reached, and recommend actions to be taken in succeeding phases. The report at the end of the third phase will be regarded as a final report, and as such will summarize the work of the first two phases, give details on the third phase, and present conclusions and recommendations based on the entire program.

5. MANAGEMENT AND COSTS

This proposal is being submitted in response to NASA's Announcement of Opportunity No. OA-75-3, dated 7 August 1975, for the Advanced Applications Flight Experiments Program.

It will be the responsibility of the Principal Investigator, Dr. Martin W. Levine of SAO, to define, coordinate, and direct the overall experimental program. He will direct the scientific analyses necessary to define the parameters of the experiment and establish data-processing and analysis techniques to evaluate the data.

The program will be conducted within the Geoastronomy Division, headed by Dr. G.C. Weiffenbach. The Division includes a large and competent staff of scientists, mathematicians, and computer programers whose expertise will be applied as required. This group is currently conducting research under a number of grants and contracts, including several from NASA, demanding expertise in earth dynamics, celestial mechanics, high-precision satellite tracking, doppler ranging, and sophisticated computer-aided analysis.

Administrative support will be provided by the Geoastronomy Program Office, supervised by Raymond N. Watts, Jr. This office will be responsible for coordinating contract administration, scheduling, budgets, reports, and management support necessary to ensure timely, cost-effective achievement of the scientific goals described in the preceding sections.

The Smithsonian Institution is an independent establishment that is under a Board of Regents. The Institution proper, as distinguished from executive agencies of the Government, was created when James Smithson, an Englishman who dedicated his fortune to the increase and diffusion of knowledge among men, designated the United States of America as his trustee to accomplish that objective. The trust was accepted by Congress.

The Smithsonian performs research, educational, and other special projects supported by grants and contracts awarded under those cost principles of the Federal Procurement Regulations and the Armed Services Procurement Regulation that pertain to educational institutions (Subpart 1-15.3 and Section 15, Part 3, respectively).

It is audited by the Defense Contract Audit Agency, Silver Spring, Maryland. This project is being proposed by the Smithsonian as an educational institution.

The Charter of the Smithsonian Institution carries a mandate for the "increase and diffusion of knowledge among men." Therefore, any grant or contract that may be awarded as a result of this proposal must be unclassifed, in order not to abridge the Institutions's right to publish, without restriction, findings that result from this research project.

Considering the nature of the proposed effort, it is requested that a cost-reimbursement research-and-development contract with letter-of-credit funding with

educational institutions be awarded to cover the proposed project in accordance with Part IV of GSA Federal Management Circular No. FMC 73-7 dated 19 December 1973. Pursuant to Part III of GSA Federal Management Circular No. FMC 73-7, it is requested that title to all equipment purchased or fabricated under the proposed contract be vested irrevocably in the Institution upon acquisition except for the deliverable end items listed in Section 4.4.

In accordance with an agreement between the Headquarters of Naval Material Command, Washington, D.C., and the Smithsonian, the Institution operates on a predetermined overhead rate with carry-forward provisions, and the indirect costs are computed as a percentage of total direct costs. The overhead rate proposed herein is 31%, which has been approved as a predetermined rate through 30 June 1975 and as a provisional billing rate thereafter.

The proposed starting date is 1 July 1976.

ESTIMATE OF COST

Proposal P 579-11-75

Object Class	Phase I	Phase II	Phase III	Total
Personnel Compensation	$61,500	$148,467	$92,891	$302,858
Personnel Benefits	11,555	27,339	17,582	56,476
Travel	1,244	2,640	9,120	13,004
Real Property Rental	2,888	6,305	2,557	11,750
Equipment Rental	176	220	300	696
Communications	600	800	840	2,240
Postage	80	100	120	300
Printing and Reproduction	225	294	360	879
Other Services	4,400	31,165	600	36,165
Computer Time	3,000	10,000	—	13,000
Supplies and Materials	700	225,250	75,300	301,250
Total Direct Cost	$86,368	$452,580	$199,670	$738,618
Indirect Cost @ 31%	26,774	140,300	61,898	228,972
Subcontracts (over $10K)	—	—	1,500,000	1,500,000
Total Cost	$113,142	$592,880	$1,761,568	$2,467,590

6. REFERENCES

Bean, B. R., and E. J. Dutton, 1966, Radio Meteorology. Nat. Bureau Standards Mono. 92, Washington, D.C.

Bouricuis, G. M., and K. B. Earnshaw, 1974, Results of field testing a two-wavelength optical distance-measuring instrument. Journ. Geophys. Res., vol. 79, pp. 3015-3018.

Chen, F. S., 1970, Modulators for optical communications. Proc. IEEE, vol. 58, pp. 1440-1456.

Cunningham, R. M., 1964, Scale and type of atmospheric refractive index anomalies. Presented at the Third Tropospheric Refraction Effects Meeting, 1974; in proceedings, ESD-TDR-64-148, pp. 33-42, 1966.

Earnshaw, K. B., and E. N. Hernandez, 1972, Two-laser optical distance measuring instrument that corrects the atmospheric index of refraction. Appl. Opt., vol. 11, pp. 749-754.

Edlén, B., 1953, The dispersion of standard air. Journ. Opt. Soc. Amer., vol. 43, pp. 339-344.

Edlén, B., 1966, The refractive index of air. Metrologia, vol. 2, pp. 71-80.

Erickson, K. E., 1962, Investigation of the invariance of atmospheric dispersion with a long-path refractometer. Journ. Opt. Soc. Amer., vol. 52, pp. 95-122.

Grossi, M. D., 1975, Private communication.

Harvey, A. F., 1970, Coherent Light. J. Wiley & Sons, Inc., New York; see especially p. 1036.

Hopfield, H. S., 1970, Tropospheric effect on electromagnetically measured range: Prediction from surface weather data. Johns Hopkins University TG-1119.

Jackson, J. D., 1962, Classical Electrodynamics. John Wiley & Sons, Inc., New York; see especially pp. 226-230.

Jacobs, K., 1975, Private communication.

Kraus, J. D., 1950, Antennas. McGraw-Hill Book Co., New York; see especially p. 54.

Melchior, H., M. Fisher, and F. Arams, 1970, Photodetectors for optical communications systems. Proc. IEEE, vol. 58, pp. 1466-1486.

Meyer, J. H.,1964, Digital atmospheric profile generation. Presented at the Third Tropospheric Refraction Effects Meeting, 1974; in proceedings, ESD-TDR-64-148, pp. 43-56, 1966.

National Aeronautics and Space Administration, 1973, Advanced Scanners and Imaging Systems for Earth Observations. NASA SP-335, 604 pp.

Owens, J. C., 1967, Optical refractive index of air: Dependence on pressure, temperature and composition. Appl. Opt., vol. 6, pp. 51-59.

Owens, J. C., and K. B. Earnshaw, 1968, Development of a microwave-modulator, dual optical wavelength geodetic distance-measuring instrument. ESSA Tech. Rep. ERL 117 WPL 8, 107 pp.

Richardson, H. M., 1964, Field test results of the line integral refractometer. Presented at the Third Tropospheric Refraction Effects Meeting, 1974; in proceedings, ESD-TDR-64-148, pp. 95-114, 1966.

Smith, E. K., Jr., and S. Weintraub, 1953, The constants in the equation for atmospheric refractive index at radio frequencies. Proc. IRE, vol. 41, p. 1035.

Thayer, G. D., 1967, Atmospheric effects on multiple-frequency range measurements. ESSA Tech. Rep. IER56-ITSA53.

Weaver, T. S., and D. L. Ringwalt, 1964, Simultaneous refractive index measurements by three aircraft. Presented at the Third Tropospheric Refraction Effects Meeting, 1974; in proceedings, ESD-TDR-64-148, pp. 9-32, 1966.

VITA

MARTIN W. LEVINE

Physicist

Education:

Massachusetts Institute of Technology, B.S.E.E. (1954)
Massachusetts Institute of Technology, M.S.E.E. (1954)
Purdue University, Ph.D. (1965)

Positions Held:

1960-65	Instructor in Electrical Engineering, Purdue University
1965-66	Member of Technical Staff, Mitre Corporation
1966-69	Engineer, Hewlett-Packard, Beverly, Massachusetts
1969-	Physicist, Smithsonian Astrophysical Observatory
1969-	Research Associate, Harvard College Observatory

General Fields of Investigation:

Quantum electronics, specifically development of atomic time and frequency standards; hydrogen maser development and investigation of noise processes in time and frequency standards and their applications to radio astronomy